Annealing Effect on Tri-component Nanoscale Metallic Multilayer Films

Rachel L. Schoeppner

Ph.D Candidate, Washington State University

Dr. Megan J. Cordill

Supporting Faculty, Department of Materials Physics, Montanuniversitaet Leoben, and

Erich Schmid Institute of Materials Science, Austrian Academy of Sciences

TABLE OF CONTENTS

Abstract

There is an increase in the hardness of tri-layer nanolaminate metallic films (Cu/Ni/Nb) after annealing at 300°C, indicating the likelihood of a change in the microstructure. In this current study Cu/Ni/Nb tri-layer and CuNi/Nb alloy multilayer films were subjected to a range of annealing conditions in vacuum to determine the extent of microstructural and strength change resulting from both different temperatures and annealing times. X-ray diffraction measurements were conducted on pristine and annealed films to determine if the increased hardness was a result of alloying, oxide formation, or intermetallic formation. While the peak ratios did show a change from the as-deposited condition, no obvious intermetallic peaks developed in the majority of the annealed samples. TEM results showed the development of a very thin Ni_xNb_y layer forming on either side of the Nb layer in both tri-layer and alloy films. Post annealing nanoindentation results verified that all annealing conditions resulted in increased hardness for all annealing temperatures and times. However, there is a peak annealing temperature and time that is different for the two different multilayer systems. The hardness of the alloy film continues to increase as the annealing time at 300°C increases, while the 30 nm tri-layer film peaks at an annealing time of 3 hours before dropping again. All films show a peak hardness from the 500°C annealing condition, matching with a thicker Ni_xNb_y layer at the incoherent boundary. This multilayer system has shown an interesting increase in strength with annealing that is not typically seen in other nanoscale metallic multilayer currently being investigated and will likely be a candidate for aging treatments similar to bulk Al alloys. The increase in strength is a direct result of intermetallic formation as a result of the Ni and Nb interaction. This phenomenon can be implemented in a variety of different multilayer systems to achieve even higher hardness values, which could be desirable in other hard coating applications.

CHAPTER 1 : Introduction

1.1 Motivation

Increasing the useful lifespan of technical components is a recurrent objective and technical challenge for any engineering application. Many components fail as a result of mechanical degradation over time; this is often directly linked to operating conditions, whether that is through fatigue, wear, thermal cycling, high impact bombardment, radiation, or a gamut of other possibilities. In order to increase the lifetime of some components hard coatings can be applied as a mechanical barrier, which protects the main component underneath. These hard coatings are utilized in countless applications ranging from tribological to electrical, optical, or even radiological barriers.

Two of the most common sources of failure, one of which is the particular focus of this investigation, are operational degradation from thermal annealing and wear. In either case the microstructure of the material is compromised and leads to softening, which in turn leads to macroscopic failure. In order to combat this type of degradation, hard coatings can be tailored to resist such microstructural changes. Nanocomposite materials have been known to show remarkable strength due to the small intrinsic length scales. The intrinsic size relationship for nanocomposites has been under investigation for decades, attempting to understand the underlying mechanisms responsible for deformation. These mechanisms continuously change as the length scale decreases from micro-scale to the nano-scale and are dependent on dislocation interactions with the increasing number of interfaces, whether they be grain-boundaries or interfaces. At extremely small length scales, the strength once again begins to decrease as dislocations overcome boundary barrier strengths.

One such system that has been studied extensively over the past few decades are nano-scale metallic multilayers (NMM) due to their atypically high strength and surprising durability in harsh environments. The strength and deformation response of these materials are directly related to the nature of their interfaces. Coherent interfaces are generally weaker but often exhibit greater ductility than incoherent interface systems. A mixed interface system has shown superior properties of both interface types leading to higher strength, greater ductility, and significant strain-hardening ability and is the focus of this investigation. Thus far, the reliability of these systems in conditions closer to actual operating environments has not yet been investigated and is the focus of the current investigation. Since annealing inherently changes the interface of the multilayers, whether it is through triple point formation, alloying, or spheroidization, over time the yield behavior and deformation of the multilayers will be negatively affected. Annealing has the potential to negatively affect all forms of strengthening techniques, not just multilayers, especially when the number of interfaces increases.

1.2 Common Strengthening Mechanisms and Their Limitations

Many different techniques are typically used to increase the strength of a material, depending on the application and desired results. Some of these techniques include the control of grain size [1]–[4], deposition of nano-laminate structures [5]–[7], and the addition of solid solution impurities [3], [8]–[11], precipitates or oxide particles [9], [12], [13], all of which have the potential to degrade when used under elevated temperature service conditions.

One way in which grain-boundary mobility can be suppressed is by adding impurities into the microstructure to act as stabilizers [11], [14], [15]. In one particular study, samples with lower impurity concentrations exhibit significant grain growth in the deformed region of the sample while the grain size in the un-deformed regions remains the same as the as deposited condition [16], a classic example of stress-induced grain growth. In contrast, grain growth in the deformed region of a high impurity concentration sample is suppressed, suggesting that impurities are effective in decreasing grain growth by pinning grain boundaries, thus reducing grain boundary sliding, rotation, and diffusion. This stabilization technique can be applied to both solid-solution strengthened as well as oxide dispersion strengthened (ODS) materials. However, impurities in solid-solution strengthened materials can segregate to the grain-boundaries over time, and this behavior can be accelerated as a result of annealing. While this doesn't necessarily mean the material would no longer exhibit grain size stabilization, it does reduce the solid-solution strengthening benefit.

Precipitation strengthening uses small precipitates to act as barriers to dislocation motion as well as Frank-Read dislocation sources. This technique is often used in strengthening of aluminum to create lightweight, high strength metals for use in aviation and other technical engineering applications. This type of strengthening is more stable than solid solution impurity strengthened materials because diffusion of the precipitate is more difficult than the diffusion of individual impurity atoms, leading to less diffusion to the grain boundaries. However, precipitation strengthened materials can also undergo Oswald ripening where atoms from smaller precipitates diffuse to larger precipitates causing them to grow at the expense of the smaller ones increasing the interparticle spacing and thus reducing the material's strength.

1.3 Strengthening Mechanisms in Nanoscale Metallic Multilayer Systems

Nano-scale metallic multilayers also have an intriguing ability to increase strength, similar to the way in which grain size reduction increases the strength of a material, with strengths far exceeding those of corresponding bulk metals [17]. The strength is highly dependent on the individual layer thickness, interface type, and material selection leading to a wide variety of properties, which could be tailored to suit specific applications. At larger layer thicknesses, down to a few hundred to several tens of nanometers, the strengthening relationship follows the Hall-Petch relationship ($\sigma \alpha 1/d^2$) [4], which is also seen in non-layered microstructures. As the layer thickness drops below a certain point, the strength increase more rapidly than the Hall-Petch model predicts, indicating a change in the deformation mechanism from traditional dislocation pile-up to a different mechanism depending on the interface structure.

The type of deformation mechanism occurring in the multilayers is highly dependent on the interface morphology and can be separated into two general categories: coherent and incoherent interfaces. Coherent interfaces occur in multilayer systems consisting of materials with similar crystallographic structures (i.e. Cu-Ni) but a lattice spacing mismatch. This mismatch causes a tensile strain in the layer with larger lattice spacing and a compressive strain in the other layer, which results in a coherency stress [18]. The stresses begin dropping off as the distance from the interface increases. Therefore, as the distance between two interfaces decreases, the less the stress is allowed to relax and the stronger the film becomes. Misfit dislocations are also likely to appear along the interface to relieve some of the stress; these dislocations can act as barriers to other dislocations and further increase the strength. Additionally, since the crystallographic structures are the same in both layers, and many coherent systems grow epitaxially, slip systems are continuous. This leads to dislocation transmission across the interface and results in reasonable ductility as well as an increase in strength.

On the other hand, incoherent interfaces are constructed of layers with different crystallographic structures (i.e. Cu-Nb), with no continuous slip plane and thus are much stronger barriers to slip transmission [19], much like grain boundaries with transmission only occurring when the strength overcomes the barrier strength. While this type of interface is often stronger than the coherent system, it is also more brittle due to shearing of the interface. The deformation mechanism for this type of interface at small layer thicknesses is the confined-layer-slip (CLS) mechanism, which has been observed in many different systems [19]–[21]. As there is no longer sufficient room for dislocations to build up against the interfaces, dislocations instead glide through a single layer, bowing along the interface and leaving dislocation debris, in the form of misfit dislocations. This debris in turn interacts with passing dislocations leading to an increased flow stress and strain-hardening. Once the layer thickness decreases below a few nanometers, dislocations can no longer bow due the extremely small radius of curvature of the propagating dislocation. At this point, the strength in the film is high enough to overcome the interface strength and dislocations can cut straight through. In some cases, there is actually a softening in these extremely thin layers which has been shown to be a result of increased dislocation nucleation and propagation [22]. A summary of this strength to layer thickness trend is schematically shown in Figure 1-1.

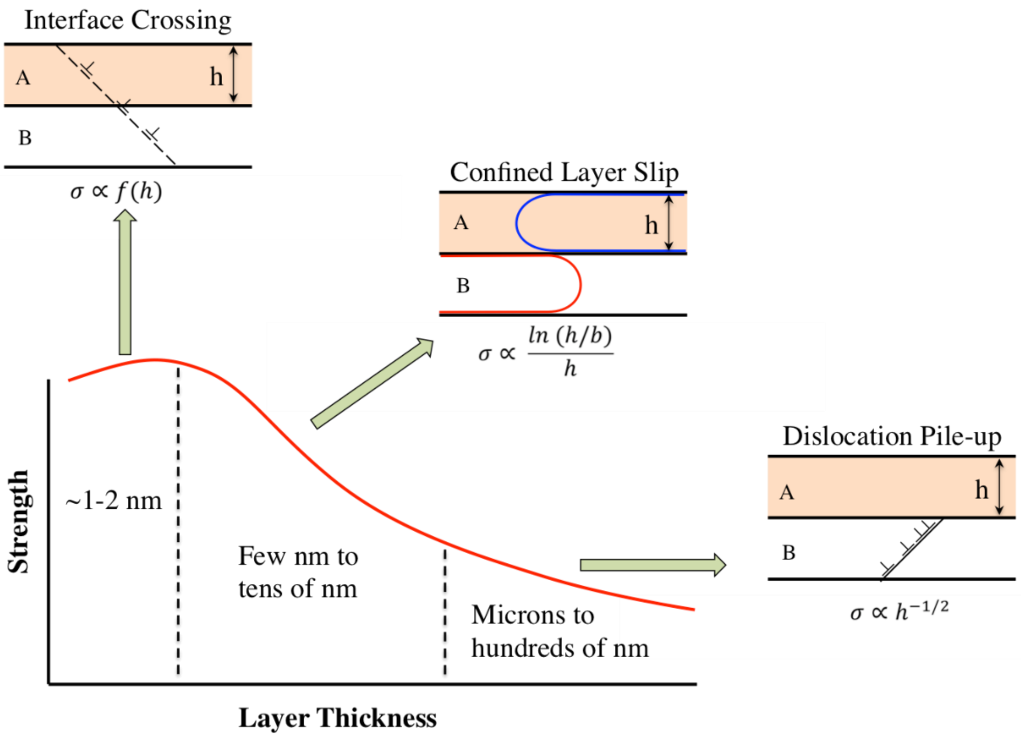

Figure 1-1. Schematic of controlling deformation mechanisms occurring in multilayers with incoherent or weak interfaces at different layer thicknesses.

Tri-layer systems have a combination of both coherent and incoherent interfaces and have been suggested to possess properties of both types of interfaces through dislocation dynamic simulations [14, 21-23]. These films suggest that the strong incoherent interface in combination with the coherent interface can lead to additional strain-hardening [24]. The Cu-Ni-Nb tri-layer system has been investigated using two different nanoindentation techniques to investigate the extent of strain-hardening occurring in these layers. The first technique tests the hardness of the material using tips with two different included angles, which create different effective strains under the indenter tip [27]. Results from bulge testing (~0.2% strain) and nanoindentation with a Berkovich (~8% strain) and cube-corner (~22% strain) tip were used to approximate the stress-strain curve of Cu-Ni, Cu-Nb, and Cu-Ni-Nb multilayers, Figure 1-2. The tri-layer system started with the lowest strength at 0.2% effective strain, but managed to surpass both other bi-layer films, suggesting a higher strain-hardening behavior.

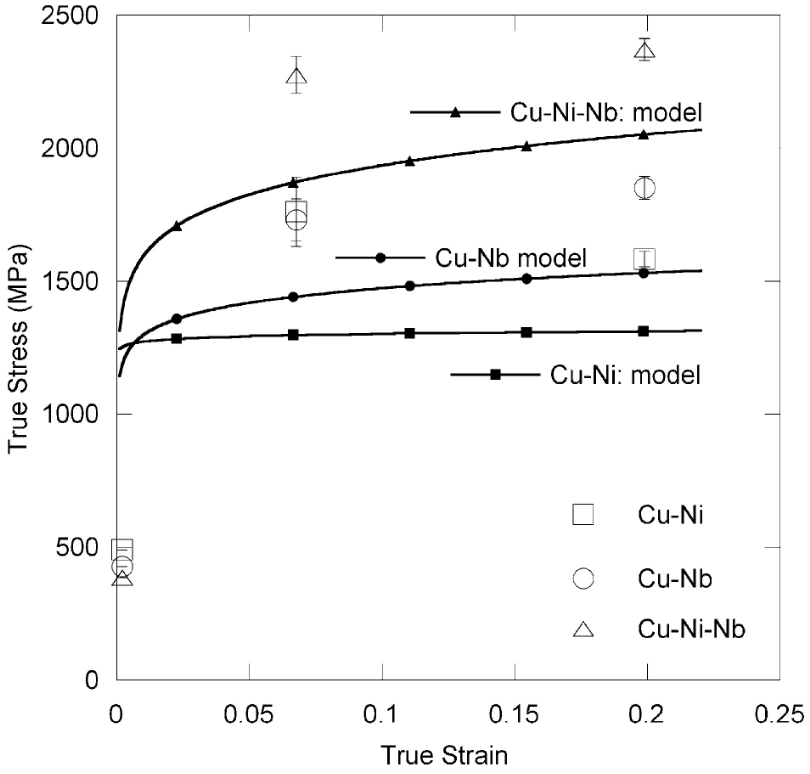

Figure 1-2. Stress-strain curves approximated from nanoindentation and bulge testing techniques on Cu-Ni, Cu-Ni and Cu-Ni-Nb multilayers with individual layer thicknesses of 20 nm. Lines are curve fit approximations from the data points [24].

Additionally, scanning probe microscopy images of the indents show tri-layers having less pile up than both bi-layer systems, indicating increased strain-hardening ability. Both of these results substantiate each other, experimentally indicating that tri-layer films would show a higher strain-hardening exponent than bi-layer systems. However, molecular dynamic simulations indicate a different trend where the strength for the tri-layer system actually starts higher than both bi-layer systems at small strains and lies in between Cu-Ni and Cu-Nb at larger strains [25], suggesting a lower strain-hardening ability than the Cu-Nb system. Since these results are inconsistent with the experimental results discussed previously, more direct measurements of the strain-hardening ability of these films is required. The differences in these predictions of strain-hardening behavior could be a result of small variations in interface structure or loading conditions, which suggests a more robust understanding is needed.

Tri-layer films generally follow the same deformation mechanism as incoherent interfaces, where confined-layer-slip is dominated at small layer thickness. The dislocation is contained in the Cu/Ni bi-layer and bows along the Ni-Nb and Cu-Nb incoherent interface. The presence of the coherent interface in the center of this threading dislocation causes a "super threader" dislocation [28]. As these super threaders propagate, dislocation debris is deposited at the incoherent interface, causing this weak interface to shear. The sheared interface then produces internal shear stresses in the system and combined with elastic mismatch between the two materials, causes cross-slip to occur. This cross slip acts as an additional barrier to dislocations, making propagation increasingly difficult and adding to greater strain-hardening behavior over the bi-layer systems [28]. This ability to cross-slip is not seen in the bi-layer systems, since the effect only occurs at high stresses with a continuous FCC-FCC system. Without the added strength from the Nb layer, Cu-Ni bi-layers cannot reach high enough stresses to cross-slip, and therefore is unique to the tri-layer system.

1.4 Thermal Stability of Multilayer Systems

The thermal stability of these NMM systems is crucial if they are to be used as hard coatings in service conditions above room temperature. If the layered structure begins to degrade, the strengthening benefit would be seriously compromised. Many studies have been conducted on the annealing stability of NMMs, mostly focusing on incoherent interfaces [26-37]. An elevated temperature nanoindentation study on thin film Cu [41] showed a 60% reduction in hardness as the temperature increases by 100˚C, coupled with a pronounced drop in modulus, whereas Cu-Nb multilayer studies conducted at elevated temperatures showed only a 40% drop in yield strength after a 200˚C temperature increase [38]. This suggests the addition of a layered structure has the potential to decrease the temperature sensitivity, allowing the thin film to maintain a greater percentage of its strength at elevated temperatures. Since the thermal stability of thin films, especially multilayers, is controlled by the tendency to decrease the internal energy of the system, and multilayered structures have both high elastic strains and a high density of interfaces, it is more preferable to rearrange the interface structure to help reduce the total energy in the system. This can occur either through interfacial mixing, alloying, or layer breakdown due to triple joint formation from the reduction of interfacial energy [42]. The extent of which any of these mechanisms occur is dependent on the temperature, chemistry, and layer thickness.

Several detailed studies have been conducted on the thermal stability of Cu-Nb bi-layers [19], [34], [38], [40], examining both mechanical and structural changes in the layers using nanoindentation and micro-tensile testing. Due to their mutually low miscibility the Cu-Nb system shows remarkable resistance to thermal degradation, maintaining a layered structure to temperatures over 600°C, but is dependent on layer thickness, with thinner layers breaking down at lower temperatures. Vacuum annealed freestanding Cu-Nb bi-layer films with individual layer thicknesses ranging from 15 to 75 nm [19] showed films with layer thicknesses larger than 35 nm maintained a layered structure up to 700°C for several hours, with the only deviation from the original structure being triple-joint formation, similar to that seen in Figure 1-3. Conversely, 15 nm layer thickness sample showed layer pinch-off and spheroidization after only half an hour at the same temperature. There was also a significant drop in hardness in the 15 nm films after annealing, whereas 75 nm layers showed a minimal drop in hardness, attributed directly to the change, or lack thereof, in the microstructure of the film.

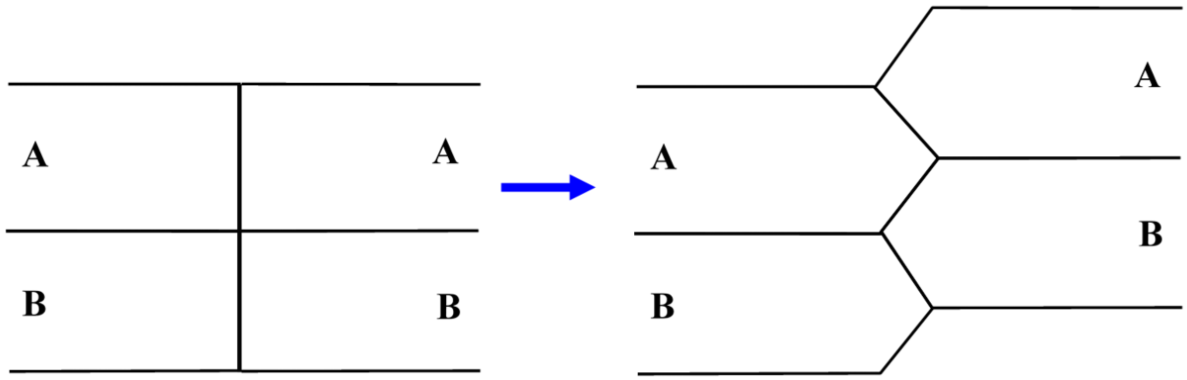

Figure 1-3. Schematic showing how triple joints form in annealed bi-layer films with grain boundaries present in both layers.

Similarly, Economy et. al. annealed Cu-Nb films with 20 nm and 100 nm layer thicknesses in a variety of atmospheres at 400˚C for 30 minutes [34]. The 20 nm Cu-Nb samples showed a significant loss of hardness even though other studies have shown thermal resistance above 400°C, whereas the 100 nm sample maintained its structure and hardness. The different atmospheres had a negligible effect on the change in hardness, indicating oxidation is not a major contributing factor. Since a breakdown of the layered structure generally isn't seen until higher temperatures, the authors attribute the decrease in hardness to a change in the internal stress of the films, which is supported by x-ray diffraction (XRD) analysis, rather than a breakdown of the layers. Elevated temperature micro-tensile tests of freestanding Cu-Nb films in Ar showed a significant drop in tensile strength and elastic modulus as the testing temperature increased, with a corresponding increase in ductility [38]. The structure of the layers was examined post mortem in both the unstrained shoulder region and near the fracture surface. The unstrained, but annealed, shoulder showed the original layered structure with triple-joint formation (as was seen in previous studies), whereas the deformed region near the fracture surface showed grain elongation in Cu layers, suggesting power-law or diffusion-based creep, along with grain rotation of the Nb layers, suggesting grain boundary sliding. Strain rate tests were also conducted and suggest high temperature deformation occurs as a result of dislocation glide and climb, as was indicated by the calculated hardening exponent.

Elevated temperature testing on coherent interfaces is less common than for incoherent systems like Cu-Nb since they are generally more miscible, like the Cu-Ni system, and readily alloy at elevated temperatures [18], [43]. This could completely eliminate the benefit of the layered structure, instead creating a solid solution Cu-Ni alloy. That being said, some elevated temperature studies have been conducted, both experimental and theoretical. Due to the diffusivity asymmetry between Cu and Ni, during the initial stages of annealing a transient interface sharpening along with a shift in position and increase of the composition gradient is likely [43]. Eventually the interfaces begin to broaden and there is complete mixing of the two regions, resulting in a loss of the layered structure and likely a drop in strength. Similarly, Bunshah et. al. conducted elevated temperature tensile testing of Cu-Ni multilayers, deposited at different temperatures and with layer thicknesses over 100 nm [44]. Significant alloying was seen for samples that were deposited at a substrate temperature of 625˚C and for samples annealed above 600˚C, though no mechanical testing was conducted on these samples to determine the effect on hardness and yield strength to determine the relative strength drop as a result of alloying. This system also showed a greater retention of strength in the higher layer thickness samples, likely due to the smaller likelihood of complete alloying which would be seen in the thinnest layer samples.

1.5 Diffusion and Alloying of Components Used in Cu/Ni/Nb Multilayers

1.5.1 Cu-Ni System

When studying the annealing characteristics of materials with multiple components, one of the first things to consider is how the different materials interact at higher temperatures. Binary phase diagrams are widely used and have been well characterized for decades, and are the first step to understanding how an alloy will form when undergoing heat treatments and annealing. The phase diagrams for the components used in this multilayer annealing investigation are shown in Figure 1-4 (Cu-Ni), Figure 1-5 (Cu-Nb), and Figure 1-6 (Nb-Ni). The first thing to notice from Figure 1-4 is the complete miscibility of Cu and Ni, across all concentrations. This suggests that with an increase in the annealing temperature, the chemically distinct Cu/Ni bilayers will start to form the CuNi alloy. Since these two materials are completely miscible, the diffusion coefficients [45] are also high with:

$$D^*_{Cu \to Ni} = 5.7x10^{-1} \exp\left(\frac{-61.7 \text{ kcal mol}^{-1}}{RT}\right) \text{ cm}^2\text{/s}$$

$$D^*_{Ni \to Cu} = 2.7x10^{-1} \exp\left(\frac{-56.5 \text{ kcal mol}^{-1}}{RT}\right) \text{ cm}^2\text{/s}$$

where *R* is the universal gas constant (1.987 cal K^{-1} mol^{-1}) and *T* is the absolute temperature. From these equations, the volume diffusion rates can be calculated at different temperatures. At 573K (300°C) Ni will diffuse in to Cu at a rate of $\mathbf{7.62x10^{-23}}$ cm^2/s and Cu will diffuse into Ni at a rate of $\mathbf{1.67x10^{-24}}$ cm^2/s (with a small degree of uncertainty). These diffusion rates tell us that at 300°C, Ni will diffuse faster into Cu than Cu will into Ni. However, both will occur at an extremely slow rate.

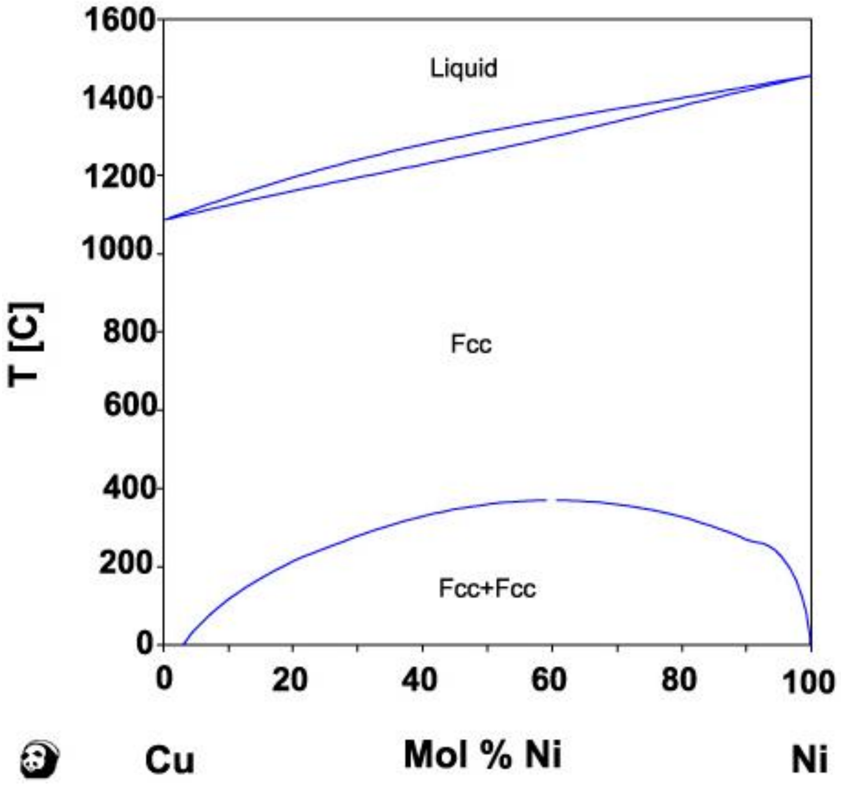

Figure 1-4. Cu-Ni phase diagram showing complete solubility at all concentrations. The two a_1 and a_2 phases shown to exist in lower temperatures and higher concentrations of Ni, are both FCC phases and are dependent on the Ni ratio in the CuNi alloy [46].

As Cu and Ni begin to diffuse into each other and a CuNi alloy begins to form, the diffusion rate will actually change as Ni (or Cu) now is diffusing into an alloy as opposed to the pure material. Therefore, over time, diffusion rates will change depending on the CuNi alloy concentration. The diffusion coefficients of Ni into different concentrations of CuNi alloy [45]:

$$D^{*}_{Ni\rightarrow Cu(78.5at\%)} = 6.3\text{x}10^{-2}\ \exp\left(\frac{-49.7\ \text{kcal mol}^{-1}}{RT}\right)\ \text{cm}^{2}/\text{s}$$

$$D^{*}_{Ni\rightarrow Cu(45.4at\%)} = 17\ \exp\left(\frac{-66.8\ \text{kcal mol}^{-1}}{RT}\right)\ \text{cm}^{2}/\text{s}$$

$$D^{*}_{Ni\rightarrow Cu(13at\%)} = 35\ \exp\left(\frac{-74.9\ \text{kcal mol}^{-1}}{RT}\right)\ \text{cm}^{2}/\text{s}$$

indicate that as the concentration of Cu increases in the alloy, the diffusion rate will increase as the diffusion driving force decreases. At 573K (300°C) the diffusion rates of Ni into alloys with 78.5at%, 45.4at%, and 13at% Cu are **$6.96\text{x}10^{-21}$** cm^2/s, **$5.63\text{x}10^{-25}$** cm^2/s, and **$9.47\text{x}10^{-28}$** cm^2/s respectively (taking into account some degree of uncertainty). Therefore, as Ni begins to diffuse into Cu, the diffusion rate will gradually decrease as the concentration of Ni increases, slowing down the diffusion process. Given enough time, the Cu and Ni layers will reach an equilibrium and create a fully alloyed layer. Once this has occurred, the tri-layer system will essentially become a bilayer system similar to the alloy system also investigated in the current study.

1.5.2 Cu-Nb System

The second combination that is important in these multilayers is the Cu-Nb system. In direct contrast to the Cu-Ni layers, the Cu-Nb layers are essentially insoluble across the entire composition range (Figure 1-5). These two materials are notoriously difficult to alloy, only managing to alloy using extreme mechanical methods (e.g. high pressure torsion). From the phase diagram (and previous annealing studies on Cu/Nb multilayers [30], [47]), it can be assumed that these layers will not alloy when subjected to the annealing conditions used in this study. Since these materials are completely immiscible, there will be little to no diffusion of the atoms into the other layer.

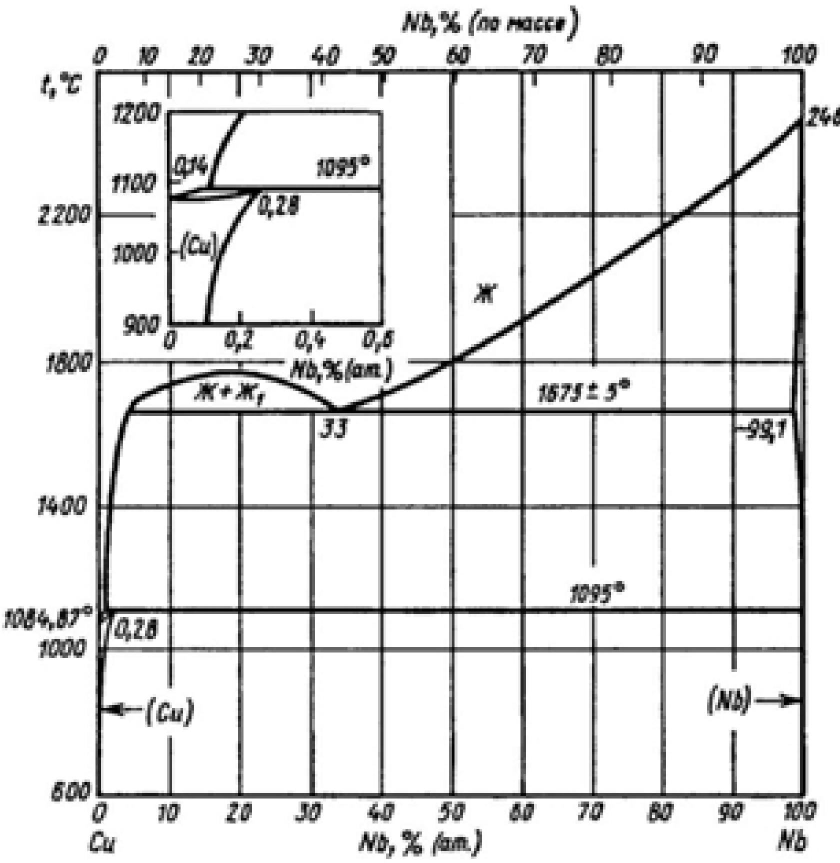

Figure 1-5. Cu-Nb phase diagram shows virtually complete insolubility up to a temperature of about 1000°C [48].

1.5.3 Nb-Ni System

One of the more complicated systems in these multilayers is the interaction of the Nb-Ni layers. It is apparent from Figure 1-6 that many different intermetallics are possible across the composition range, all of which form easily at lower temperatures. This suggests that any annealing, even at modest temperatures, would create Nb_xNi_y intermetallics. Depending on the different diffusion rates of Ni into Nb, and Nb into Ni, the composition of the intermetallic could be either Ni_6Nb_7, Ni_3Nb, Ni_6Nb, or could even non-stoichiometric. X-ray diffraction will be able to determine which intermetallic is favorable. However, depending on the distance from the interface, there will most likely be a gradient Ni concentration which would result in Ni_xNb_y of different compositions.

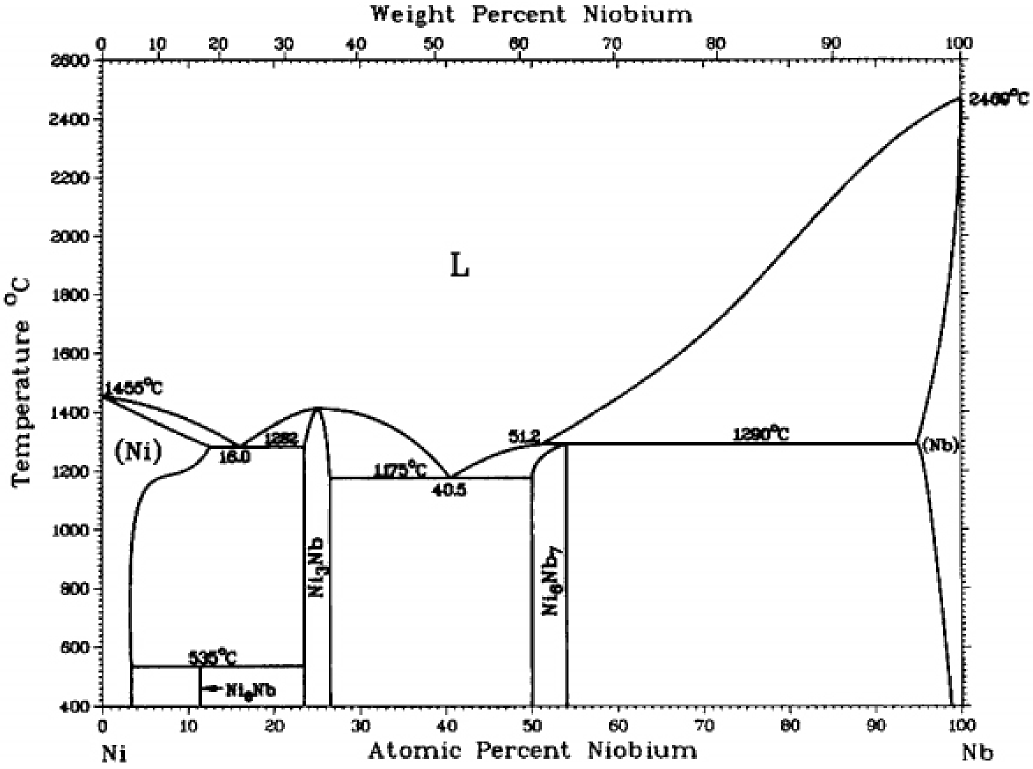

Figure 1-6. Nb-Ni phase diagram showing multiple possibilities for intermetallic formation across different concentrations [49].

1.6 Testing Techniques

1.6.1 Wafer Curvature

Wafer curvature is a thin film testing technique which tracks the changing curvature of a film as it undergoes heating and cooling cycles. The difference in thermal expansion between the film material and the substrate material causes the sample to curve into increasingly smaller radius of curvature as the temperature rises. By tracking and calculating the changing curvature values, the stress in a thin film on a thick substrate can be approximated by using the well-known Stoney equation:

$$\sigma_f = \frac{E_s {t_s}^2}{6(1-\nu)t_f R} \tag{1-1}$$

where E_s is the substrate biaxial modulus, t_s is the substrate thickness, ν is the film Poisson's ratio, t_f the film thickness, and R is the measured curvature [50]. Typically, films are deposited onto single crystal silicon wafers which have been well characterized over the years; therefore, as long as the thicknesses of the film and substrate are known (ν is typically estimated to be 0.3 for metals) the stresses in the film can be tracked through different heating and cooling cycles. A theoretical stress temperature relationship can be determined from the basic principles of thermal expansion and plastic flow, shown in Figure 1-7, which are governed by thermally activated glide [50]. The boundary lines (dashed lines) shown in the figure can be determined by the stress required for plastic flow:

$$\sigma = \tau\left(1 - \frac{T}{T_F}\right) \tag{1-2}$$

where τ is the limiting stress at absolute zero and T_F is the temperature at which the flow stress would go to zero. The sample will exhibit elastic behavior up to the point when it is heated or cooled to the stress state which approaches one of the boundaries, then substantial plastic flow occurs and the profile follows the limiting lines.

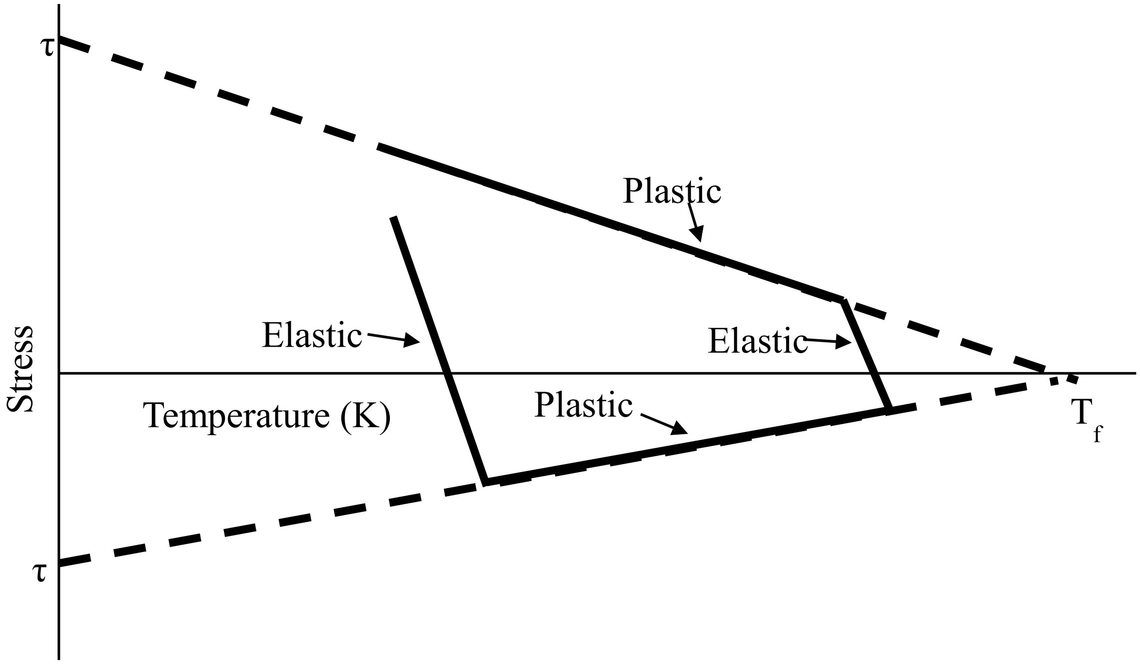

Figure 1-7. Idealized stress-temperature profile based strictly off thermal expansion and plastic flow where $\sigma=\tau(1-T/T_f)$ [50]**.**

A simple stress-temperature profile for a thin metal film on a Si substrate is illustrated in Figure 1-8, where the initial portion of the heating curve is linear, indicating the stresses in the film are still in the elastic regime and have not exceeded the yield stress. Once the film approaches the plastic flow limiting line, the profile becomes non-linear and the film has reached the yield stress of the metal at that particular temperature. While this stress vs. temperature relationship shown in figure 1-8 is quite idealized, many other factors could contribute to deviations from this behavior including phase changes, grain growth, strain hardening behavior, etc.

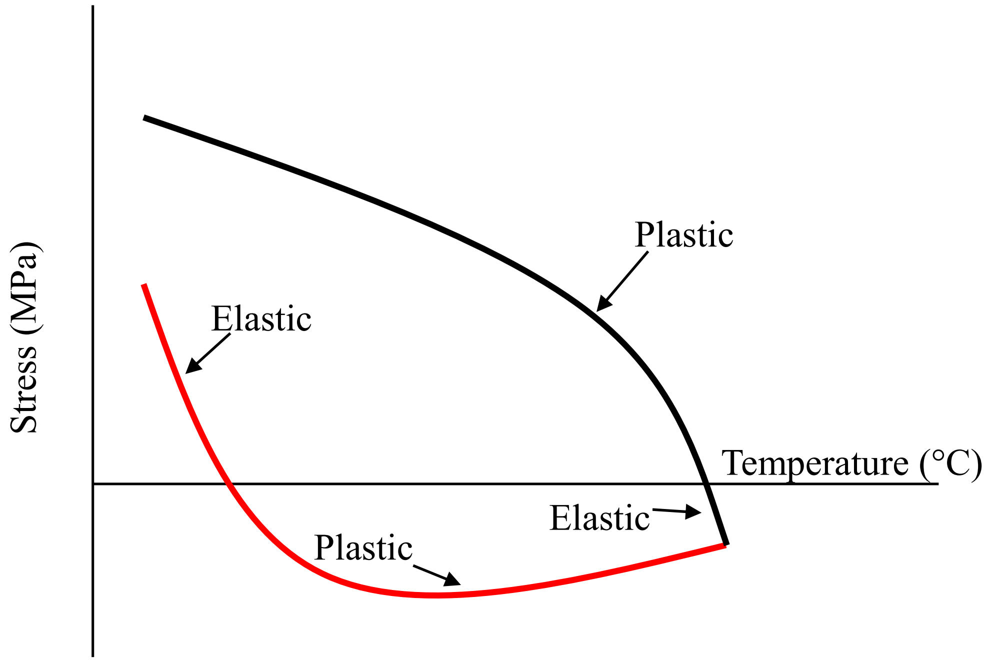

Figure 1-8. Typical stress vs. temperature profile indicating regions of elastic deformation and plastic deformation.

1.6.2 X-ray Diffraction

X-ray diffraction is a quick, non-destructive technique often used to identify elements in a given sample and determine any residual stresses that might exist in the film. In this technique, the x-rays that penetrate the sample get reflected off at specific angles, unique to the crystal orientation and lattice spacing following the relationship known as Bragg’s Law:

$$2d\sin\theta = n\lambda \tag{1-3}$$

where d is the lattice parameter, θ is the incidence angle, n is an integer, and λ is the wavelength of the x-ray beam. Each material has a unique pattern that can be used to determine the chemistry of an alloy or powder. When a material is highly textured, or single crystalline, there will only be one peak which corresponds to the crystallographic plane which is normal to the surface. For example, a Cu (111) crystal will have a single peak at $2\theta = 43.3°$.

For fine powders or polycrystalline samples, specifically ones with very small grain sizes, the crystallite size can be determined from the full-width half-max (FWHM) of the peak of interest where smaller crystallites result in significant broadening of the diffracted peak. Although the crystallite size is not necessarily the grain size, it is often a close approximation. While this is a very useful characteristic of XRD, it leads to some complications in multilayer measurements which was seen in the current study and will be discussed in further detail in Chapter 4. Additionally, the broadening of the peak makes it more difficult to pinpoint the diffraction angle and thus makes it more difficult to determine residual stresses and exact chemistry. The residual stress in the film can actually be inferred from the lattice spacing if the chemistry is already known. Elastic strains in the lattice will cause either a smaller (for compressive stress) or larger (tensile stress) lattice spacing when compared to films without intrinsic strains. First order residual stresses can then be calculated from these elastic strains using the known elastic modulus and the well-known Hooke's Law ($\sigma = E\cdot\varepsilon$).

Since the nanolaminate systems investigated here are created using sputter deposition, most often each layer is highly textured, making them ideal for XRD characterization. Both intrinsic stresses which develop from deposition as well as any alloy resulting from deposition or annealing can be determined from the scans. XRD scans from each of the samples are compared to reference peaks of pure materials to identify composition and determine the relative shift due to internal stresses. After annealing, the films were once again examined using XRD, comparing peak to valley ratios to determine the relative amount of alloying from annealing.

1.6.3 Transmission Electron Microscopy and Energy-dispersive X-ray Spectroscopy

Materials with nano-scale intrinsic lengths cannot be investigated with traditional microscopy techniques such as optical or scanning electron microscopy. However, transmission electron microscopy (TEM) has the capability of achieving atomic resolution and is typically used to image NMM films with layer thicknesses on the order of a few to tens of nanometers. The *bright field* imaging technique utilizes transmitted electrons to create an image of the material from the scattered electrons. As the density and thickness increases, more electrons are deflected inside the material and results in a darker image.

Diffraction imaging is another useful technique which allows for higher contrast images based on atomic density and lattice defects in the material. This technique uses diffracted electrons as opposed to transmission electrons, to produce diffraction patterns which are specific to the material and crystallographic orientation. Any defect in lattice which would result in a change in the diffracting planes (including dislocation, stacking faults, lattice strain, etc.) will alter the Bragg diffraction and thus become visible in the resulting image. The dark field technique is ideal for examining materials with very similar atomic densities (such as Cu and Ni) and for grain size and orientation and is therefore the preferred technique for examining the films investigated in the current study.

Energy dispersive x-ray spectroscopy (EDS) is a technique used for elemental analysis and chemical characterization of a material. This technique can be used in both scanning electron microscopy (SEM) as well as TEM to determine the elements present in a sample. As a material is hit with high energy electrons, some of those electrons will cause secondary effects in the atoms of the material. One of these is the excitation (and subsequent relaxation) of electrons in the atom which will emit characteristic X-rays depending on which energy state the electrons fall to. For example, an electron which relaxes from the L shell to the K shell of a molybdenum atom will emit the K_α X-ray with 17400 eV. Other combinations of electron relaxations will emit different energies, all of which are unique to the particular atom. For lighter elements ($Z<50$), the K and L X-rays are typically used for characterization since the energies these transitions emit are easy to excite with mild incident energy as well as being easily distinguishable. A representative EDS spectrum (Figure 1-9) [51] shows how this technique can be used to determine different elements and their relative amounts based on the intensity of the peak. The two different Cu peaks belong to two different excitation levels, the furthest left belonging to L_α and the right peak from K_α.

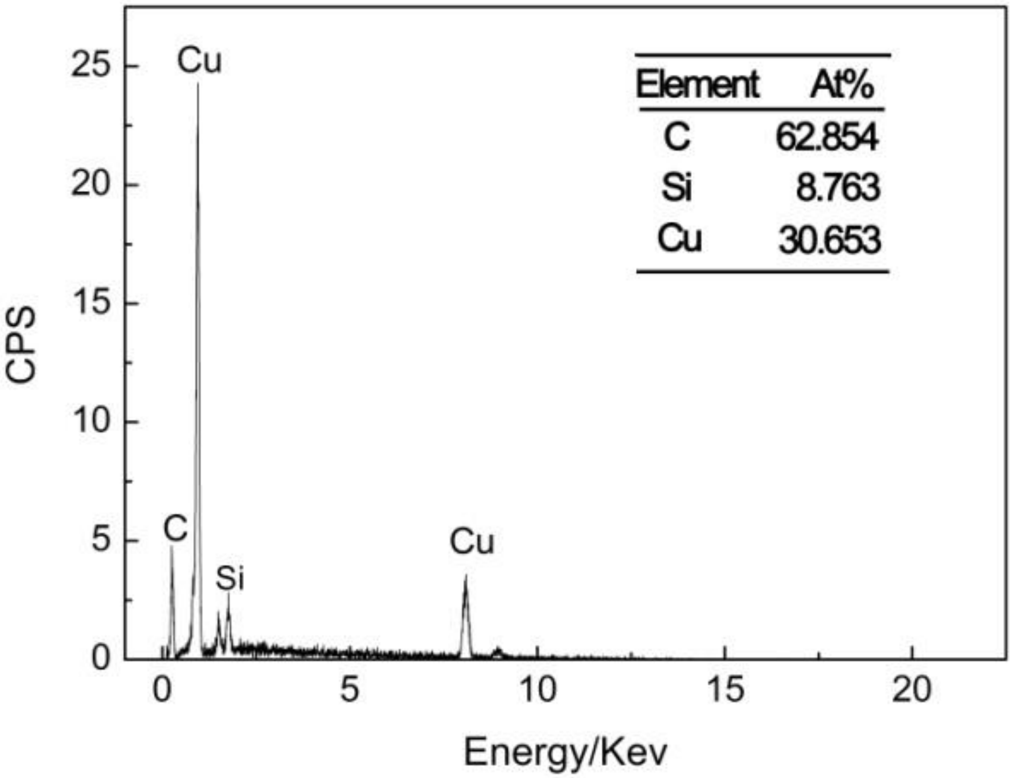

Figure 1-9. Example of an EDS spectrum taken from SiC-Cu composite interaction zone [51].

The sampling volume of this technique is quite often about the same size as the interaction zone of the microscopy technique since the incident electron beams are responsible for emitting the X-rays. For SEM, this volume is more than 1 μm^3 while for TEM the volume is much smaller due to the sample thickness, which doesn't cause the X-ray spread seen in bulk samples. Using the STEM mode in the TEM beam widths and thus spatial resolution can be on the order of about 10 nm, allowing for area and line scans to determine composition across interfaces or determine compositions of different fine particle phases.

1.6.4 Nanoindentation

Instrumented nanoindentation has become an increasingly popular way to test mechanical properties of thin films due to the ease and breadth of testing ability. Instrumented indentation differs from typical hardness tests in both the fact that the load and depth are measured during the test as well as the fact that the indents are extremely small, thus optical observation of the contact area is difficult so contact area must be calibrated to indentation depth by indenting a standard material, typically fused quartz or polycarbonate, at various depths. Based on contact mechanics equations [52], material hardness and modulus values can be determined from the load-depth curve. The initial portion of the unloading segment is purely elastic, with the slope S representing the stiffness of the material, where $S=dP/dh$, and therefore can be used to calculate the elastic modulus of the material. The stiffness however is indicative of both the elastic response of the material and the machine response, therefore a combination of the material of interest and the tip material yields a reduced modulus, E_r, where:

$$E_r = \frac{1}{\beta}\frac{\sqrt{\pi}}{2}\frac{S}{\sqrt{A_p(h_c)}} \quad . \tag{1-4}$$

This reduced modulus is a combination of the sample modulus, E_s, as well as the indenter tip modulus, E_i, and is related through the contact mechanics equation:

$$\frac{1}{E_r} = \frac{1-\upsilon_i^2}{E_i} + \frac{1-\upsilon_s^2}{E_s} \tag{1-5}$$

where v_i is the Poison's ratio of the indenter material and v_s is the Poison's ration of the sample. Typical nanoindentation probes use a diamond tip, with E_i=1140 GPa and v_i=0.07. The hardness of the material can be calculated by the relationship: $H=P_{max}/A$, where P_{max} is the maximum load and A is the contact area.

The projected contact area of the indent is calculated using a standard material (with known modulus) to calibrate a tip area function based on specific depths. Although this allows the mechanical values to be quickly calculated from the indentation depth, it is also problematic if the area function does not accurately depict the actual contact area to depth calibration. A large number of materials exhibit either a sink in or pile up effect during nanoindentation [53] which can change the actual contact area and thus the calculated reduced modulus and hardness of the tested material. A material which exhibits perfectly plastic deformation would deform freely as opposed to elastically deforming underneath the tip, this results in significant pile-up around the indenter, as is depicted by the blue dashed line in Figure 1-10. This results in a much higher contact area than is assumed from the tip area function calibrations, which in turn will depict a larger calculated reduced modulus and, to a greater extent, the hardness values. Similarly, sink-in will have a smaller actual contact area and calculate artificially small values for both the modulus and hardness.

Not only can material modulus and hardness values be determined, but depending on the tip geometry the strain-hardening behavior can also be inferred. Based on the included angle of a conical indenter tip, different local strains are created in the material immediately beneath the contact [54]. Using this approximation, a Berkovich (θ=65.35°) and cube-corner (θ=45°) indenter geometry correspond to an effective strain of approximately 8% and 22%, respectively [55]. Using these effective strains the strain-hardening response of a material can be investigated, where a material that exhibits strain-hardening will have a higher hardness when tested with a cube-corner tip.

Another technique for investigating the strain-hardening response of a material regards the relative pile-up around the indenter. For if a material exhibits significant strain-hardening, it will harden with increasing deformation and thus reduces the amount of pile-up occurring around the indenter. Bower developed a relationship between the amount of pile up and the strain-hardening response of the material [56]:

$$\frac{h}{a} = \frac{(\kappa - 1)}{\kappa tan\theta} \tag{1-6}$$

where h is the height of the pile-up region, a is the contact radius, θ is the included angle of the indenter and κ is related to the strain-hardening ability of the material. Figure 1-10 shows a schematic for a material that exhibits pile-up (blue line), sink-in (black dashed line), and neutral deformation (red dashed line). As is annotated in the figure, the pile-up height drastically changes the contact area at the same depth whereas sink-in reduces the contact area. Using a combination of these two techniques, the strain-hardening response of the sample can be inferred, though the specific strain-hardening exponent cannot be absolutely determined due to the complicated stress state that exists under the indenter tip. To determine a value for the strain-hardening response of the material, a uniaxial condition is required, leading to either micro-pillar or micro-tensile testing techniques.

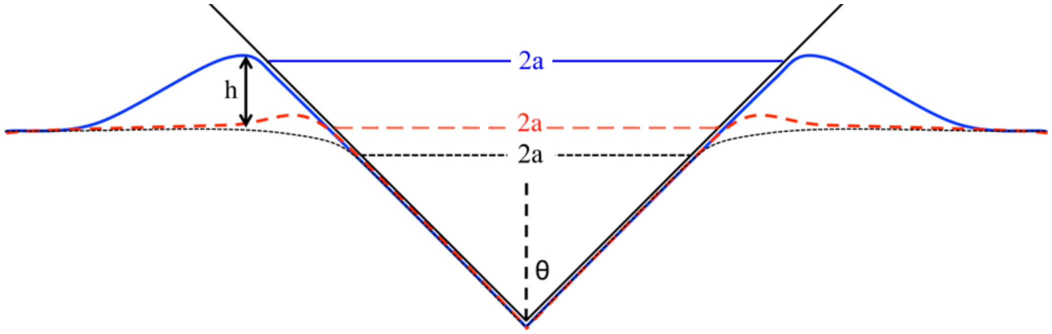

Figure 1-10. Schematic of pile-up and sink-in effects on the contact radius during indentation. Pile-up (blue line) occurs in materials which readily plastically deform whereas sink-in occurs when the material can elastically account for the material being displaced by the indenter.

Traditionally high temperature testing of materials has been limited to tensile testing of macro-scale samples or static indentation, with elevated temperature instrumented indentation (ETI) only increasing in popularity over the past few years. One of the main complications with ETI is thermal drift [51-53] which occurs as a result of the temperature difference in the sample as well as between the sample and the indenter tip. To overcome the internal temperature difference the sample is typically allowed to come into thermal equilibrium typically for a minimum of one hour, though the thermal gradient from the bottom of the sample contacting the heating stage to the surface still exists. Another option is to heat the tip as well as the sample, which has been shown to reduce the drift to less than 1 nm/s in some cases [58]. Even with the issues surrounding ETI, this technique is quick, easy to use and provides reliable comparisons between samples and different testing conditions even if the strain state is non-linear.

1.7 Previous Annealing Studies on Tri-component NMM films

Previous ETI and elevated temperature micropillar compression investigations on these tri-layer and alloy multilayer systems showed an increase in hardness and σ_{max} at room temperature after annealing, which is not typically observed in multilayer systems. Figure 1-11 summarizes the room temperature strength values for the as deposited and annealed conditions in all four films with error bars showing the spread between the two tests performed. The majority of multilayer systems show a breakdown of the layered structure resulting in an overall softening of the film after annealing, whereas in the current study only the 5 nm Cu-Ni/Nb alloy incoherent interface film showed a decrease in the room temperature strength as a result of the current annealing conditions. This increase in strength as a result from annealing was also seen during elevated temperature nanoindentation [60] and was suggested as being a result of precipitation of NbNi particles along the interface, adding to the strength of the multilayer system as a whole. There are a few different possible reasons why the 5 nm sample does not show this same trend. Either the Ni in the alloy prefers to stay in the alloy rather than diffuse into the Ni and create precipitates, in which case there would not be that additional strengthening mechanism, or annealing has caused a breakdown in the layered structure likely resulting in spherodization, which has been seen to occur in other bi-layer systems. Since the 30 nm film still shows increased strength after annealing, it is more likely that layer breakdown is occurring in the 5 nm sample.

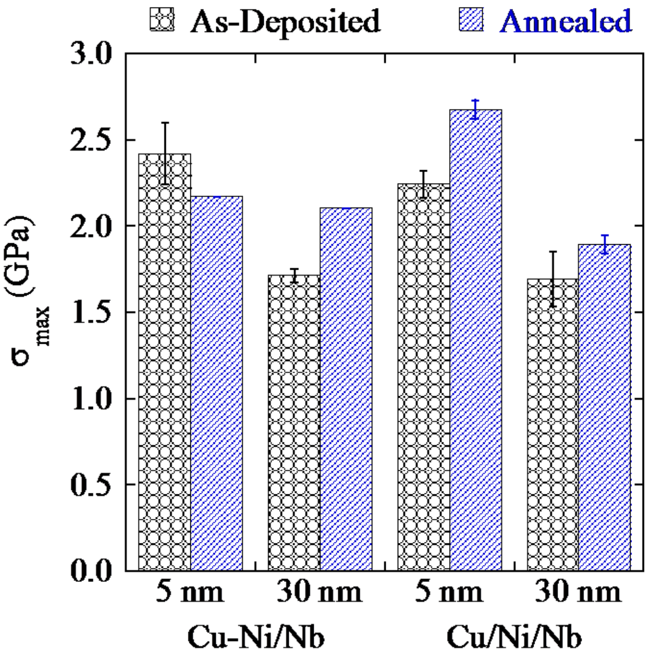

Figure 1-11. Room temperature σ_{max} values for as-deposited and annealed conditions. Error bars represent spread between two micro-pillar compression tests; values without error bars only had one compression test.

An annealing study was conducted to mimic the temperature conditions encountered during elevated temperature indentation and determine the effect of potential oxidation or alloying. If a significant amount of oxide formed during annealing, the increased room temperature hardness which was observed after annealing could be a result of a hard surface oxide layer rather than an intrinsic property of the multilayers. Therefore, XRD characterization of annealed films is a crucial step in understanding the nanoindentation results. All tri-layer films were annealed in ambient laboratory conditions at 325°C for 4 hours and then allowed to furnace cool for approximately 6 hours. To examine the effect of decreasing oxygen content, the samples were also annealed in a furnace with flowing Argon (reduced oxygen atmosphere). Both annealing atmospheres were compared to the as-deposited films to determine changes in both the XRD scans as well as nanoindentation hardness.

The films used in this study are the same as were used in the elevated temperature indentation experiment. The as deposited condition for the 30 nm film is as expected, with distinct peaks for Nb (110), Cu (111), and Ni (111) at 2θ = 38.5, 43.3, and 44.5 respectively. The 10 nm sample shows similar peaks but with more broadening, suggesting smaller grains [61], which is expected since the grain size should scale with the individual layer thickness. The substantial peak broadening in the 5 nm films causes the Cu and Ni peaks to merge and appear as a single peak with a slight shoulder on the Cu side of the peak.

X-ray diffraction (XRD) was then performed on the post-annealed films to determine the effect on the structure of the multilayers. The films were removed from the silicon substrate and attached to a glass slide prior to testing using double-sided tape. Using a Bruker D8 Focus X-Ray Diffractometer with Cu Kα source and high speed 1D Lynxeye detector, scans were run between 2θ = 20° to 80°, at 40 kV and 40 mA at a step size of 4 deg/min.

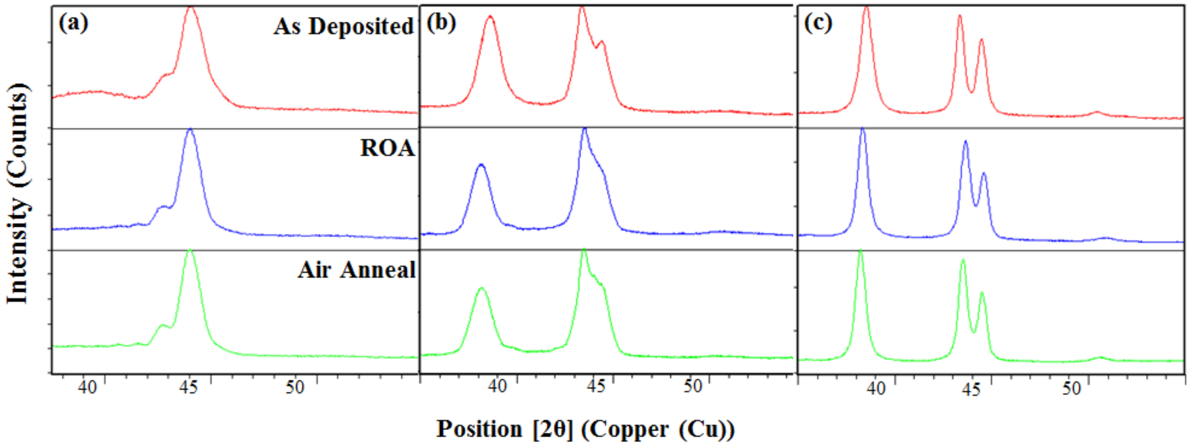

Figure 1-12. XRD scans of ex situ annealing of (a) 5 nm, (b) 10 nm and (c) 30 nm layers for as deposited, reduced oxygen atmosphere (ROA), and air anneal.

Figure 1-12 shows the XRD analysis for the 5, 10, and 30 nm samples. The 30 nm layers show a very slight change in peak ratio, but with a significant shift in the peaks as a result of annealing. The Nb peak shifts to the left of the original peak whereas the Cu and Ni peaks shift slightly to the right, indicating a developing compressive stress in the Nb layer and tensile stresses in the Cu and Ni layers. The 10 nm sample also shows significant peak shifts, which could explain the increased intensity where CuNi alloy should be. Since the Ni peak shift is nearly nonexistent and the Cu shifts to the right, closer to the Ni peak, the amount of overlap between increases and the resulting total intensity increases. However, with this technique it is impossible to determine if the increase in intensity between the two primary peaks is strictly due to the peak shift or if there is a small amount of alloying occurring between the two layers. The 5 nm film shows a completely different story than expected. In this case, the Nb peak which should be occurring around $2\theta=38.5$ is extremely broad in the as-deposited condition and essentially non-existent in the annealed conditions. The broad peak suggest an extremely small crystallite size, either signifying a small grain size or a much smaller layer thickness than what was expected. Considering the 5 nm films were deposited at a different facility than the other two films, this is not a surprising result. The disappearance of the Nb peak with annealing suggests it could have possibly combined to create intermetallic precipitates, ones that are too small to resolve with this system. Additionally, while the other films show an increase in the intensity between the Cu and Ni peak, this 5 nm films actually shows a sharpening which is most likely a result of peak narrowing due to grain growth from annealing.

CHAPTER 2 : Determining Onset of Plasticity and Phase Change Temperatures

Wafer curvature experiments were conducted on a custom machine designed and built at the Erich Schmidt Institute in Leoben, Austria. The wafer curvature chamber was put under vacuum and allowed to come to pressure for at least 20 minutes, which results in a base pressure of approximately 10^{-4}-10^{-5} Torr. Each sample was cycled up to the desired temperature and back to room temperature at a rate of 0.17°C/s for one cycle. Wafer curvature experiments were conducted on each of the films to determine the onset of plasticity and potential phase change temperatures. This technique is useful for determining the stress changes which undergo a thin film on a thick substrate due to differences in thermal expansion. By tracking relative changes in spot spacing the curvature of the sample as a whole can be determined and from there the stress in the film can be determined. The Stoney equation which uses the measured radius of curvature, R, and thickness of the substrate, t_s, and film, t_f, is used to determine the stress in the film:

$$\sigma_f = \frac{E_s {t_s}^2}{6(1-\nu)t_f R} \tag{2-1}$$

where E_s is the substrate biaxial modulus and ν is the film Poisson's ratio. As the temperature increases, the differences in the thermal expansion of the film and substrate causes the sample curvature to increase (radius of curvature decrease) and thus the stress in the film to increase.

The initial portions of the stress-temperature curves are rounded, possibly due to some relaxation of initial deposition stresses. After this small curved section, all films undergo a linear portion which correspond to elastic deformation of the film. For the multilayers in this investigation, the initial heating slope should be the same since the base components are the same and the modulus is dependent on interatomic bonds and should not be dependent on the multilayered structure. Since this doesn't change based off layer thickness, and CuNi solid solution is so close to both Cu and Ni, all elastic properties of these films should be approximately the same. After the initial elastic portion of the heating curve, the stress slowly levels out as the temperature increases, indicating the start of stress relaxation brought on by diffusion-based creep, dislocation motion, interface sliding, grain growth, or phase transformations [50], [62]–[64], most likely a mixture of multiple mechanisms depending on the stress and temperature state [65]–[67]. The stress at the onset of plasticity (σ_{min}) is unique for each film and is generally indicative of the strength of the film. However, since the yield strength is a temperature sensitive property these strengths cannot be directly compared, but rather used as a comparative study. As the temperature increases it is easier to activate thermally controlled deformation processes; therefore, the onset of plasticity is a coupled stress-temperature response with stronger films yielding at both higher stresses as well as higher temperatures. The initial cooling portion of the curve is once again indicative of the elastic response of the material, which will be approximately the same as the elastic portion of the heating slope. If a drastic change in the cooling slope is observed, it likely suggests a change in the composition of the film from annealing has occurred (e.g. development of a new phase or intermetallic).

2.1 Single Wafer Curvature Cycle to 500°C

As a first, the films were cycled up to a temperature of 500°C to examine the stress-temperature response at relatively modest temperatures and before the films delaminated. All films were heated at the same heating rate (10 °C/min) and held at the maximum temperature for 10s before cooling at the same rate (though actual cooling rate was much slower). Four different films were tested, tri-layer films and alloy films with both 5 nm and 30 nm layer thicknesses. However, the alloy films kept the “FCC” layer thickness the same as the tri-layer films with CuNi alloy being 10 nm and 60 nm thick rather than 5 nm and 30 nm, respectively.

Figure 2-1 shows the stress-temperature curves for the 500°C wafer curvature test of the tri-layers (top) and alloy (bottom) films. Each of the films show a similar initial heating curve up to the yield point, indicating similar elastic properties, with the linear slope for all the films falling within 20% of each other (See Table 2-1). After initial yielding (occurring at different temperatures depending on the film), all multilayers undergo an additional increase in compressive stress which is not normally seen in traditional wafer curvature tests. As was discussed in Chapter 1, the ideal single phase (non-phase changing) material typically exhibits one elastic heating (increasing stress with temperature) segment followed by a plastic heating (smaller increase in stress with increasing temperature) with the slope of the stress-temperature curve approaching zero while the film is plastically deforming. The presence of the additional “elbow” section in all of the films where the film starts to yield for a short time before becoming stronger again until reaching a second yield point at much higher stresses and temperatures, indicates an additional thermally activated mechanism has occurred which is not typically seen in other systems. This phenomenon could suggest the presence of a strengthening mechanism which occurs after the initial yield; whether it is brought upon by the elevated temperature or increased stress is hard to determine. This could indicate the development of intermetallic particles, strain hardening, oxidation, or a phase change is occurring in the film.

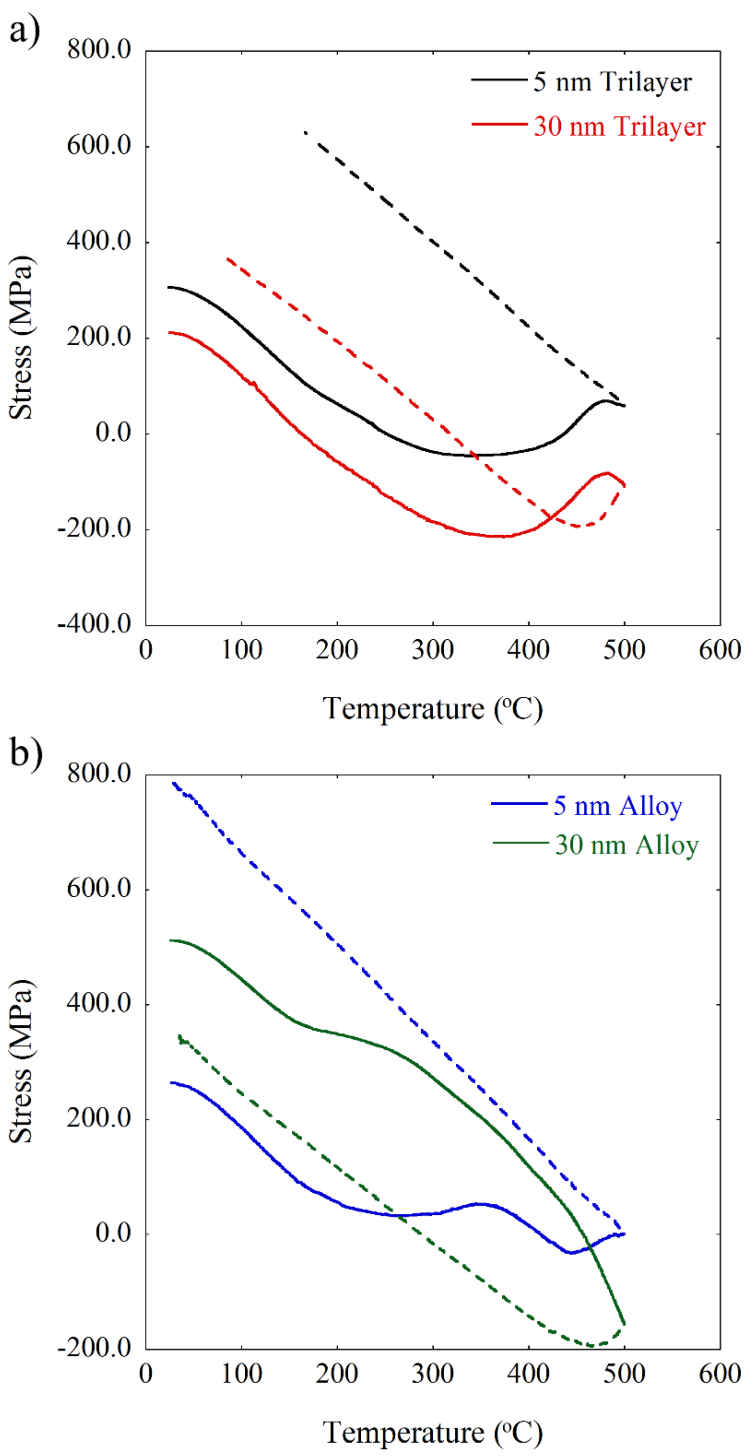

Figure 2-1. Stress-temperature profiles of (a) tri-layer films and (b) alloy films cycled to 500°C, with the solid lines showing the heating curve and the dashed line representing the cooling curve.

Another characteristic that is distinct to each sample is the temperature at which the initial plasticity initiates, T_{yield}. Since this is unique to each film and is suggestive of the film's temperature sensitivity, the higher the yield temperature, the more resistive it is to temperature induced strength degradation. As can be seen from Table 2-1, the tri-layer films show a higher resistance to elevated temperatures, with the initial yield occurring at higher temperatures than the alloy films. However, it is also possible that this effect is also directly related to the different thicknesses of the film since the alloy films are about half the thickness of the tri-layer films. The most apparent difference is between the 30 nm layers with a 50°C increase in temperature resistance in the tri-layer films while the difference between the 5 nm films is a more modest 15°C.

Table 2-1. Summary of 500°C wafer curvature results for alloy and tri-layer films

	Tri-layer		**Alloy**	
	5 nm	**30 nm**	**5 nm**	**30 nm**
σ_{max} (MPa)	629.7	378.91	785.82	346.48
σ_{min} (MPa)	-45.84	-215.28	-32.87	-195.08
T_{yield} (°C)	175.7	206.7	162.5	148.6
T_{min1} (°C)	340.6	362.6	269.5	187.5
$M_{heating}$ (MPa/°C)	-1.81	-1.80	-1.60	-1.40
$M_{cooling}$ (E) (MPa/°C)	-1.74	N/A	-1.31	N/A
$M_{cooling}$ (P) (MPa/°C)	-1.74	-1.61	-1.31	-1.68
$\Delta\sigma_{anneal}$ (MPa)	323.7	167.9	479	-135

Another interesting aspect of the 500°C wafer curvature test occurs when the films start their cooling cycle, specifically the 30 nm layer thickness films. The stresses in both the alloy and the tri-layer films continue to increase even after cooling starts. Theoretically, as the sample begins to cool the changes in the thermal expansion will reverse and the stresses should decrease.

However, for these films the compressive stresses continue to increase which further suggests that this is a thermally activated process, possibly due to the development of new phases from annealing. The fact that the 5 nm films do not show this same trend hints that whatever mechanism which is occurring in these layers has significantly slowed down or finished in the thinner layers while not in the thicker layers. This once again hints at possible alloying occurring in the system which can occur faster in the thinner layers since the diffusion distance is significantly smaller.

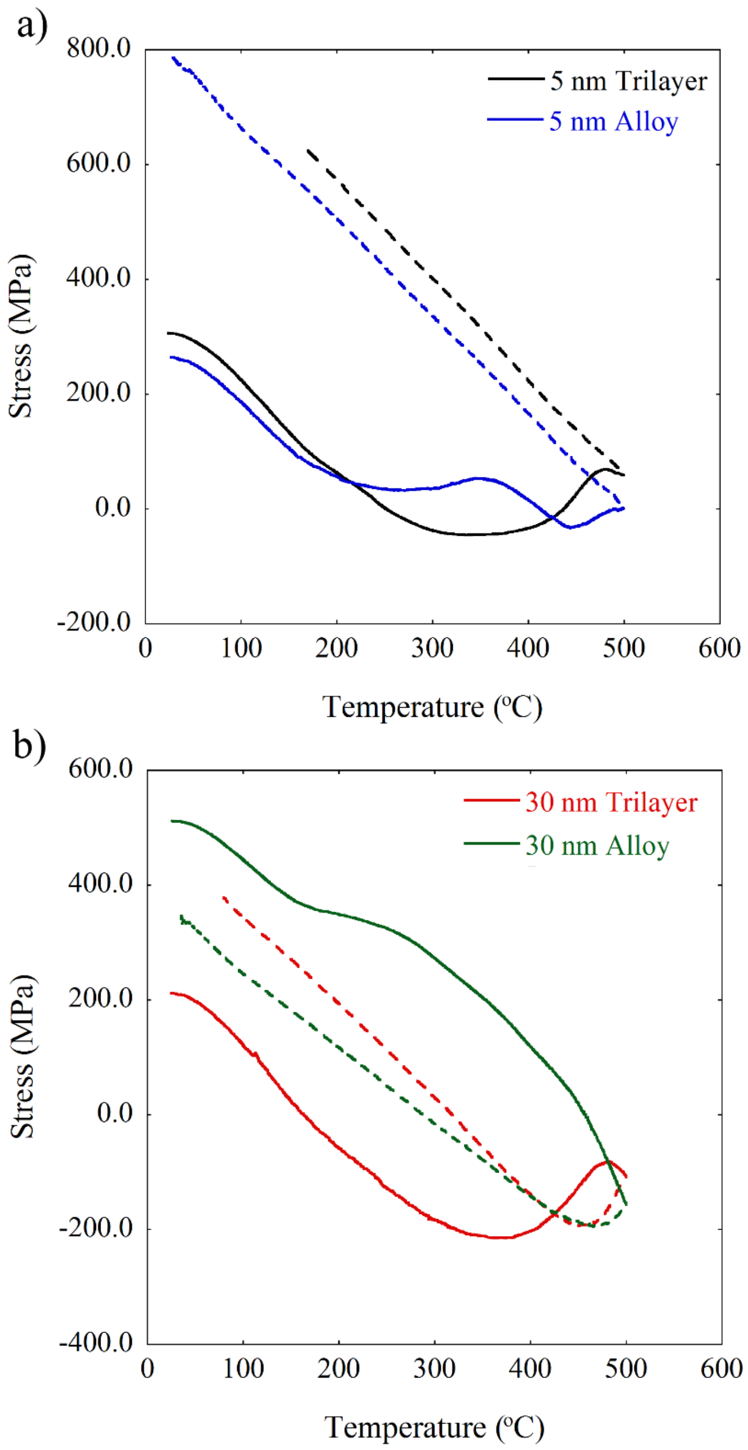

Figure 2-2. Stress-temperature profiles of samples with (a) 5 nm individual layer thickness and (b) 30 nm individual layer thickness, with the solid lines showing the heating curve and the dashed line representing the cooling curve.

Figure 2-2 shows a more direct comparison between the two interface systems, highlighting the difference specifically from the different interface structures. As can be seen from the 5 nm layer thicknesses, it is directly apparent that the alloy films begin to plastically deform before the tri-layer films. This is also seen in the 30 nm layer thicknesses with the first plastic deformation occurring nearly immediately. The cooling curves for the 5 nm films have the exact same slope, suggesting similar microstructural changes have occurred in the system, even if they initially started at different times. However, the 30 nm films show some difference in the cooling curve which could indicate the change which is occurring in the multilayers is happening at a different rate for the alloy and the tri-layer systems.

2.2 Single Wafer Curvature Cycle to 600°C

The stress-temperature profiles all of the films showed interesting behavior which started around 500°C and suggest there could be additional effects beyond 500°C. Therefore, another 600°C wafer curvature cycle was conducted on new samples to examine this possibility. Figure 2-3 shows the tri-layer films (top) and alloy films (bottom) cycled up to 600°C and verifies there is indeed additional stress increase above 500°C, with all films showing an additional dip between 500°C and 600°C The most drastic difference is seen in the 30 nm tri-layer film which shows one dip around 370°C followed by a second dip above 500°C after an additional 400 MPa increase in the stress in the film. Table 2-2 summarizes the important characteristics of these curves, including the heating/cooling slopes, yield temperature, and overall change in stress as a result of this annealing condition. Even though the samples came from the same wafer, slight variations in the thickness or local residual stresses in the film can cause a slight variation in the observed stresses.

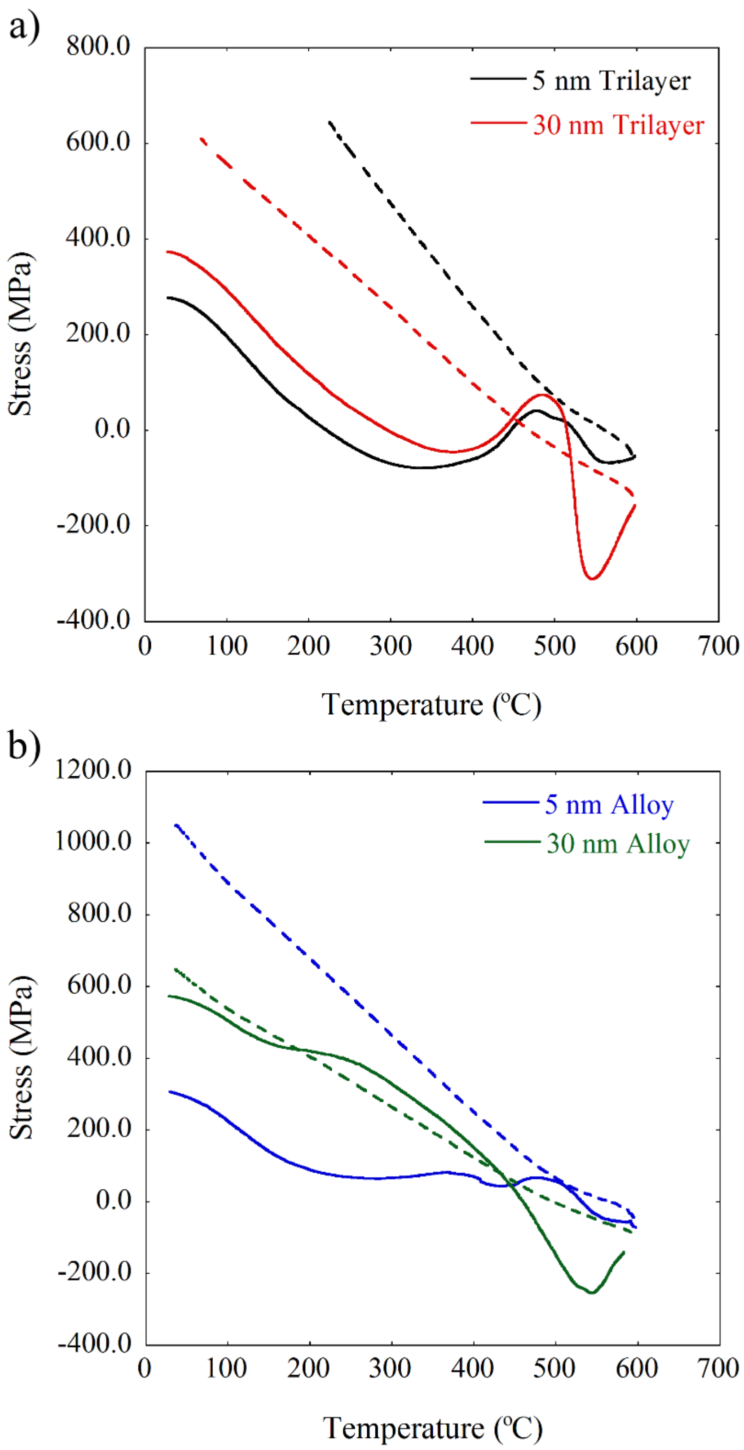

Figure 2-3. Stress-temperature profiles of tri-layer (a) and Alloy (b) films cycled to 600°C, with the solid lines showing the heating curve and the dashed line representing the cooling curve.

The same trends which were observed in the 500°C tests, are also seen at this temperature, with tri-layer films showing higher temperature resilience than the alloy films. Also, the yield temperature and temperature at the first minimum are approximately the same, ranging less the 10°C. This shows reproducibility of the results and verifies the validity of the trends observed. Once again, the 5 nm tri-layer film delaminated upon cooling as the internal stresses became too high. Interestingly, rather than the film strictly coming off of the surface of the Si wafer, the Si actually fractures below the adhesion site. This indicates the adhesion between the multilayers and Si is fairly good but the increased stress in the multilayers causes too much shear stress just below the Si surface that the Si fractures instead.

Table 2-2. Summary of 600°C wafer curvature results for alloy and tri-layer films

	Tri-layer		**Alloy**	
	5 nm	**30 nm**	**5 nm**	**30 nm**
σ_{max} (MPa)	N/A*	621.21	1050.7	651.4
σ_{min} (MPa)	-79.27	-311.16	-71.63	-257.82
T_{yield} (°C)	169	193	158	140
T_{min1} (°C)	335	375	283	187
$M_{heating}$ (MPa/°C)	-1.84	-1.82	-1.70	-1.51
$M_{cooling}$ (E) (MPa/°C)	-2.53	-2.67	-3.55	-1.65
$M_{cooling}$ (P) (MPa/°C)	-2.15	-1.56	-2.19	-1.41
$\Delta\sigma_{anneal}$ (MPa)	N/A*	248	743	79

*Delaminated before reaching room temperature

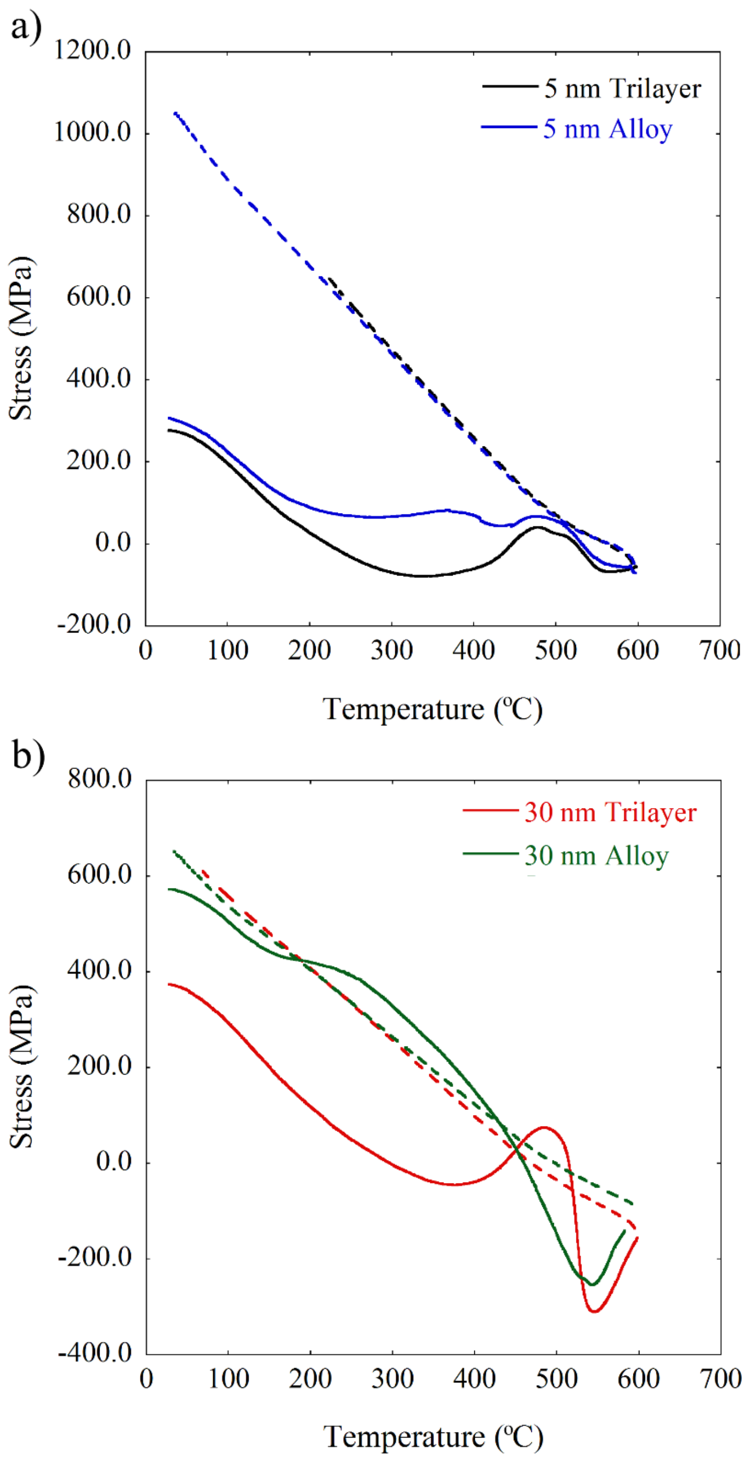

Figure 2-4. Stress-temperature profiles of samples with (a) 5 nm individual layer thickness and (b) 30 nm individual layer thickness cycled to 600°C, with solid lines indicating the heating curve and the dashed line representing the cooling curve.

When comparing directly between films with the same layer thickness, the differences in the temperature sensitivity are once again quite apparent. As the temperature increases above 500°C, the 5 nm films start to resemble each other quite closely, following essentially the same heating and cooling path. The difference between these two films occurs before 500°C, indicating the change in microstructure has already occurred in the thinner samples. The 30 nm films are still significantly different up until about 550°C, where they start to behave similarly. The most apparent difference between the tri-layer and alloy films is the much larger dip which occurs between 500°C and 600°C in the heating curve for the tri-layer film, which isn't present in the alloy film (or at least occurs at a much lower temperature).

The mechanism behind the multiple dips in the heating curves is still unknown. Previous studies conducted on passivated and unpassivated Cu films show similar stress drop response; however, that system does not show the second drastic increase as is seen in these multilayer films. The stress drop in the unpassivated Cu film is attributed to grain boundary diffusion [68], [69]. There are a range of possibilities which could lead to the observed stress drop (grain growth, diffusion processes, dislocation motion, twinning, phase transformation, etc.) and more in depth investigations are required. All of these methods are highly likely in these multilayer systems, though combined with the significant increase in strength after the initial "dip" points strongly to a mechanism which would also increase the strength of the multilayer such as the development of intermetallics or strain hardening.

CHAPTER 3 : Determining Change in Microstructure, Alloying, and Internal Stresses

3.1. As-Deposited Microstructure Determined from XRD

X-ray diffraction (XRD) scans were conducted using a Bruker system with a Cu α x-ray source in a range of 30°-100° at a resolution of 0.04° and a speed of 1.3°/min. The samples were placed on a flat stage and measured using the line source and through a 5 mm filter. All measured scans were compared to known standards of star or calculated quality based on the possible intermetallics and alloys which can develop from this tri-component system. From the phase diagrams, both Ni_3Nb and Ni_6Nb_7 intermetallics can possibly develop at the Nb/Ni interface. The formation of a copper silicide is also distinctly possible if the Cu is able to diffuse through the Nb bottom layer to the Si substrate as has been seen in recent investigations. Since the first layer is polycrystalline Nb, followed by the Cu layer, the likelihood of some diffusion along the grain boundaries to the substrate is probable, even if the miscibility of Cu in Nb is very small.

Figure 3-1 shows the as deposited XRD scans for 5 nm and 30 nm tri-layer films. Both films are highly textured which is typical for physical vapor deposited metal films [70], with BCC Nb showing strong (110) texture and FCC Cu and Ni showing a strong (111) texture. The secondary (220) and (222) peaks are also visible between 80° and 100°, slightly more spread out so the peaks are more distinguishable. The 5 nm films also show substantial peak broadening as a result of the smaller layer thicknesses (similar to peak broadening as a result of small grains/crystallites). In both tri-layer and alloy films the Nb layer also shows additional (100), though at a much lower intensity than the (110) peak.

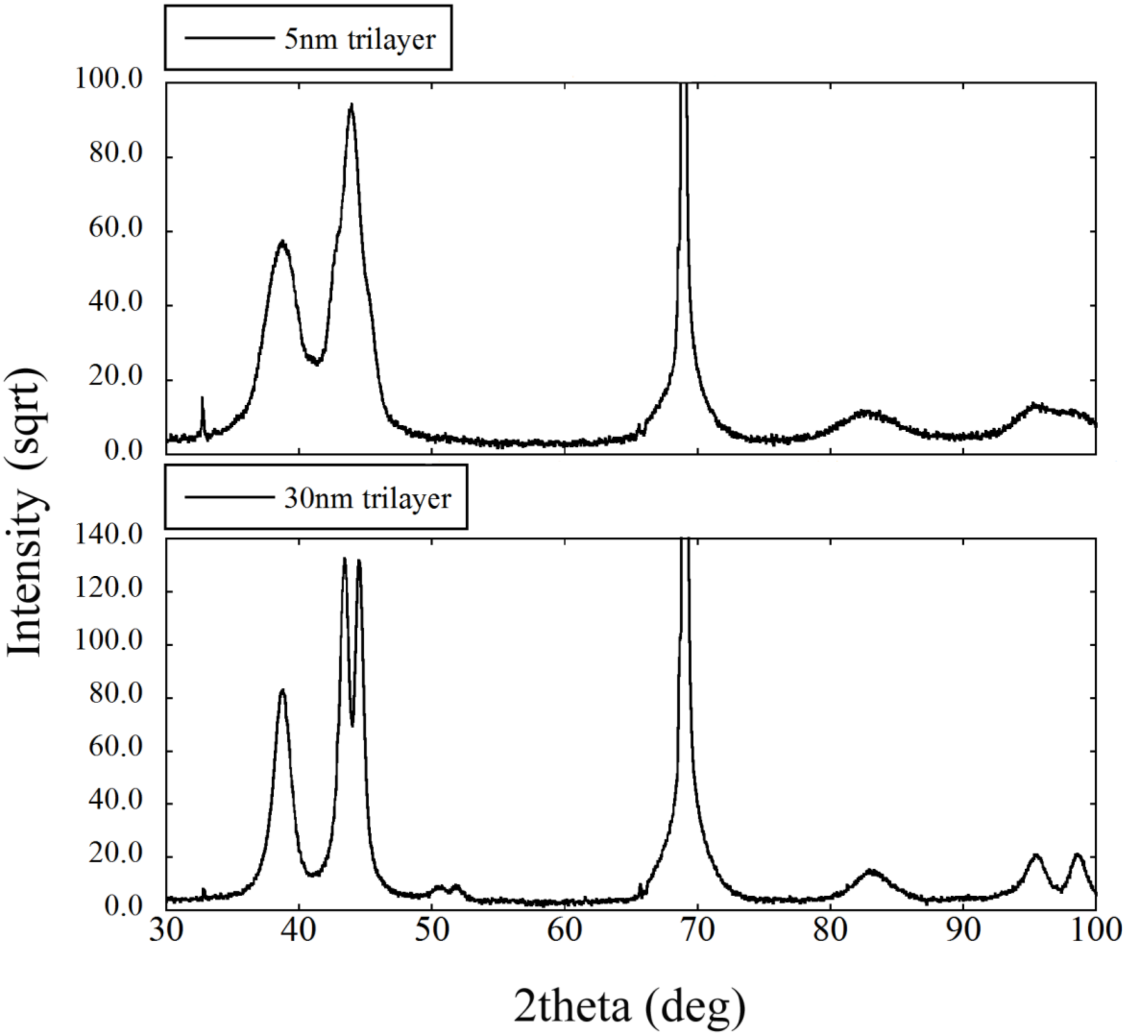

Figure 3-1. X-ray diffraction experiments showing structure of Cu/Ni/Nb tri-layer films with 5 nm (top) and 30 nm (bottom) layer thicknesses. Peak merging from two different materials that exhibit large peak broadening can result in a shoulder, as is seen on the 5 nm scan.

The 5 nm tri-layer sample does not show distinct Cu and Ni peaks, which at first glance seems to be a result of alloying of the Cu and Ni layers. However, as was briefly mentioned earlier, as the layer thickness decreases the crystallite size also decreases and thus causes significant peak broadening, as is specifically apparent in the Nb peak. When there is broadening of two peaks that are very close together, the signals can overlap and add intensities, schematically depicted in Figure 3-2. When this happens there will be shoulders on the combined peak from the portions of the individual peaks that were not overlapping. This is seen on both sides of the 5 nm “Cu/Ni” combined peak, more noticeably on the Cu side of the peak that is circled in the Figure. While this doesn’t necessarily guarantee the layers are completely discrete, it does show that the layers are not fully alloyed from the beginning. Once again, the Nb peak is shifted slightly to the right, indicating a tensile stress exists in the as deposited film.

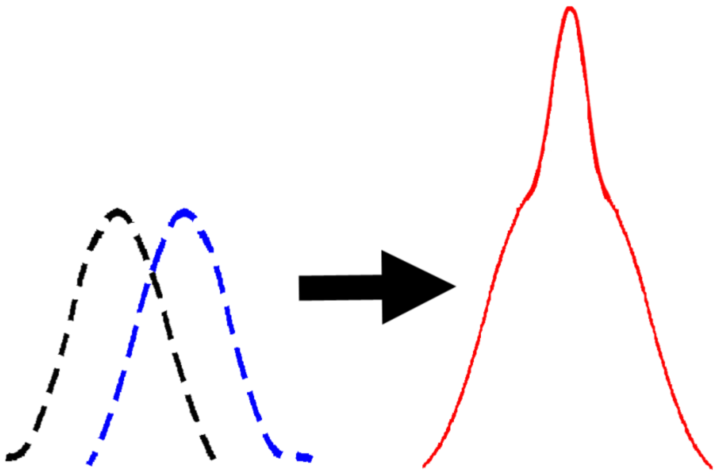

Figure 3-2. Schematic of how merging XRD elemental peaks can combine to create a merged peak with shoulders as is seen in the as-deposited 5 nm tri-layer sample and later in some of the annealed films.

The 30 nm films show very discrete peaks from each of the layers, corresponding to (110) Nb (green- 38.5), (111) Cu, (red- 43.3), and (111) Ni (blue- 44.5). All three peaks are shifted slightly to the right of the reference peaks indicating a tensile strain in the film. The extent of the peak shift is different for each peak, indicating a different amount of initial stress in the layers, likely due to slightly mismatched lattice constants which can create their own strains across a coherent interface. In order to ensure coherency there would need to be a shortening of the lattice constant in one layer (Cu) and a lengthening in the other (Ni). This would lead to a stronger shift of the Cu peak to the right than the Ni peak (which is only slightly shifted from the reference pattern). The strong shift in the Nb peak could be due to the overall tensile stress in the film or could be additional stresses in the individual Nb layers as a result of the deposition conditions. The strong peak seen at approximately 2θ= 70° belongs to the single crystal Si substrate, a minor shift is also seen at this peak from the reference value, which could be due to either stresses caused by the thin film or from being slightly off planar due to bowing or small defects on the bottom surface.

As-deposited Cu-Ni/Nb alloy films were also inspected using XRD to compare structure and intrinsic stress to the tri-layer films (Figure 3-3). The 30 nm film shows two distinct peaks, one from the Nb layer and the other from the Cu-Ni alloy. Once again, the third peak in the scan is the second diffraction peak belonging to the Nb (220), which is often seen in highly textured samples. The Cu-Ni alloy peak is also shifted slightly to the right of the reference peaks, once again indicating a slight tensile stress in the film. These films also show significant peak broadening in the Nb layer while only a slight broadening in the Cu-Ni alloy. Since the CuNi alloy layer is twice the thickness of the Cu or Ni layers in the tri-layer film, the observed crystallite size can also be twice that of the tri-layer films leading to less peak broadening. The two alloy films have a remarkably consistent microstructure with similar texture, though different amounts of peak broadening which results in less peaks in higher 2θ angles for the 5 nm film.

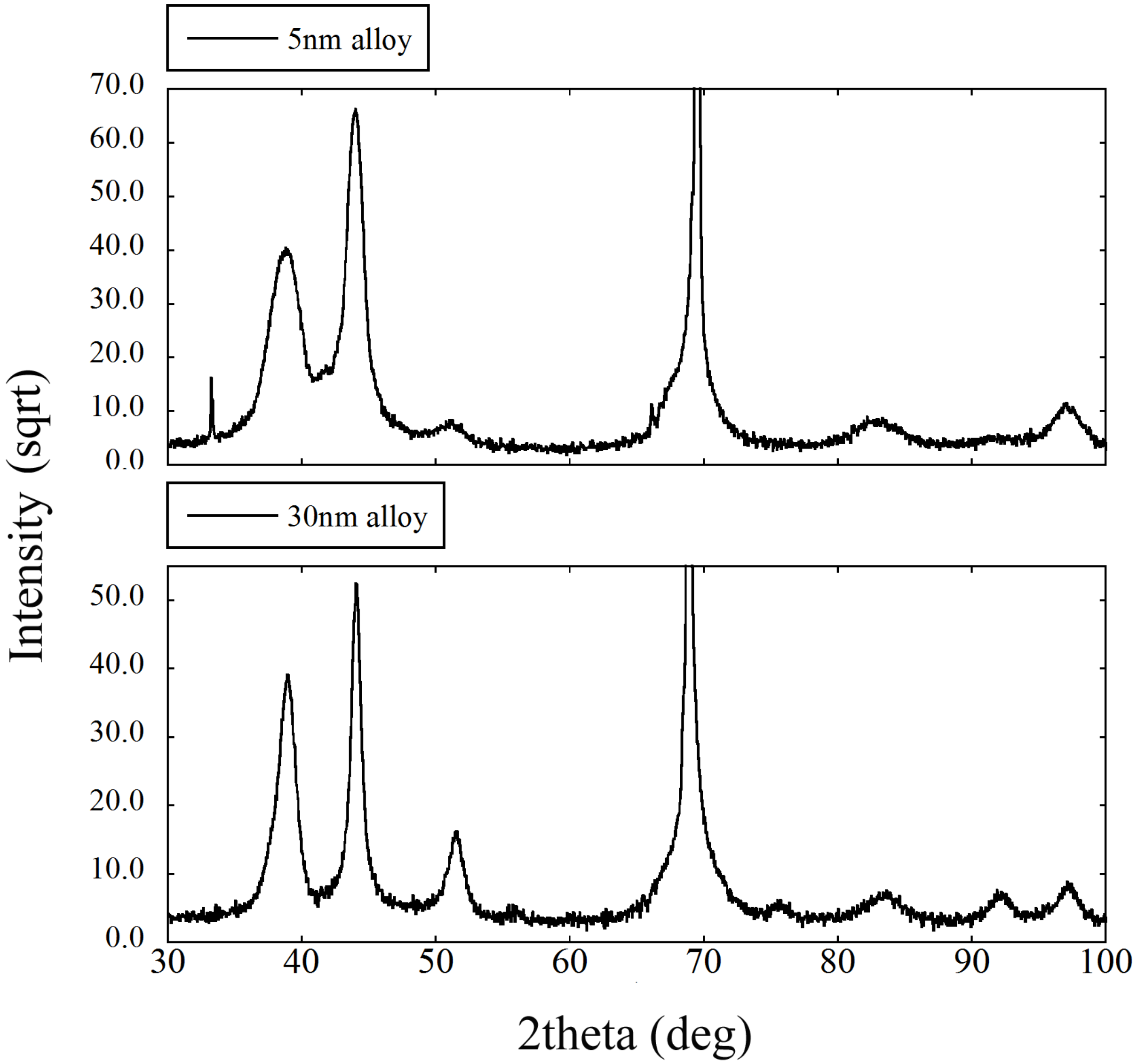

Figure 3-3. XRD scans of CuNi/Nb bi-layer films with individual layer thicknesses of 5 nm (top) and 30 nm (bottom). Scans show highly textured orientation for both layer thicknesses with predominately (100) for Nb and (111) for CuNi alloy.

The relative peak ratios for the four different films are summarized in Table 3-1 and will be used as a comparison to the annealed films, which will help determine the extent of alloying which might be occurring in the films. While the ratio for the tri-layer films is not 1:1:1, this relates both to the degree of texture as well as the thickness of the individual layers. The layer which has a weaker texture will have a smaller than expected peak intensity even if the overall thickness is the same. Therefore, these peak ratios are to be used as comparison between alloyed films and the starting microstructure.

Table 3-1. As-deposited peak ratios of tri-component multilayers.

	Cu/Ni/Nb Trilayers		Cu-Ni/Nb Alloy	
	5 nm	30 nm	5 nm	30 nm
Cu:Ni:Nb (Cu-Ni:Nb)	n/a	1 : 1 : 0.63	1 : 0.61	1 : 0.77

3.2. Microstructural Evolution Resulting from 300°C Anneal

From the wafer curvature results, all four films show a slight deviation from elastic behavior at a temperature of 300°C with the alloy films showing obvious plastic deformation beginning as early at 175°C. Since it is unknown what exact mechanism is causing the plastic deformation at such low temperatures in the alloy films the XRD investigations could possibly shed light as to whether it is due to grain growth rather than dislocation propagation, grain boundary diffusion, or creep. While extremely small particles or the formation of a very thin intermetallic layer would be extremely difficult to see in traditional theta-2theta scans, pronounced amounts of alloying or intermetallic formation should be visible. For the 300°C annealing condition, three different annealing times (1 hr, 3 hr, and 12 hr) were investigated to determine if there was a peak strengthening change which can be linked to specific microstructural changes in the film. Due to testing complications, the 30 nm alloy film was not annealed for 3 hours and the 5 nm tri-layer film annealed for 12 hours delaminated before any further tests could be conducted.

3.2.1. 5 nm Tri-layer

In general, the thinnest tri-layer film showed a considerable amount of instability under high temperatures and long annealing times. Even at 300°C, which is on the brink of the plastic response in the wafer curvature results, the film delaminated from the silicon substrate. Figure 3-4 shows the XRD scans of the 5 nm tri-layer samples annealed at 300°C, at a range of different times and compared to the as deposited microstructure. The as-deposited microstructure (top-black) shows merging of the Cu and Ni (111) peaks due to the extremely small crystallite size, which can be compared to the layer thickness, and the similar lattice constants (and thus the 2θ diffraction angle). For this reason any alloying which occurred during deposition conditions would be masked by the merging peaks. The second diffraction peak corresponding to the (444) crystallographic orientation has a much smaller intensity, but the Cu and Ni peaks are further apart from each other, making the individual peaks a bit more discernable. Even though the peaks are still merging there are now two separate high points instead of one peak with two shoulders, making it easier to determine if the Cu and Ni layers are starting to alloy.

Examination of the annealed XRD scans in Figure 3-3 shows the beginning of alloy formation in the (444) collection of peaks even after only one hour. Since the films were annealed at a rate of 10°C/min and left to furnace cool, each sample was at an elevated temperature for a longer time than what it is labeled. As can be seen in the 1 hour XRD scan, there seems to be the start an additional peak in between the Cu and Ni (444) peaks, belonging to CuNi alloy (444). Although there isn't a distinct peak, the valley seen in the as-deposited sample has disappeared which suggests the CuNi peak is beginning to emerge. Furthermore, there are two additional peaks: one just to the left of the Cu peak and the other barely discernible to the left of the strong silicon peak both of which are a result of annealing and diffusion of the different atoms diffusing into the neighboring layers. After 3 hours at 300°C the peaks which were seen in the 1 hour sample are more pronounced. The CuNi (444) peak is now much more distinguished from the Cu and Ni peaks, showing there is significant amount of alloying as a result of the Cu/Ni layers diffusing. The ratios of these three (444) peaks is approximately 1:1:1 and assuming the crystallite sizes are approximately the same, the thickness of the pure Cu, Ni, and CuNi alloy layers are approximately the same. The peaks to the left of Cu and Si also increased in intensity, indicating larger precipitates or thicker layers have developed from the increased annealing time. This sample was also annealed for 12 hours at 300°C but ended up delaminating immediately following being removed from the furnace; therefore, the XRD data for this condition could not be collected.

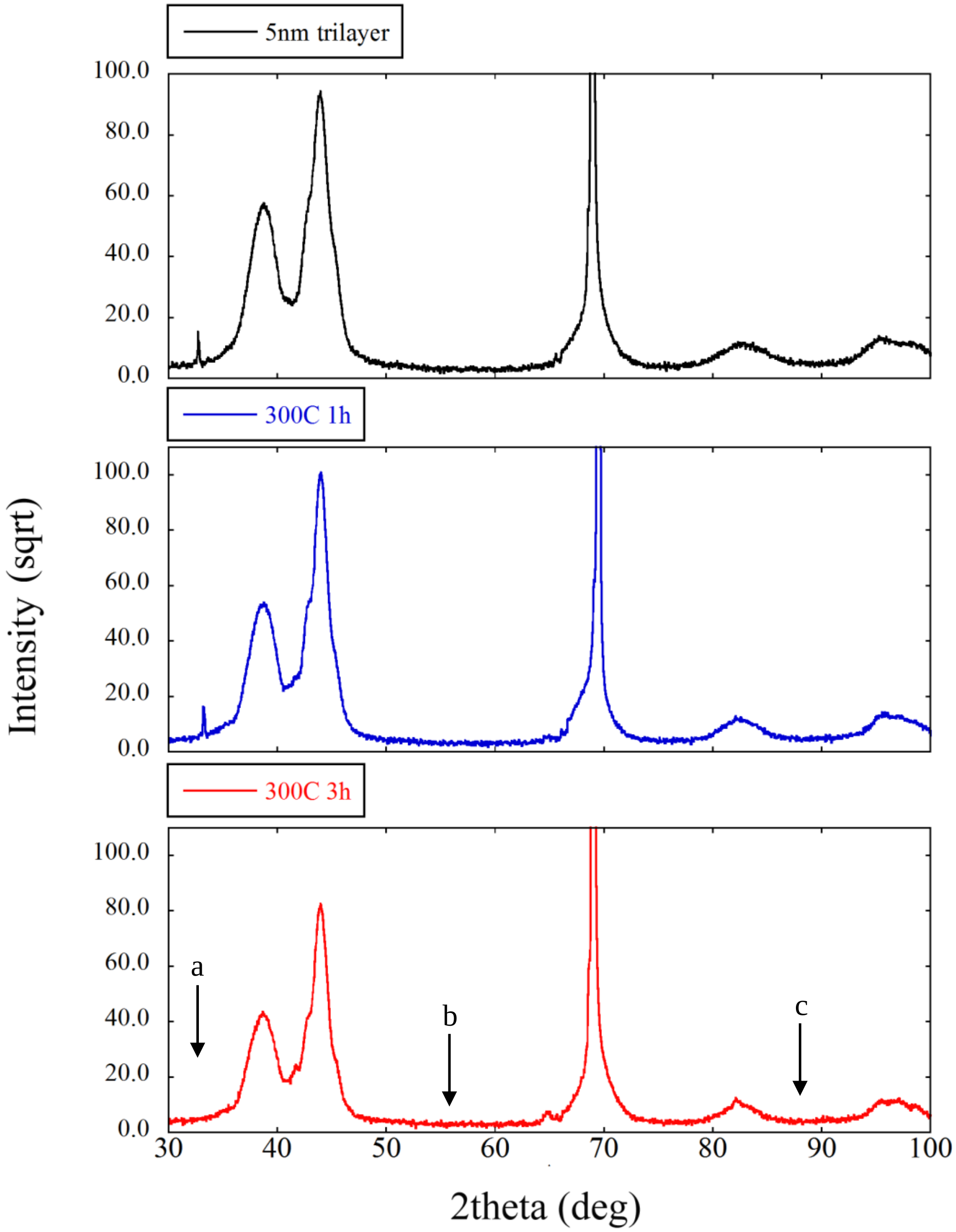

Figure 3-4. Summary of 300°C annealing temperature on the microstructure of 5 nm tri-layer films, showing room temperature (top), 1 hr (middle), and 3 hr (bottom) annealing times. The 12 hr annealing time delaminated from the substrate. The peaks which develop as a result of annealing are highlighted with black arrows in the 3 hr scan.

3.2.2. 30 nm Tri-layer

The same annealing conditions were applied to the 30 nm tri-layer film and the resulting XRD scans are shown in Figure 3-4, once again with the as-deposited condition provided as a comparison. As was discussed previously, the Cu, Ni, and Nb peaks are much sharper and thus the Cu and Ni (111) peaks are much more distinct, allowing nearly full separation of the Cu and Ni peaks both in the lower 2θ range as well as the secondary diffraction peaks. Examining the 300°C 1 hr annealing condition, the majority of the elemental peaks remain unchanged, though with the addition of an unidentified peak just to the left of the Si (100) substrate peak, indicating this annealing condition is not sufficient enough to create large enough NiNb intermetallic or CuNi alloy layer. Interestingly, the 12 hour annealing condition does not show a significant change in the XRD scans, with the exception of a substantial decrease in the relative Ni peak when compared to the as-deposited condition. This shows that while the 300°C annealing temperature is low enough that changes in the microstructure occur at a very slow rate, over time the multilayers will indeed begin to alloy and create additional intermetallic layers. Additionally, as the annealing time increases the amount of internal stress in the film continually increases which can be seen from the shifts in the peaks compared to the as-deposited structure. The increasing amount of stress in the longer annealed film is also apparent from the ease at which the film delaminates from the surface, with some samples delaminating before any tests could be conducted.

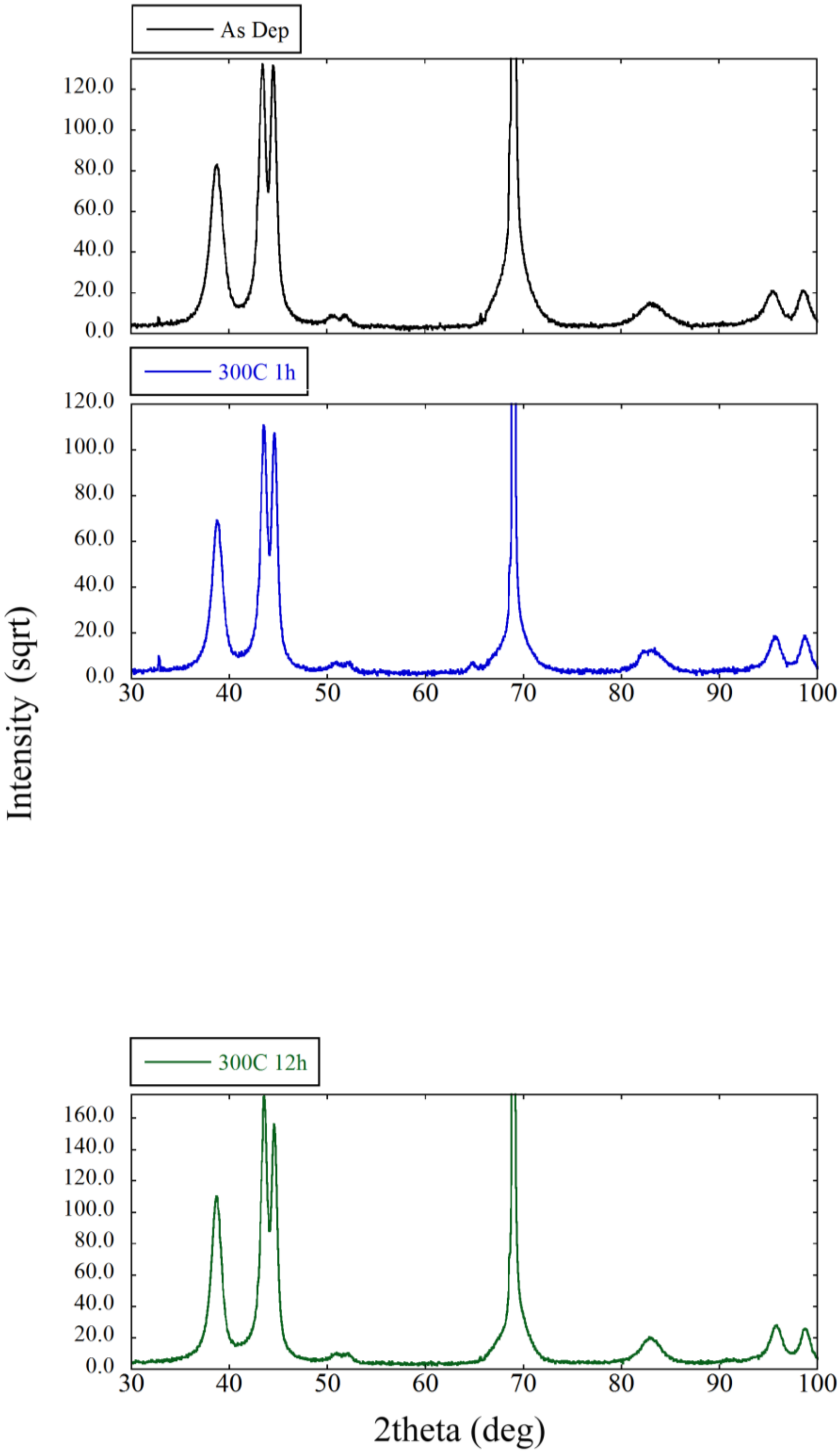

Figure 3-5. XRD scans of 30 nm tri-layer sample annealed at 300°C for 1hr (blue), 3 hrs (red-data unavailable), and 12 hrs (green) and compared to the as-deposited condition shown in black.

The peak ratios for each of the 300°C annealing temperature for the 30 nm tri-layer film is summarized in Table 3-2, and compared to the as-deposited peak ratios. As the ratio of the elemental peaks changes there is a high likelihood that some of the initially pure layers have begun to alloy or create intermetallics, otherwise the peak ratio would remain the same regardless of the annealing conditions. The Ni (111) peak specifically decreases more than the other two layers indicating more interactions are occurring with this element and the other two. Since the Ni can both alloy with Cu to create CuNi and form an intermetallic with Nb, it is difficult to conclude which is occurring strictly from the XRD measurements. In all likelihood, it is a combination of both reactions, although the Ni_xNb_y particles/layers are too small for the resolution of this system.

Table 3-2. Peak ratios of primary Cu, Ni, and Nb elemental peaks in 30 nm tri-layer XRD scans from different annealing conditions at 300°C.

Annealing Condition	Peak Ratio (Cu:Ni:Nb)
As-deposited	1 : 1 : 0.63
300°C 1 hr	1 : 0.96 : 0.63
300°C 3 hr	n/a
300°C 12 hr	1 : 0.9 : 0.63

3.2.3. 5 nm Alloy

The CuNi/Nb alloy bilayer films were also annealed at the same temperature and for the same amount of time to compare with the tri-layer films. Figure 3-5 shows the change in the 5 nm film microstructure which occurred after the 3 different annealing times and compared to the as-deposited conditions (top). All three of the annealed conditions show similar peaks which developed in the tri-layer films at the longer annealing times, most noticeably the (a) peak. Since this peak most likely corresponds to the NbNi intermetallic formation, it suggests the alloy films start forming the intermetallic much sooner than the tri-layer films, either at a lower temperature or at very short times. Since the Ni atoms in the alloy are already adjacent to the Nb layer on both sides, the reaction can occur at both interfaces and therefore can interact faster than in the tri-layer films which have to wait for the Ni to diffuse through the Cu layer in order to reach the second Nb interface. Since this sample starts as a CuNi alloy the (c) peak which developed in the tri-layer films will not be observed in the annealed conditions for the alloy films. Examination of the Si peak in the different annealing conditions in Figure 3-5 suggests that the 3 hr sample was slightly misaligned since the (100) peak isn't as strong as in the other conditions even though no microstructural change would have occurred in the substrate.

The microstructure of this films seems to be fully evolved after 1 hour at 300°C since little to no change is observed in the peaks with increasing time at this temperature (supported by the peak ratios summarized in Table 3-3). The extremely sharp peak of unknown origin at 33° seems to be especially prevalent at the longer annealing time, though since this peak is seen in some as-deposited samples (5 nm tri-layer, 30 nm tri-layer,) as well as annealed samples it indicates this peak is most likely not a new phase or alloy/intermetallic.

Table 3-3. Peak ratios of primary CuNi, and Nb elemental peaks in 5 nm alloy XRD scans from different annealing conditions at 300°C.

Annealing Condition	Peak Ratio (Cu-Ni:Nb)
As-deposited	1 : 0.61
300°C 1 hr	1 : 0.54
300°C 3 hr	1 : 0.51
300°C 12 hr	1 : 0.49

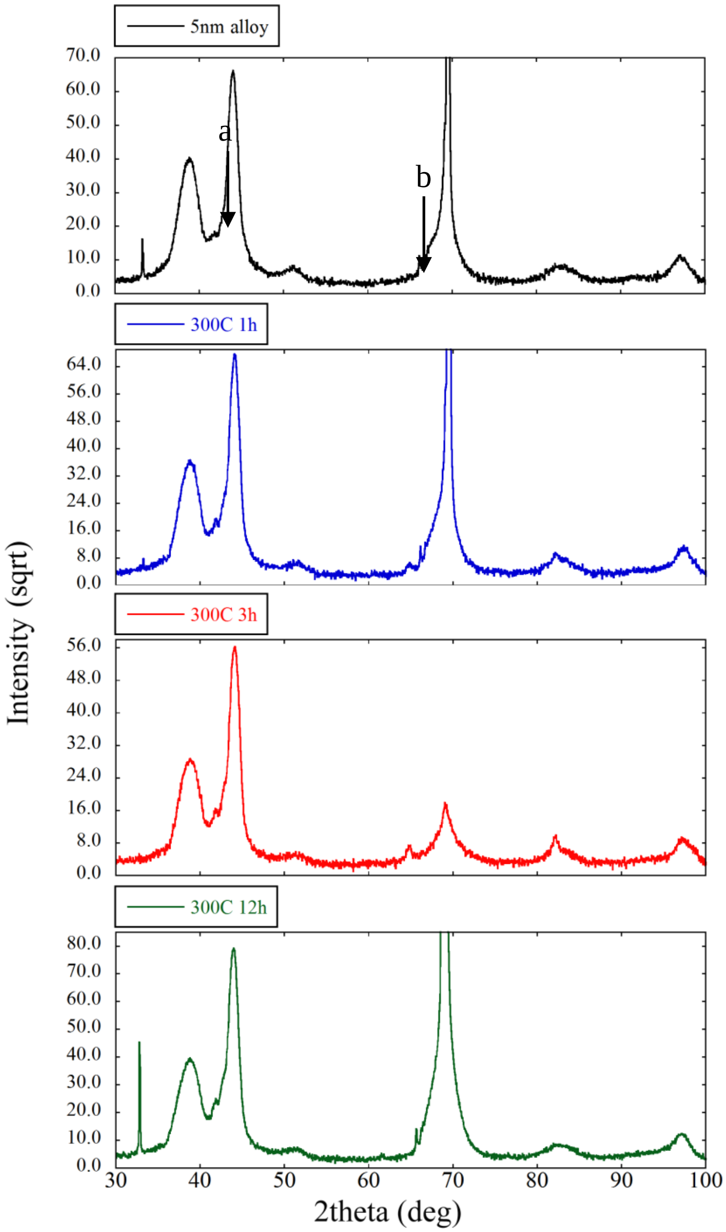

Figure 3-6. 5 nm alloy film annealed at 300°C for a range of annealing times. A slight peak (highlighted with black arrow) is already observed in the as-deposited condition in between the Nb and CuNi peaks; however the intensity of this peak increases as annealing time increases. An additional unidentified peak near the Si (100) peak is observed in the annealed films which is not present in the as-deposited condition (top).

3.2.4. 30 nm Alloy

Finally, the 30 nm alloy was annealed under the same conditions, with the exception of the 3hr annealing condition. The corresponding XRD scans are shown in Figure 3-6, once again including the as-deposited scan included for a direct comparison to the annealed samples. While there does not seem to be any drastically obvious change in the microstructure, there does seem to be a faint peak (highlighted with the black arrow), which results in a shoulder on the left side of the Nb peak. While the peak isn't as prominent in the 12 hr anneal condition, the asymmetry in the Nb peak is still there. To further prove the development of a new alloy, Table 3-4 shows the peak ratios of the CuNi:Nb peak. As the annealing time increases, the relative intensity of the Nb peak continues to decrease, indicating some of the Nb which was once as a discrete layer is now being consumed and changed to another compound, most likely some form of Ni_xNb_y intermetallic.

Table 3-4. Peak ratios of primary CuNi, and Nb elemental peaks in 30 nm XRD scans from different annealing conditions at 300°C.

Annealing Condition	Peak Ratio (Cu-Ni:Nb)
As-deposited	1 : 0.77
300°C 1 hr	1 : 0.71
300°C 3 hr	n/a
300°C 12 hr	1 : 0.72

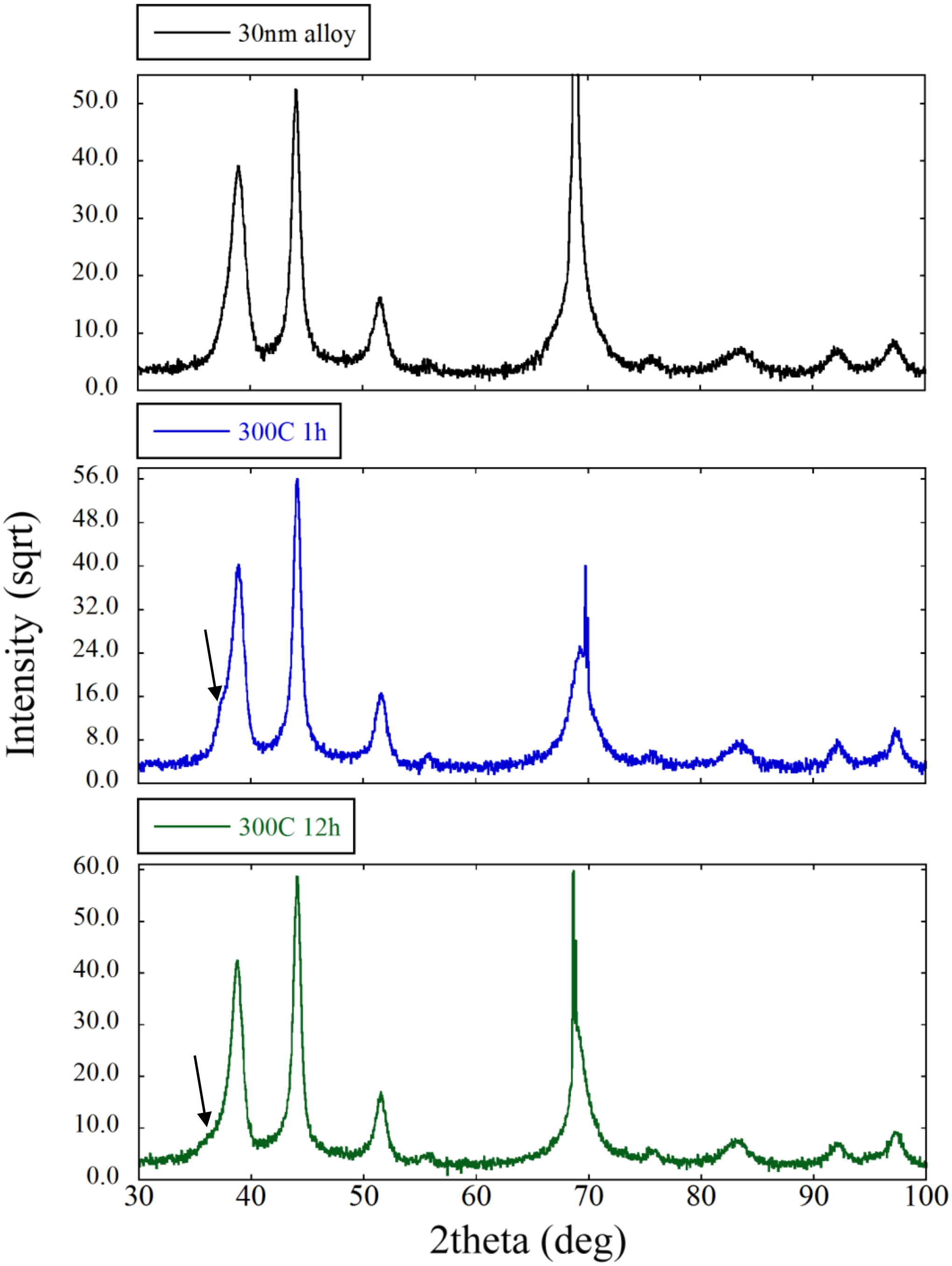

Figure 3-7. XRD scans of 30 nm alloy film in the as-deposited (top), and annealed at 300°C for 1hr (middle) and 12 hr (bottom). Increasing intensities of the (a), (b), and (c) peaks indicates a microstructural change in the film as a result of increased annealing time.

3.3. Vacuum annealing up to 200°C

As was seen from the wafer curvature results, the alloy films start to deviate from linearity at a much lower temperature than the tri-layer films. However, it is unknown what process is behind that first plasticity event whether it is from diffusion, dislocation motion, creep, or grain growth. Therefore, the different films were annealed at a temperature which was above the inflection point in the alloy films but below that of the tri-layer films. All films were vacuum annealed for 3 hours at 200°C at the same heating rate as was used in the 300°C annealing study followed by a furnace cool back down to room temperature before being removed from the vacuum furnace.

Figure 3-7 shows the XRD results from this annealing condition with the 5 nm films above the 30 nm films and the tri-layer films above the alloy films. The tri-layer films show no additional peaks and no substantial change in peak ratios from the as-deposited condition, indicating no change in the microstructure of the film, which since the stress-temperature profile remained linear (elastic response) is not surprising. Whereas, the 5 nm alloy film shows the same peak which developed in the 300°C annealed films (emphasized with a black arrow in the figure. Since the additional peaks in the alloy film show the beginnings of a changing microstructure, this indicates the inflection point observed in the wafer curvature stress-temperature profiles is likely a result of diffusion and/or the development of a new alloy. Both of these observations indicate that the alloy films are more susceptible to structural degradation from annealing than the tri-layer films.

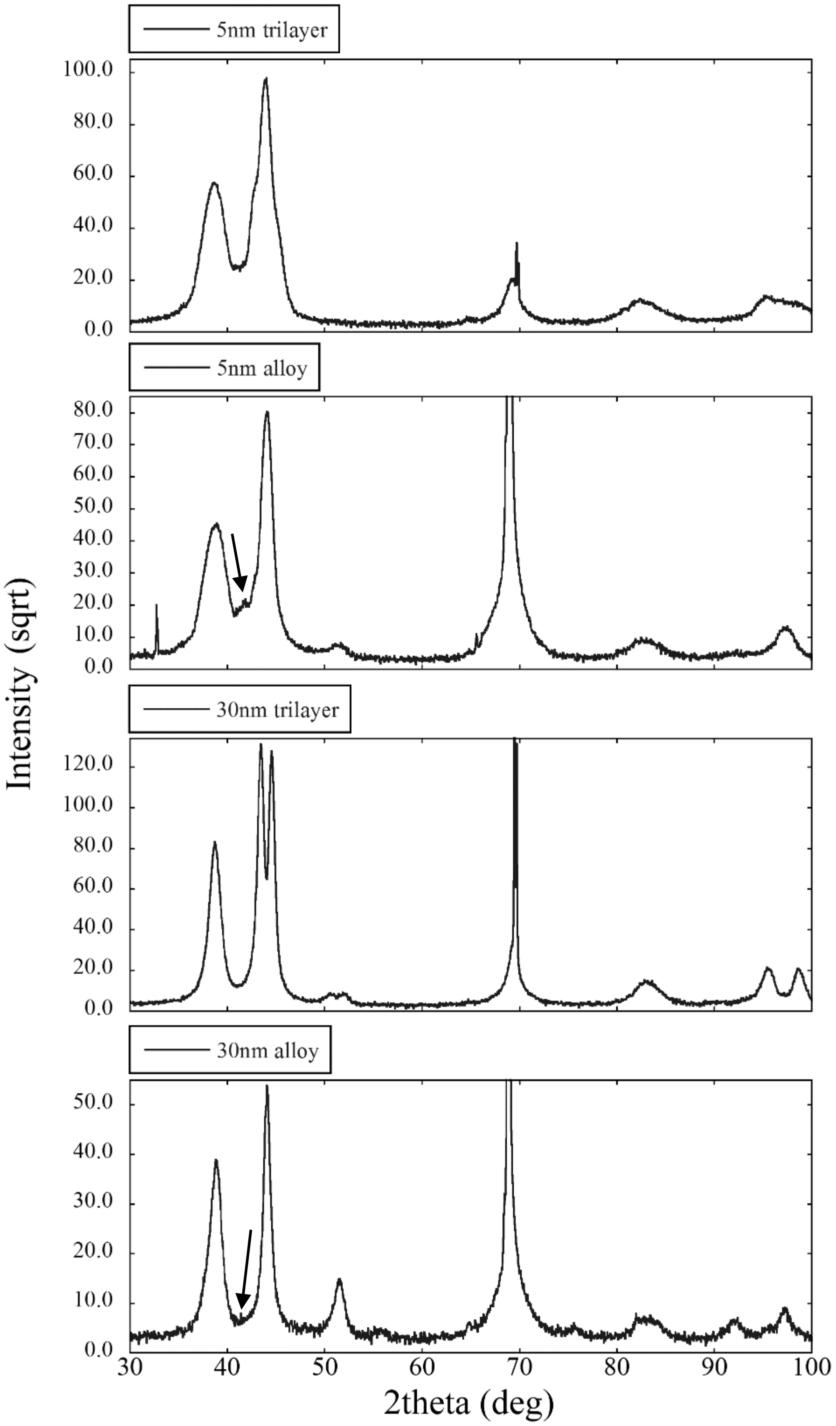

Figure 3-8. XRD scans of 5 nm tri-layer, 5 nm alloy, 30 nm tri-layer, and 30 nm alloy (from top to bottom respectively) films annealed at 200°C for 3 hours. Additional peaks which are not present in as-deposited films are emphasized with a black arrow.

3.4. Microstructural changes after wafer curvature cycles to 500°C and 600°C

As was shown in Chapter 2, all of the films were cycled up to 500°C and 600°C using the wafer curvature technique under mild vacuum conditions. The stress-temperature profiles suggest a drastic microstructural change is occurring in the films above 500°C, where a large increase in stress follows the initial stress drop. The stress drop can easily be attributed to diffusion, dislocation motion, grain growth or other such relaxation mechanisms; however, the following increase in stress at a certain point suggest a strengthening in the film as the temperature continues to increase. The temperature at which this stress increase starts is similar in the tri-layer films (approximately 475°C). The alloy films show a slightly different behavior where the 5 nm sample undulates between 375°C and 500°C before the last stress increase at 550°C; whereas the 30 nm sample shows a slow stress increase after 200°C up until 550°C.

XRD scans of these films are shown in Figure 3-8 (500°C) and Figure 3-9 (600°C), though the 5 nm tri-layer film delaminated before scans could be performed. After the 500°C anneal it is apparent that a change is beginning to occur in the Cu and Ni layers of the tri-layer film. What were once distinct peaks in the as-deposited condition are now starting to merge either via diffusion (creating CuNi alloy) or changes in relative stresses of the layers bringing them closer to one another. The 30 nm alloy films doesn’t show a drastic change in the XRD profile from the as-deposited condition except for the emergence of a very broad peak just to the left of the Nb peak, likely the first signs of a very thin Ni_xNb_y layer.

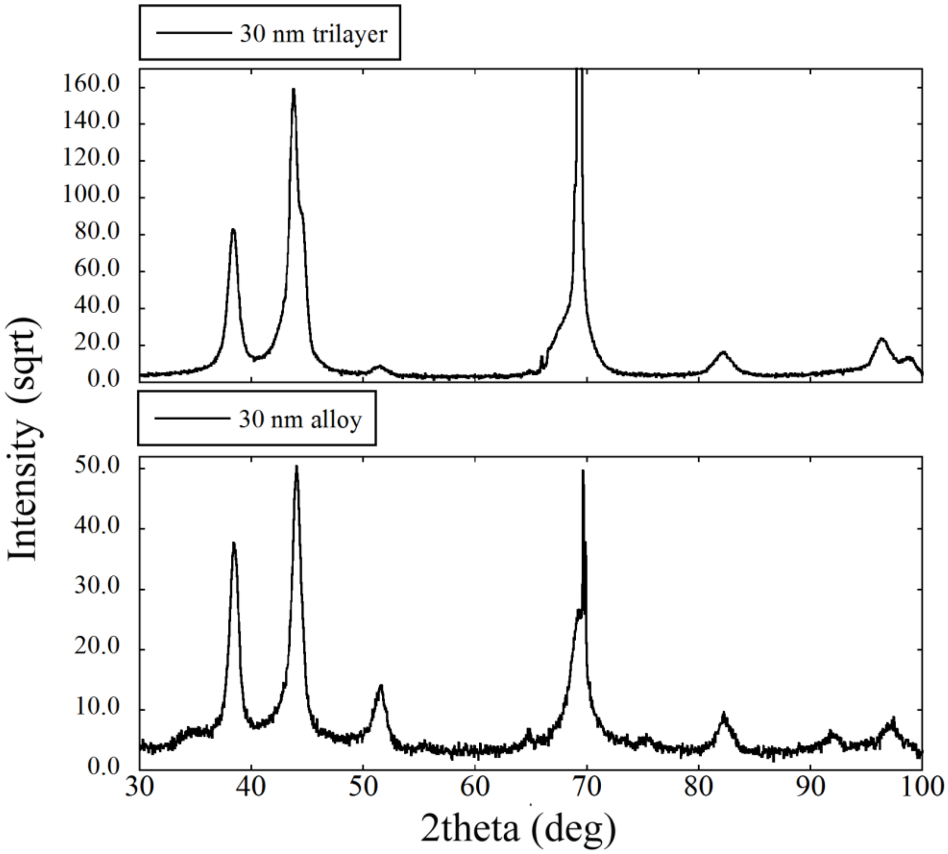

Figure 3-9. XRD measurement of films annealed at 500°C using the wafer curvature technique. Tri-layer films show an obvious change from the as deposited condition, where Cu and Ni peaks are no longer distinct but start to merge into one large peak around 43°.

As is immediately apparent from the 600°C anneal condition, the 5 nm alloy film shows a drastically different signature than those previously reported with the emergence of numerous peaks between 2theta 30°-50°, most likely due to formation of Ni_xNb_y intermetallics with Ni_3Nb being the most probable. The possibility of oxide formation is also highly likely, though an exact match for these peaks was not obtained. The 30 nm tri-layer film does not show any obvious new peaks; however, the majority of the Cu and Ni layers have alloyed with only a small amount left as a distinct layer.

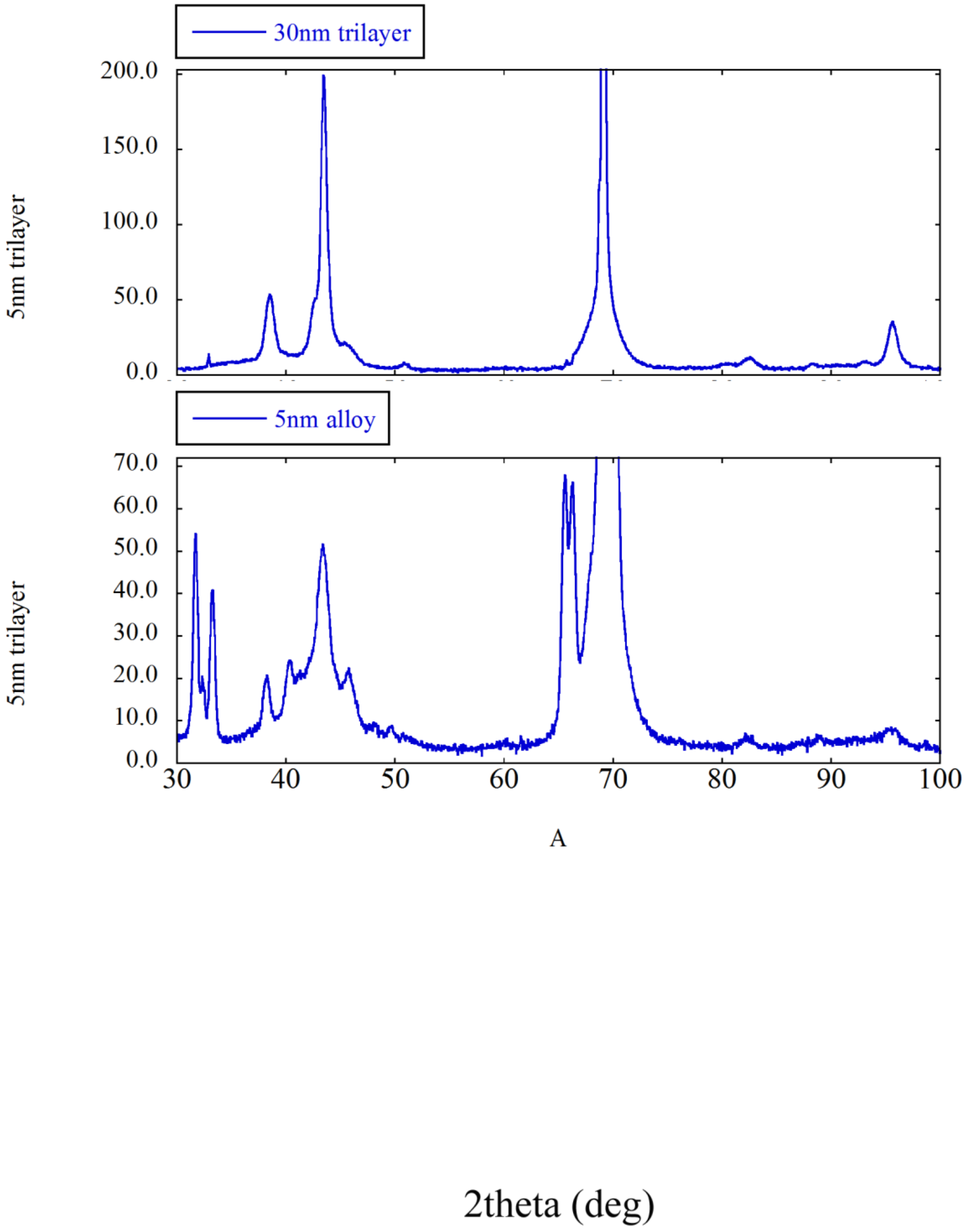

Figure 3-10. XRD scans of films which have undergone once cycle up to 600°C. The 5 nm tri-layer film developed so much residual stress in the film, it delaminated from the substrate and consequently XRD scans were impossible to perform.

CHAPTER 4 : Determining Extent of Alloying and Identifying Precipitates

Due to the small length scales that naturally govern nano-scale metallic multilayers, one of the most effective ways to investigate the individual layers and interface structure is using transmission electron microscopy (TEM). In this way, the microstructure of the individual layers can be determined including grain sizes, interface sharpness, crystal orientation, dislocation content, etc. Since the governing models used to predict the strength of these materials assumes the intrinsic strength is from the layer thickness as opposed to grain size, it is necessary to verify that the lateral grain dimensions are larger than the individual layer thickness. Otherwise, the deformation behavior would not follow the expected trend, leading to unexpectedly high strengths. The interface structure also plays a crucial role in NMMs and depending on its planarity and orientation relative to the neighboring layers, can have a profound effect on the strength properties and deformation behavior. Even incoherent interfaces can resist interface sliding if they are mechanically pinned due to sliding along rough interfaces. Therefore a thorough knowledge of the microstructure and interface structure of these NMM films is essential for a full understanding of the deformation and strengthening mechanisms.

Using this technique, the annealed microstructures of the 30 nm films were examined at two different annealing conditions: 300°C for 12 hrs and 500°C which was a result of one of the wafer curvature experiments. The majority of the TEM samples were prepared by FIB cut-out method creating thin lamellae samples which are then placed on a Cu grid to put into the TEM. Most of the samples were investigated using a JEOL 2200FS TEM/STEM operated at 200 keV. While the 30 nm alloy as-deposited condition was prepared using traditional cross-sectional preparation and examined using a Philips CM12 TEM operated at 120 keV.

4.1 As Deposited Microstructure

The as-deposited microstructure of each of the 30 nm films for the tri-layer sample is shown in Figure 4-1, using both bright field (top) and dark field (bottom) imaging techniques. Since these films were deposited using PVD magnetron sputtering, the Cu and Ni layers have the potential to deposit epitaxially given their similar crystallographic structures and close lattice parameters; however, re-nucleation is also possible. This particular sample shows evidence of both epitaxial (leading to a coherent interface) grains as well as re-nucleation (likely incoherent or semi-coherent interface). Examples of epitaxial grains are outlined in the figure with red boxes while examples of re-nucleated grains are outlined in blue, showing no significant preference to either epitaxial growth or re-nucleation. However, since this is only a small glimpse of the entire structure of the film a more extensive study would be required to determine the actual ratio of renucleated grains versus epitaxial growth.

The grains in the individual layers (though hard to determine in the Nb layers) have diameters similar to or greater than the layer thickness, indicating the intrinsic size in these layers is actually the layer thickness as opposed to the grain size. This is important when considering the governing strengthening mechanisms, since confined layer slip (CLS) would only be dominant when the grain diameter is larger than the layer thickness which will allow the single dislocations to bow along the interface. As can be expected, both the Nb/Ni and Nb/Cu interfaces are incoherent and grew via re-nucleation. The layers in this film also show substantial waviness and roughness. This is particularly noticeable in the bright field image where the Nb and Cu interface isn’t sharp as shadows of different parts of the grain are visible though they are not visible in the STEM image. Based on the STEM dark field image, the layer thicknesses of Cu, Ni, and Nb were measured to be 30, 30, and 30 nm respectively.

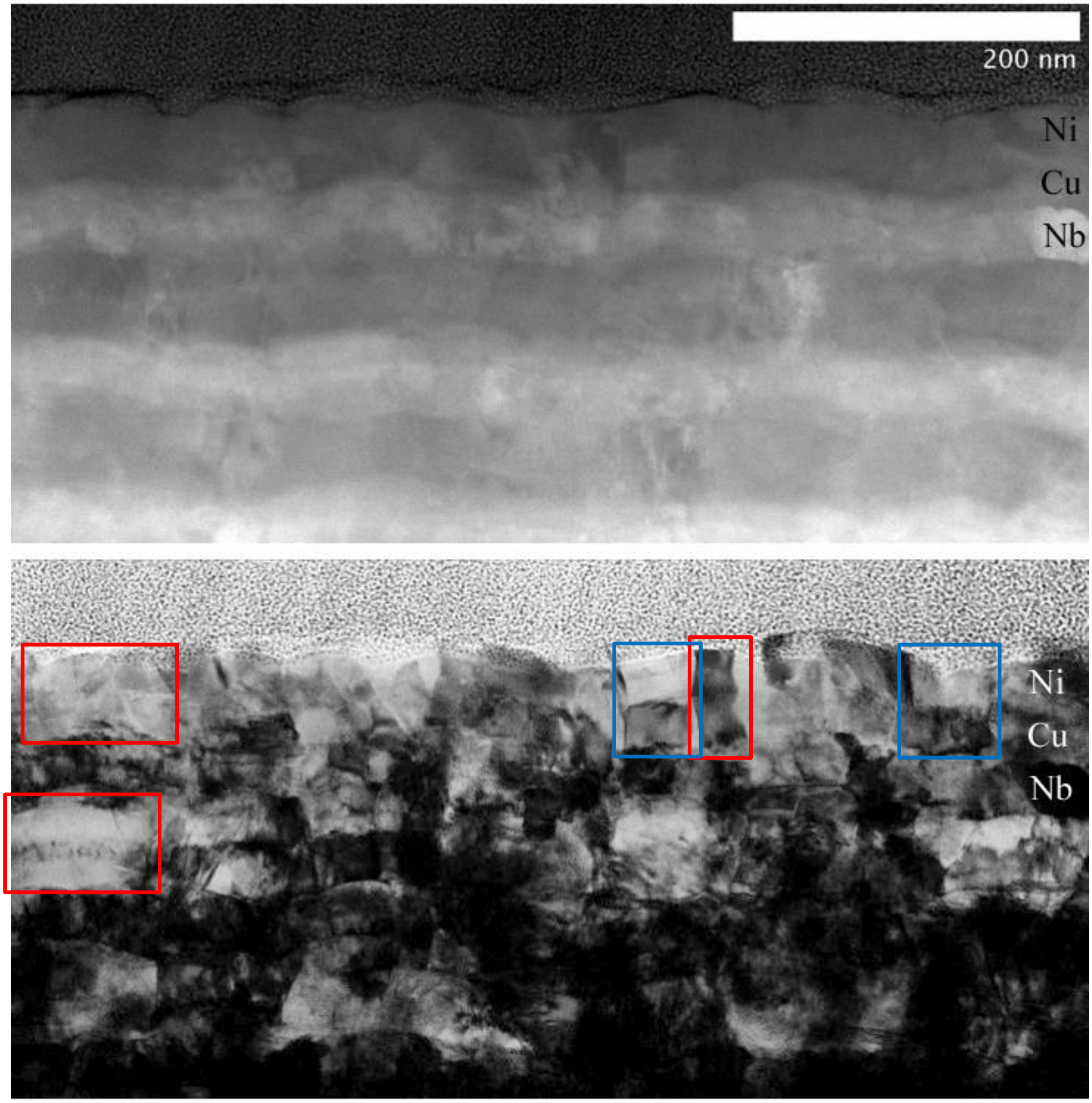

Figure 4-1. Cu/Ni/Nb tri-layer as-deposited microstructure observed with bright field (top) and dark field (bottom) STEM imaging. The Cu/Ni interface shows some areas which appear to be coherent (outlined in red), while there are also other places which do not seem to be coherent (outlined in blue).

The as-deposited bright field image of the 30 nm alloy film is shown in Figure 4-2, which includes labels of the individual layers. The first noticeable difference in these films is the presence of a large number of growth twins in the CuNi alloy layer which have nanometer scale spacing and would result in much higher strengths than what is predicted from the CLS model. Additionally, the majority of the CuNi grains show columnar growth with grain diameters smaller than the layer thickness. This would lead to deformation mechanisms in the CuNi alloy layer which do not follow the CLS model, but rather that of a nanocrystalline material. Once again, as is expected, the CuNi and Nb films grow via renucleation due to the out of plane preferential growth of (110) for Nb and (111) for the CuNi alloy (as was seen in the XRD scans of the as-deposited films in Section 3.1).

Similar to the tri-layer films, the layers are slightly wavy and have a mix between columnar and equiaxial growth patterns leading to rough interfaces which can actually aid in the stability of the multilayers due to mechanical constraints, lessening the layers' ability to slide freely and thus increasing the film toughness. Ledge and step imperfections in the layers could also lead to an increase in the yield strength of the film due to the additional barrier to slip transmission as was modeled in Cu/Nb multilayer films [71]. While the study did not look into the effect on interfacial sliding, it does suggest that interfacial imperfections lead to a certain amount of strengthening as well as areas of stress concentration, which allows for easier dislocation nucleation in the Nb layer leading to reduced strength. Due to these competing mechanisms, the extent of strengthening versus weakening of the multilayer system as a whole is difficult to predict if strictly considering dislocation transmission and nucleation. A more extensive study in the effect of surface roughness on the toughness of these multilayer films is desirable.

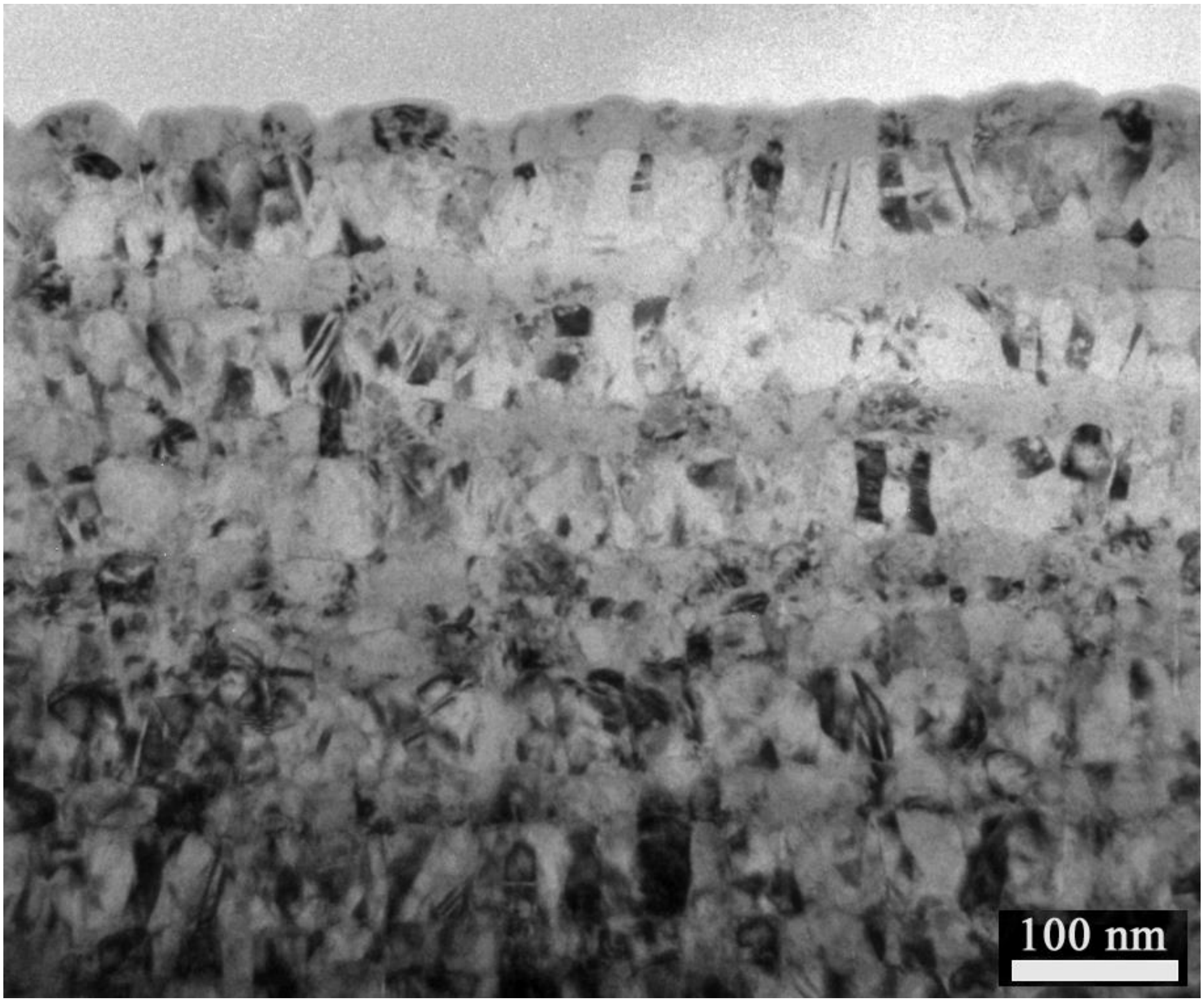

Figure 4-2. Bright field TEM image of 30 nm Cu-Ni/Nb alloy as-deposited microstructure. Cu-Ni alloy layer has a large density of twins with grain sizes equal to or smaller than the individual layer thickness, which would lead to higher strengths than those suggested by the CLS model.

4.2 300°C 12 hr Annealing Condition

After both 30 nm films were annealed at 300°C for 12 hours, lamella for TEM investigations were made using a Tesca Lyra Focused Ion Beam (FIB) lift-out technique. The 12 hour annealing condition was chosen over the one hour and three hour conditions because it allows ample time for all temperature induced changes to occur in the films. Since the majority of the changes in the microstructure will be due to diffusion of the different elements causing new alloy/intermetallic formation, and temperature is the strongest influence on the diffusion rate, microstructures of the films at the same temperature should be very similar while films annealed at different temperatures could be much different. Additionally, since both films were annealed in the same vacuum chamber, the annealing conditions are identical and any difference in the microstructure is strictly due to the differences between having a CuNi alloy instead of discrete Cu and Ni layers.

4.2.1 30 nm Tri-layer

The high resolution bright field and dark field STEM images of the 30 nm tri-layer sample annealed at 300°C for 12 hours is shown in Figure 4-3. An obvious change at the interface is observed which is likely due to the formation of a very small layer of Nb_xNi_y intermetallic; however, could also be due to diffraction fringes from a rough interface or increased dislocation content. Interestingly, this is observed at both the Nb_xNi_y interface as well as the Nb/Cu interface which suggests that the Ni is diffusion through the Cu layer to react with Nb at the Cu/Nb interface. While this is not necessarily surprising, the Cu an Ni layers are still mostly chemically distinct as could be seen in other TEM sections as well from the XRD scans reported previously. Therefore, the Cu and Ni layers do not fully alloy but Ni can fully diffuse across the Cu layer to react with Nb and create a very thin Nb_xNi_y intermetallic layer.

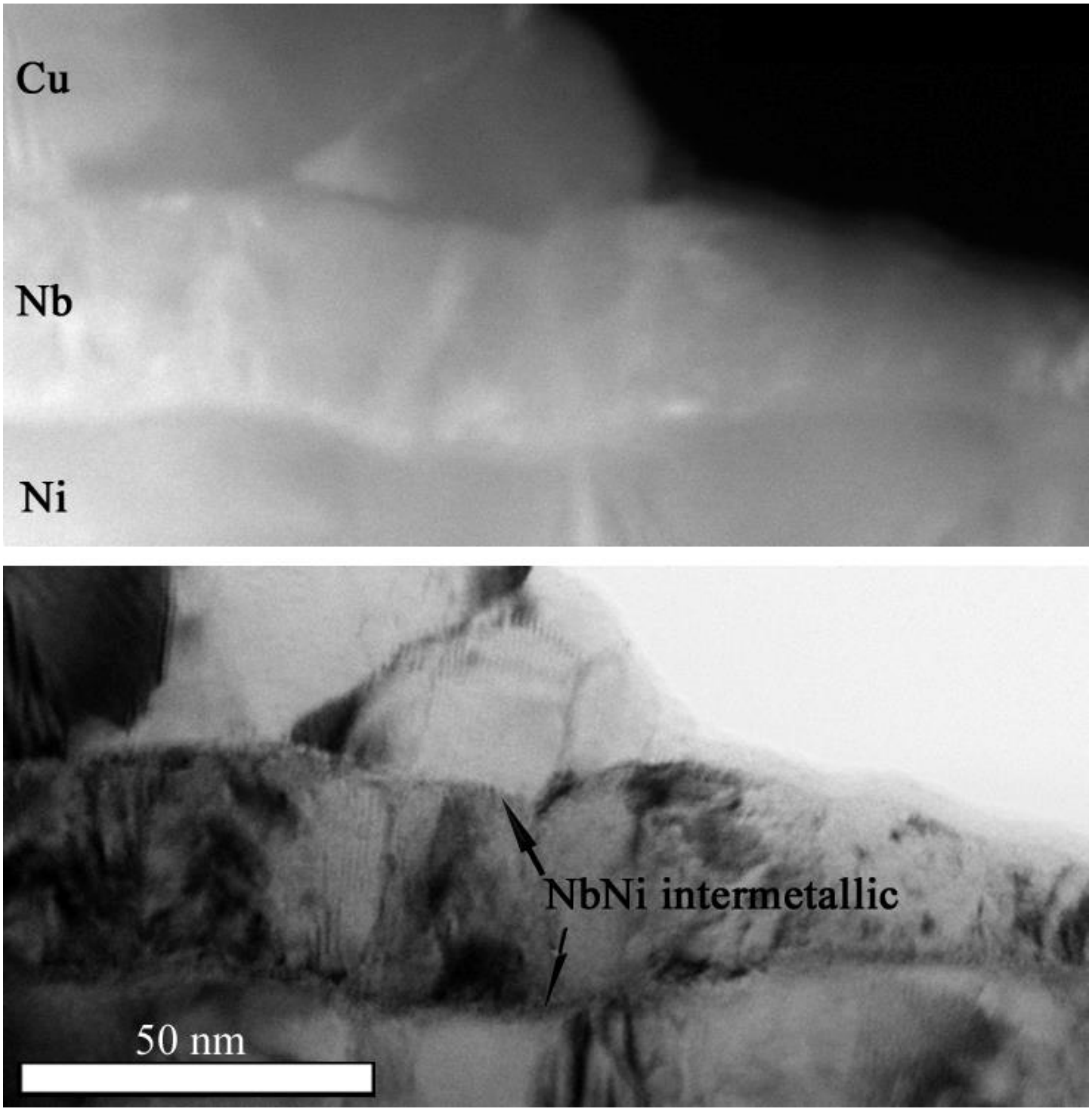

Figure 4-3. Bright field (top) and dark field (bottom) TEM images of 30 nm tri-layer film annealed at 300°C for 12 hrs. The presence of a 2-3 nm thick NbNi intermetallic layer is observed on both sides of the Nb layer.

4.2.2 30 nm Alloy

The 30 nm alloy 300°C condition was prepared for TEM observation in a similar manner as the other samples but was lost during transportation before any images could be recorded. Future work will include making a new sample to examine and compare to the 30 nm tri-layer annealed under the same conditions. Until then, it is assumed that the microstructure will follow a similar pattern as the other samples, with Nb_xNi_y layers on either side of the Nb layer which is brought about by the increased diffusion at the elevated temperatures. This intermetallic formation is also observed in the 500°C annealed condition which will be discussed in the following section. The thickness of the intermetallic formation between the alloy and tri-layer samples will be interesting to compare, whether the alloy allows for greater Nb_xNi_y formation due to the larger concentration of available Ni at the interface, or if enough Ni is readily diffused through the Cu to make it approximately the same reaction rate.

4.3 500°C Wafer Curvature Annealing Condition

As will be discussed in the next chapter, an additional increase in hardness of these films is seen when they are annealed up to a temperature of 500°C using the wafer curvature technique, which only used a 10 second hold at 500°C but had the same heating and cooling rate as those annealed in the vacuum furnace. While there might still be some additional microstructural changes that could occur with a longer hold at the peak temperature, since temperature is the controlling factor in diffusion, the majority of the change has likely already occurred.

4.3.1 30 nm Tri-layer

Figure 4-4 shows the dark field image of the 30 nm tri-layer film heated to 500°C, with an much thicker layer (when compared to the 300°C 12 hr condition) on either side of the Nb layer. Additionally, the majority of the Cu/Ni interfaces are no longer visible, either suggesting the disappearance of the interface by full alloying, or at very least a substantial diffusion gradient is expected, especially given the increased CuNi alloy peak seen in the XRD results. Nevertheless, the possibility that this section of the film is predominantly epitaxial growth cannot be ruled out. Going with the assumption that the Cu/Ni interface has disappeared as a result of CuNi alloy formation, the structure of the film is now much more columnar and would not have the added benefit of the coherent interface. Additionally, the grain size of these new "alloy" grains is now less than the layer thickness of the samples which makes the CLS deformation less likely to accurately describe the strengthening mechanism. While this won't be the largest controlling factor of determining the change in strength as a result of annealing, it should be considered to have some effect on the hardness of these annealed films.

While the Nb_xNi_y layer is once again seen on both sides of the Nb layer, the relative thicknesses of each is difficult to determine from this scan; however, the thicknesses look to be approximately the same regardless of the original interface. Therefore, enough Ni is able to diffuse through the Cu layer to not be the rate limiting factor of this Nb_xNi_y formation. Since the intermetallic layer in the 300°C annealed sample was not thick enough to verify for sure whether or not it was due to a new layer forming or was the result of diffraction from other means, the presence of this thicker layer suggests that it actually was the very beginnings of Nb_xNi_y growth. EDS scans of the different annealed conditions will further support this theory and will be discussed in the next section.

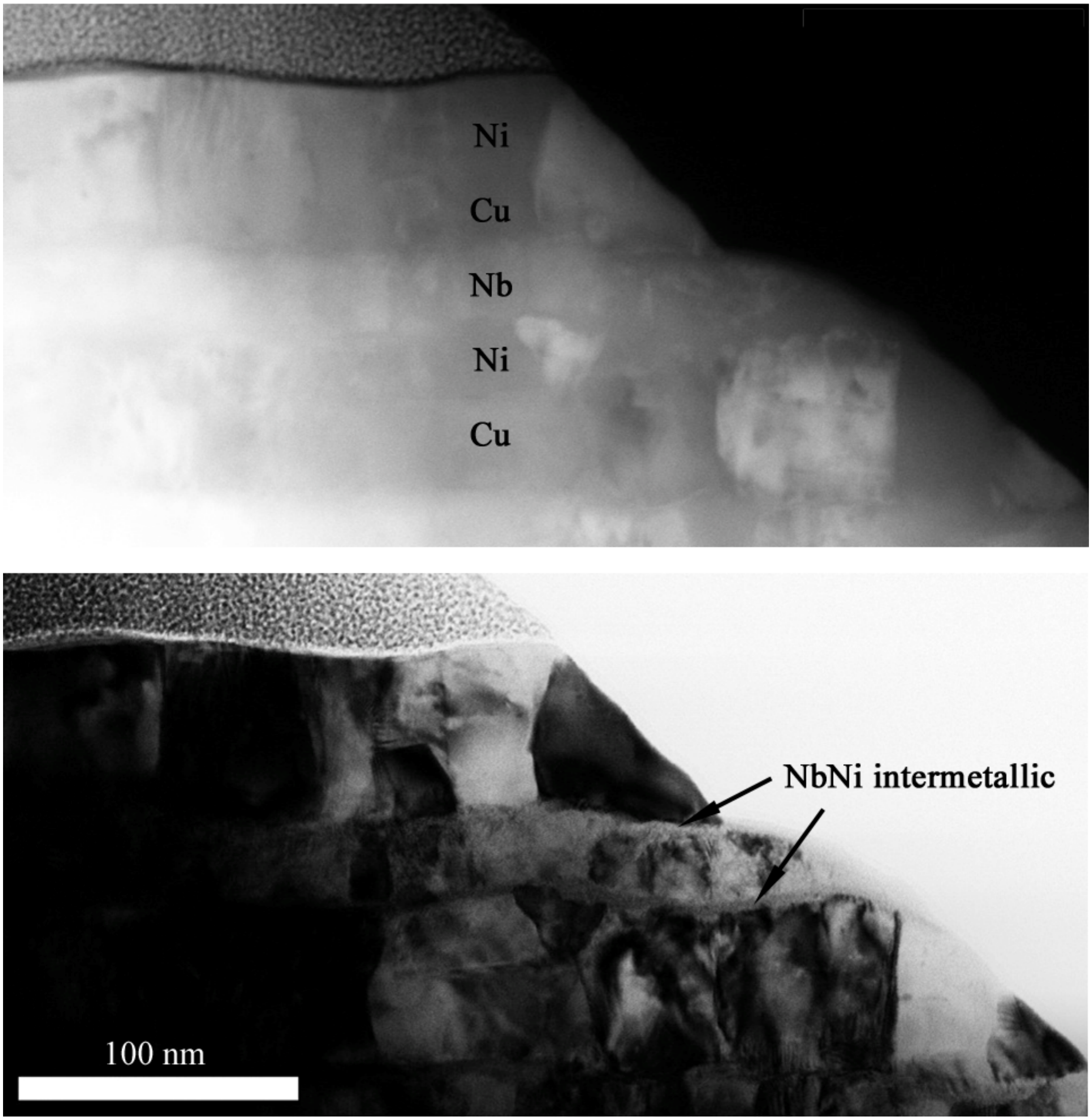

Figure 4-4. Bright field (top) and dark field STEM (bottom) of the 30 nm tri-layer film annealed using the wafer curvature method to 500°C. A new layer is clearly seen on both sides of the Nb interface indicating Ni is diffusing through the Cu layer as well as reacting at the Nb/Ni interface.

4.3.2 30 nm Alloy

The 30 nm alloy film which also underwent the temperature cycle up to 500°C during the wafer curvature investigations is shown in Figure 4-5, once again with obvious Nb_xNi_y formation on both sides of the Nb layer. In this image, it is quite apparent that both layers are of approximately the same thickness, although since the transition between the intermetallic to Nb and CuNi layers is not a sharp interface, the exact thickness is hard to determine. Measuring 10 different places along this scan suggests that range in thicknesses of this Nb_xNi_y ranges from 7-12 nm. This also results in thinner Nb and CuNi layers which would lead to increased hardness and will be discussed more in Chapter 5.

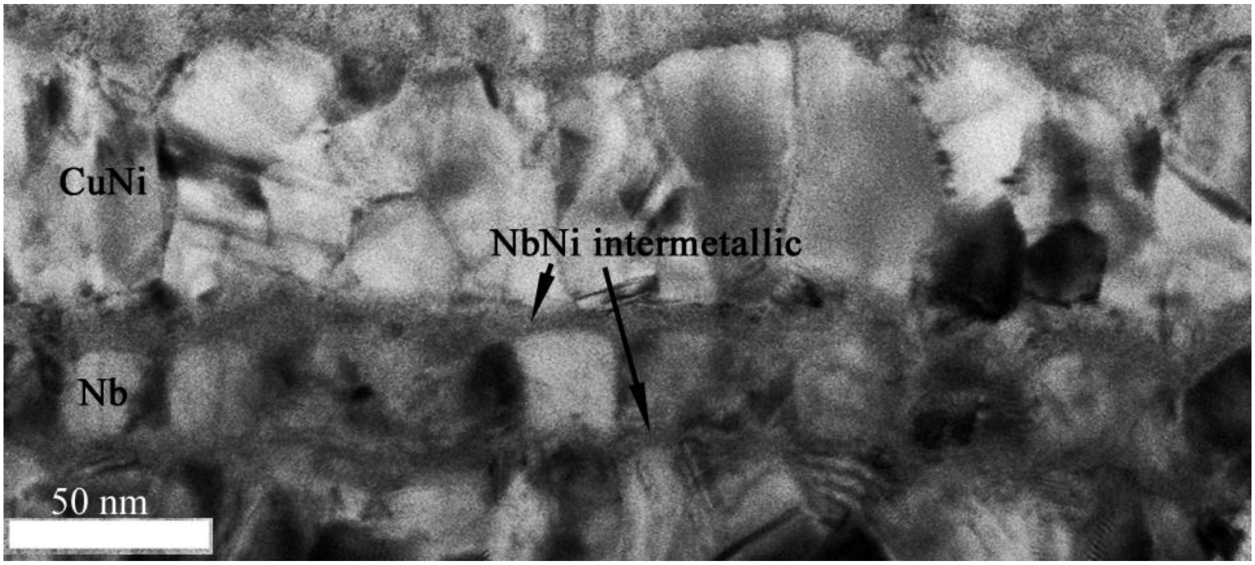

Figure 4-5. STEM dark field image of 30 nm alloy film annealed at 500°C during the wafer curvature experiment. The Nb_xNi_y layer which forms on either side of the Nb is of equal thickness, approximately 7-12 nm thick.

Surprisingly, the CuNi grains show a similar structure as was seen in the as-deposited films with significant twinning and grain sizes smaller than the layer thickness and a mixture of equiaxial and columnar growth. While grain growth is generally expected during annealing, there does not seem to be any evidence of significant grain growth in these films, either stabilized by the fact that they are solid solution alloys or confined from significant growth by the Nb and intermetallic layers. In any case, any softening which would have resulted from an increase in grain size in these layers will not be observed.

4.4 Energy-dispersive X-ray Spectroscopy

Annealed films were examined using Energy-dispersive X-ray Spectroscopy (EDS) to determine the relative concentration of an element across the interfaces. This method is crucial in determining potential alloying and in verifying intermetallic formation as a result of the annealing conditions applied during this study. The lines scans were conducted at 200keV and a resolution of 2 nm, across both the Cu/Nb interface as well as the Nb/Ni interface for the three annealing conditions previously discussed. Since the FIB lamellae are attached to Cu grids for transportation and ease of handling, there is a low Cu signal as the background in all of the scans which should not be misconstrued as being a signal from Cu diffusing into the different layers as a result of annealing. Most importantly, the slopes of the intensity profiles will be able to give us some idea of the alloying which is occurring in the films. The sharper the change from one element to another, the less alloying/intermetallic formation is occurring. However, due to the apparent roughness of the interface and the thickness of the cross-section, the precise amount of alloying is difficult to quantify. Therefore, this method is used as a qualitative measure to determine the extent annealing affects the microstructure of these two different multilayer systems.

4.4.1 30 nm Tri-layer

The 30 nm tri-layer film annealed at 300°C for 12hr was examined using EDS across all three layers with the resulting STEM image and elemental intensities along the line scan shown in Figure 4-6. The line scan begins and ends in the Nb layer with different intensity levels for the two Nb layers due to the different thicknesses of the layers from FIB polishing. This is also the reason all of the layers show an increasing intensity as the scan travels from the top to the bottom of the section. As was mentioned previously, there is a baseline Cu signal from the Cu grid that should not be contributed to alloying and is in fact present at all times. Since Cu and Nb are completely immiscible under normal conditions, if Cu were present in the Ni layer via alloying, there would be a larger relative Cu intensity in the Ni layer when compared to the Nb layer. This is not the case in this annealed sample. The same Cu baseline is present in both Nb and Ni indicating little, if any, alloying of the Cu and Ni layers. Interestingly, the regions surrounding the interfaces are still relatively sharp specifically the Cu-Ni interface. Since these two materials are completely miscible at all temperatures and have similar crystal structures and lattice parameters, one would have predicted a significant amount of alloying was likely to occur as a result of annealing at 300°C for 12 hours. However, as the EDS and XRD results have proved, these layers remain stable at this annealing condition. The Nb-Ni interface shows a bit more of a slope in both elemental peaks; however, not to the extent that immediately points to intermetallic formation.

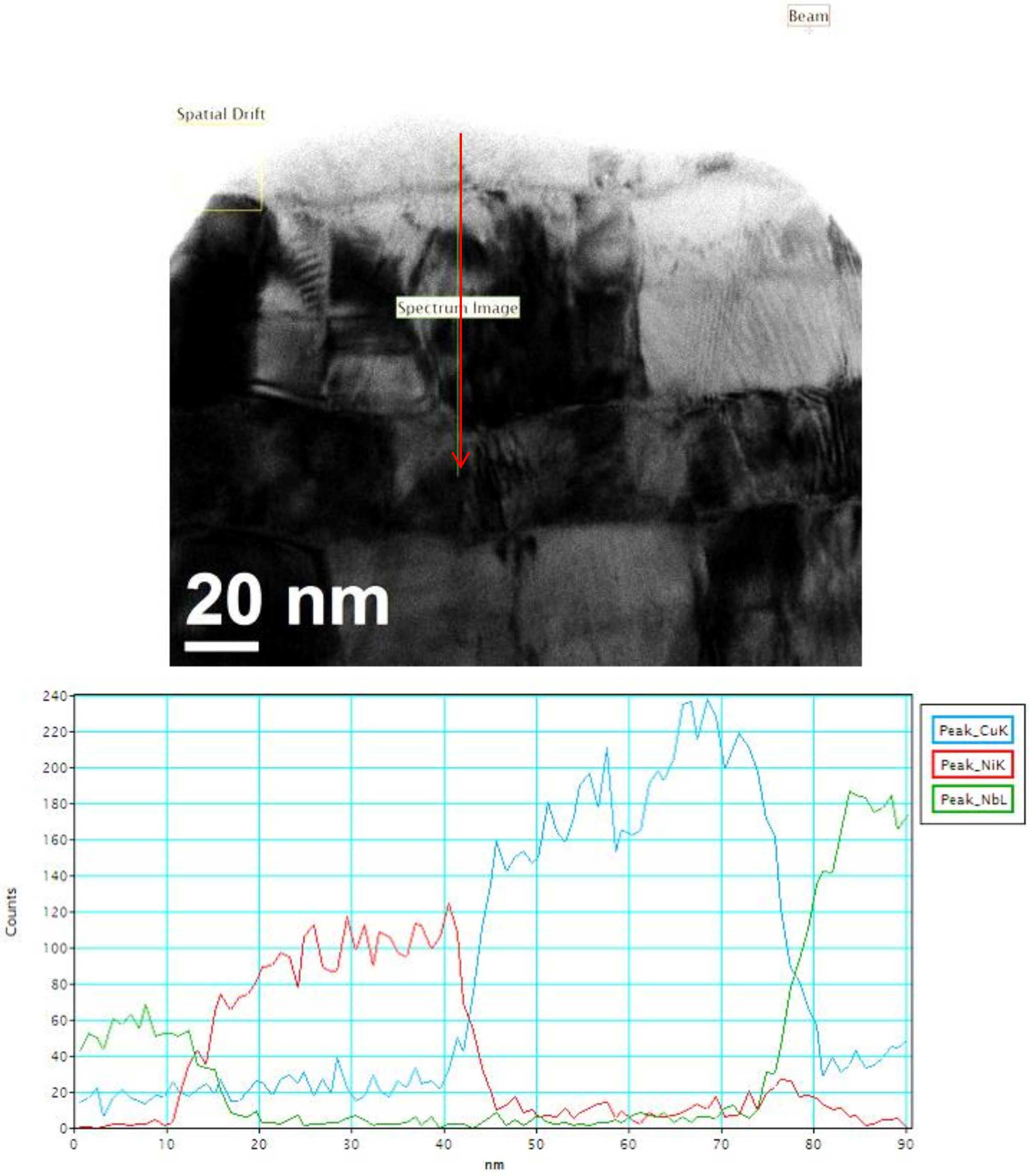

Figure 4-6. EDS line scan (bottom) of tri-layer film annealed at 300°C for 12 hours with the accompaning STEM image (top) showing gradual slopes on either side of the Nb layer for all three elements which is likely due to changing film thickness as a result of FIB polishing.

Most interestingly, the Cu-Nb interface show both a gradual slope in the Cu and Nb elemental intensities (most likely due to the roughness of the interface) as well as a slight increase in the Ni peak right at the interface. While the former is not necessarily surprising, the increased Ni peak is quite unexpected considering the apparent lack of Ni *in* the Cu and Nb layers. A closer examination of the Cu-Nb interface is shown in Figure 4-7, including the STEM dark field image with the accompanying EDS line scan starting in the Cu layer and ending in the Nb layer. These scans were also run at 200kV and at a resolution of 0.5 nm. As was seen in the larger scan which spanned across both interfaces, the Ni intensity increases significantly across this interface, reaching almost the same intensity as the Nb layer. This strongly suggests the presence of a Nb_xNi_y intermetallic which has started to form as a result of annealing. Given the relative intensities right at the interface, the most likely intermetallic is Nb_6Ni_7, although the possibility of Nb_3Ni is also highly likely, especially as the Ni concentration decreases further from the interface. However, the exact nature of the new layer is difficult to determine using XRD since the intermetallic layer thickness is only on the order of a few nanometers, too small for the resolution of the XRD source used. In order for the Ni to reach the Cu-Nb interface, the Ni atoms must diffuse through either the Cu or Nb layer to the interface. Since Ni easily diffuses into Cu it is very probable that the Ni is able to diffuse completely through the Cu layer to react with Nb. Additionally, since the Nb and Ni would immediately react to form intermetallics before allowing the Ni to fully diffuse across the layers, it is most likely the Ni diffusing through the Cu layer but preferentially forming the Ni_xNb_y intermetallic rather than staying in solid solution.

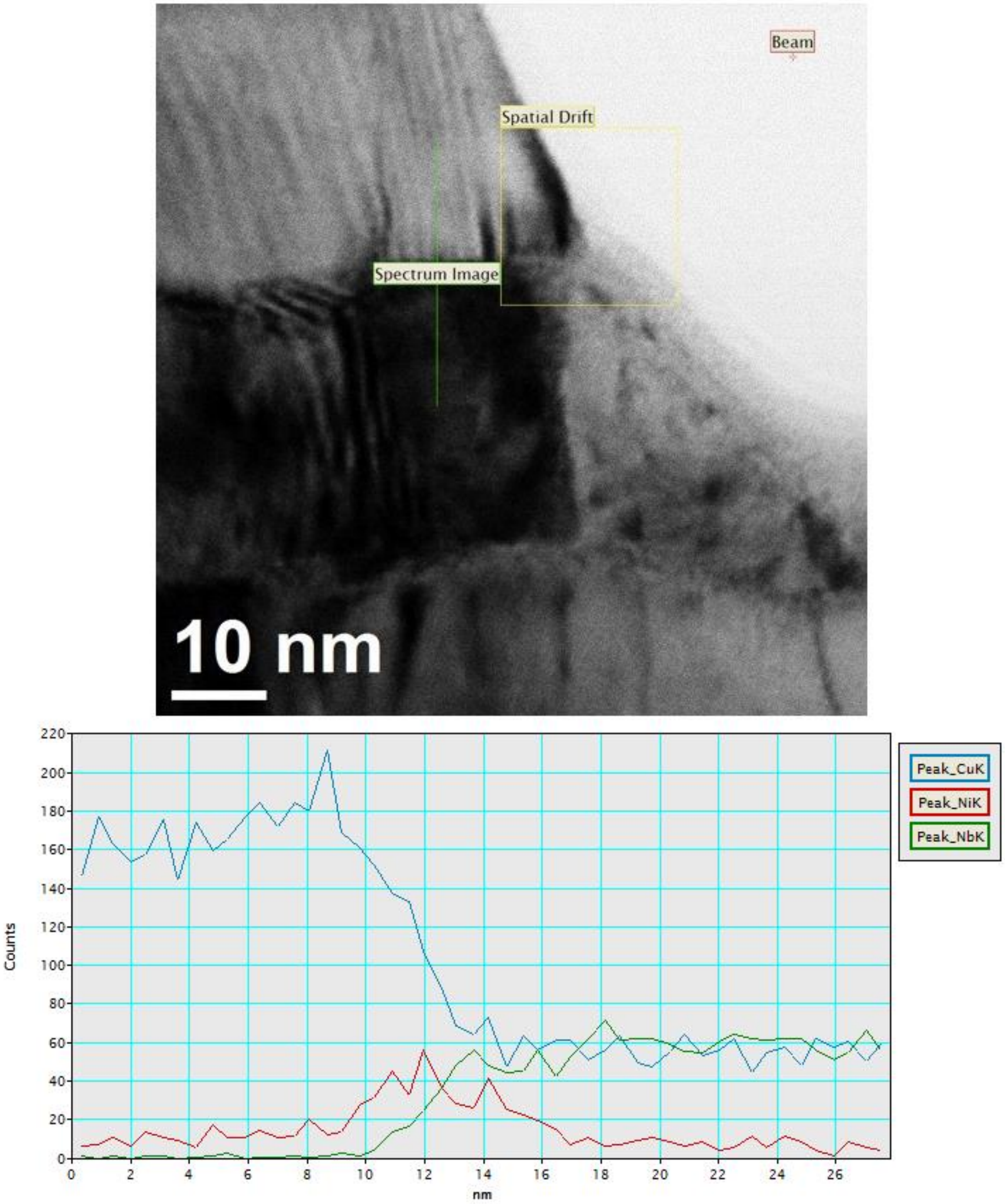

Figure 4-7. Higher resolution EDS scan (bottom) with complementary STEM image (top) showing scan line of the tri-layer sample annealed at 300°C for 12 hours. This particular scan focuses on the Cu-Nb interface, showing an obvious Ni enrichment at the interface indicating Ni is diffusing through the Cu layer to interact with Nb.

A close up examination of the Nb-Ni interface shows a more detailed look at the diffusion of Ni into the Nb interface. Figure 4-8 once again includes the STEM image which correlates to the EDS line scan shown in the bottom of the figure. As was seen in Figure 4-6, the Ni signal gradually increases as the thickness of the cross-section increases, which can mask the actual amount of Ni which diffuses into the Nb layer. However, this depends how drastically the thickness increases along the 20 nm line scan. The Nb signal also shows a very shallow slope from the peak intensity which is stable across the layer to no signal, spanning approximately 4 nm. The gradual slope could be caused from: increasing thickness of the sample, roughness of the layer, or diffusion of the elements and intermetallic formation. As the layer thickness increases the volume of material being sampled increases, thereby increasing the relative amount of Nb, even if the interface is perpendicular to the beam. Alternatively, if the interface is not sharp or is not perpendicular to the incident beam, the EDS scan will also show sloped signals for the two different layers. Lastly, if the sample thickness does not change significantly along the line scan and the interface is both sharp and perpendicular then the slopes are actually due to diffusion of the elements and likely the formation of an intermetallic. Since the portion of the line scan surrounding the interface which shows sloping elemental signals is only about 4 nm in length, the likelihood of the thickness of the film changing significantly across this small distance is small, the first option is least likely. The roughness of the interface however could change enough across the 4 nm to cause the sloping seen in the line scans. Therefore, while the sloping EDS signal is not irrefutable proof that a Nb_xNi_y intermetallic actually exists at this interface, there is also no proof that the intermetallic doesn’t exist.

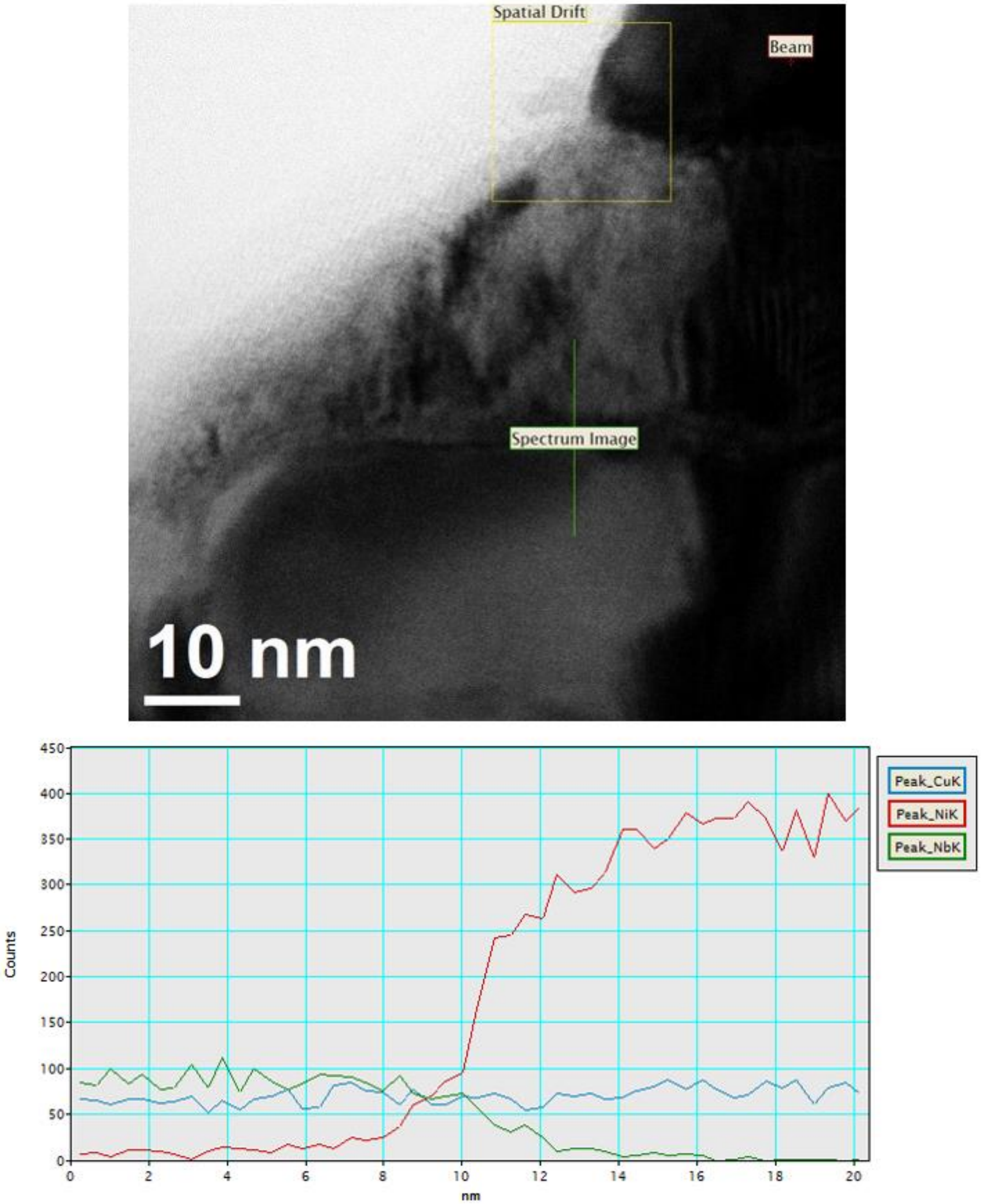

Figure 4-8. Higher resolution EDS scan (bottom) with complementary STEM image (top) showing scan line of the tri-layer sample annealed at 300°C for 12 hours. This particular scan focuses on the Ni-Nb interface, showing a gradient in the Nb and Ni layers approximately 6 nm wide.

One way to determine if the signal is more due to interface roughness or diffusion would be to scan additional sections on the sample and see if the same slope is seen in other parts of the film. Since the roughness and alignment of the interface will be different in different parts of the film, if the sloping in the intensities remains the same, it is likely due to intermetallic formation rather than merely interface roughness. Additionally, EDS line scans of the as-deposited condition will be able to tell us if this sloping interface occurs regardless of the annealing condition. These tests will be the focus of future investigations.

The difference between the two different annealing temperatures on the 30 nm tri-layer film can be seen from Figure 4-9 which shows the film after being annealed at 500°C. The EDS line scan across both interfaces shows a similar trend as the 300°C 12 hr annealing condition with the exception of significantly more Ni presence in the Cu layer. Additionally, there is a substantial presence of both Cu and Nb in the Ni layer. This could possibly suggest a complex tertiary alloy of unknown composition, or a mixture of CuNi and Nb_xNi_y alloys, though exactly which combination it is would be very difficult to determine using the EDS technique. Focusing on the Cu layer, it is obvious the amount of Ni present in the layer is substantially more than was observed in the 300°C 12 hr condition. The ratio of Cu:Ni in the Cu layer ranges from 5.5:1 to 3.3:1 as the scan moves closer to the Nb interface, with the intensity of the Ni increasing while the Cu intensity decreases slightly. Once again, the Ni intensity increases right at the Cu/Nb interface with twice the number of counts at the interface as is seen in the middle of the layer. Finally, the Ni layer once again shows a gradual Nb content decreasing from the Nb-Ni interface, indicating a substantial amount of diffusion is occurring. Since the Nb layer count is level along the entire thickness, it is safe to assume the concentration gradient is not a result of changing cross-sectional thickness but is actually representative of a diffusion gradient.

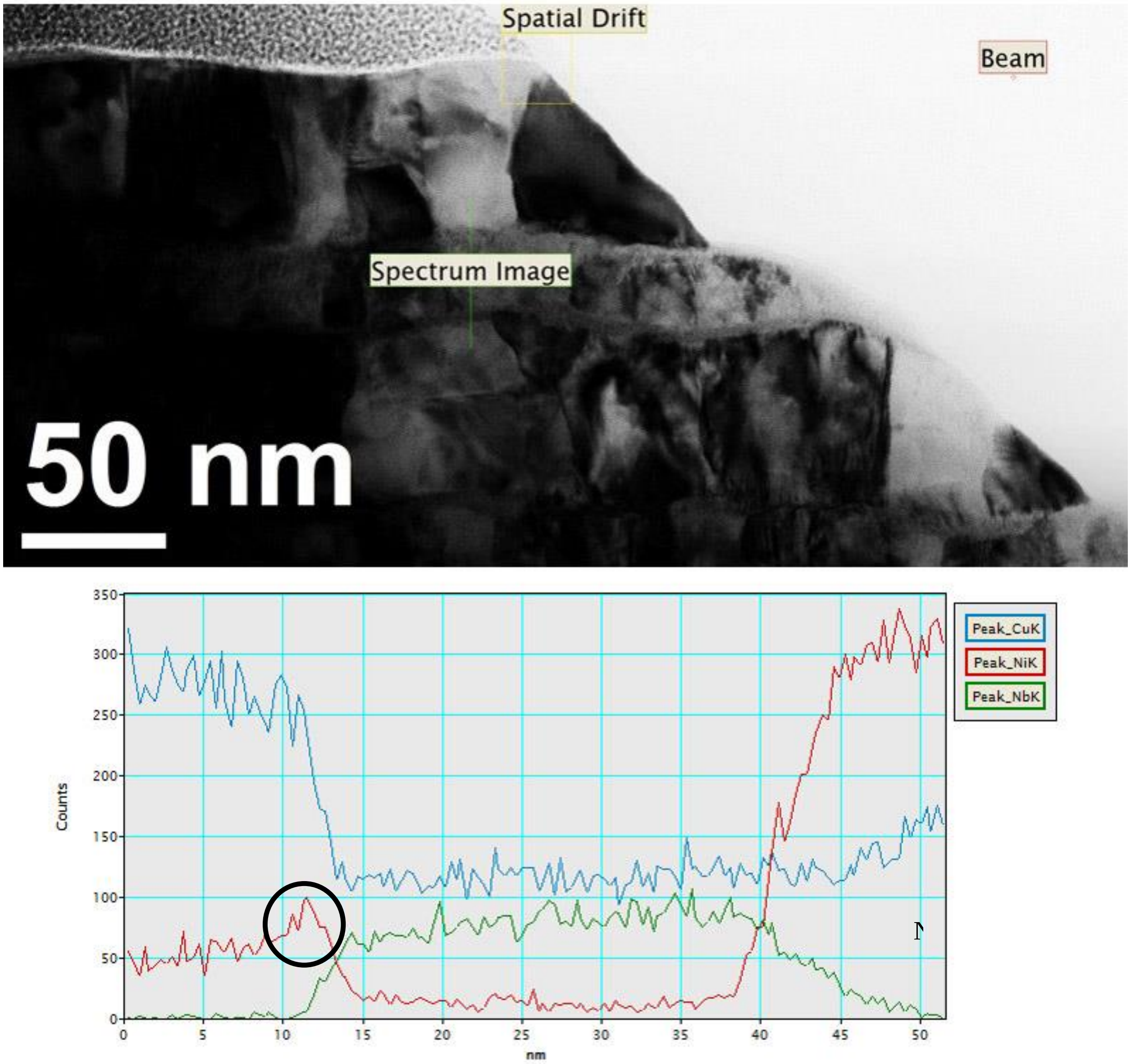

Figure 4-9. EDS line scan (bottom) of tri-layer film annealed at 500°C during the wafer curvature experiment with the accompaning STEM image (top) showing gradual slopes of the various element indicating substantial diffusion in the sample, creating CuNi and Nb_xNi_y alloys.

4.4.2 30 nm Alloy

The 30 nm alloy sample annealed at 300°C was damaged during sample preparation and there is no way to compare the alloy and tri-layer systems for this temperature; however, the 500°C annealed conditions can be compared. Figure 4-10 shows the TEM image and accompanying EDS line scan for the 30 nm alloy film annealed to 500°C. Since the FCC layer in this film started as a CuNi alloy, the apparently equal amounts of Cu and Ni intensities (when negating the extra signal from the Cu TEM grid) is expected. However, right at the interface between the CuNi layer and the Nb layer, there is an oversaturation of Ni which exceeds the Cu signal despite the extra signal from the TEM grid, indicating there is additional Ni at the interface, which was also seen in the tri-layer films. This leads to additional Ni depletion in the CuNi alloy which is slightly visible in the CuNi alloy signal, the Ni element slowly decreasing while the Cu element increases at the same time. The Cu signal increasing can easily be due to slight changes in the thickness of the cross-section from polishing; however, the Ni signal would have to increase at the same rate, which it does not. There are also significant sloping of the signals near the interfaces, with Cu and Ni sloping at approximately the same rate which suggests some of the gradient is strictly due to interface roughness as opposed to purely diffusion. However, if the TEM grid signal is subtracted from the Cu, the portion of the Cu in the Nb layer is much lower than the Ni signal. This is also apparent when comparing the length of the segment which is flat, indicating no Cu atoms present except those excited from the TEM grid; the Cu segment spans approximately 35 nm whereas the Ni segment is only 15 nm. Additionally, the Nb slope spans about 15 nm on either side of the peak from the Nb layer, indicating substantial diffusion into the alloy layer.

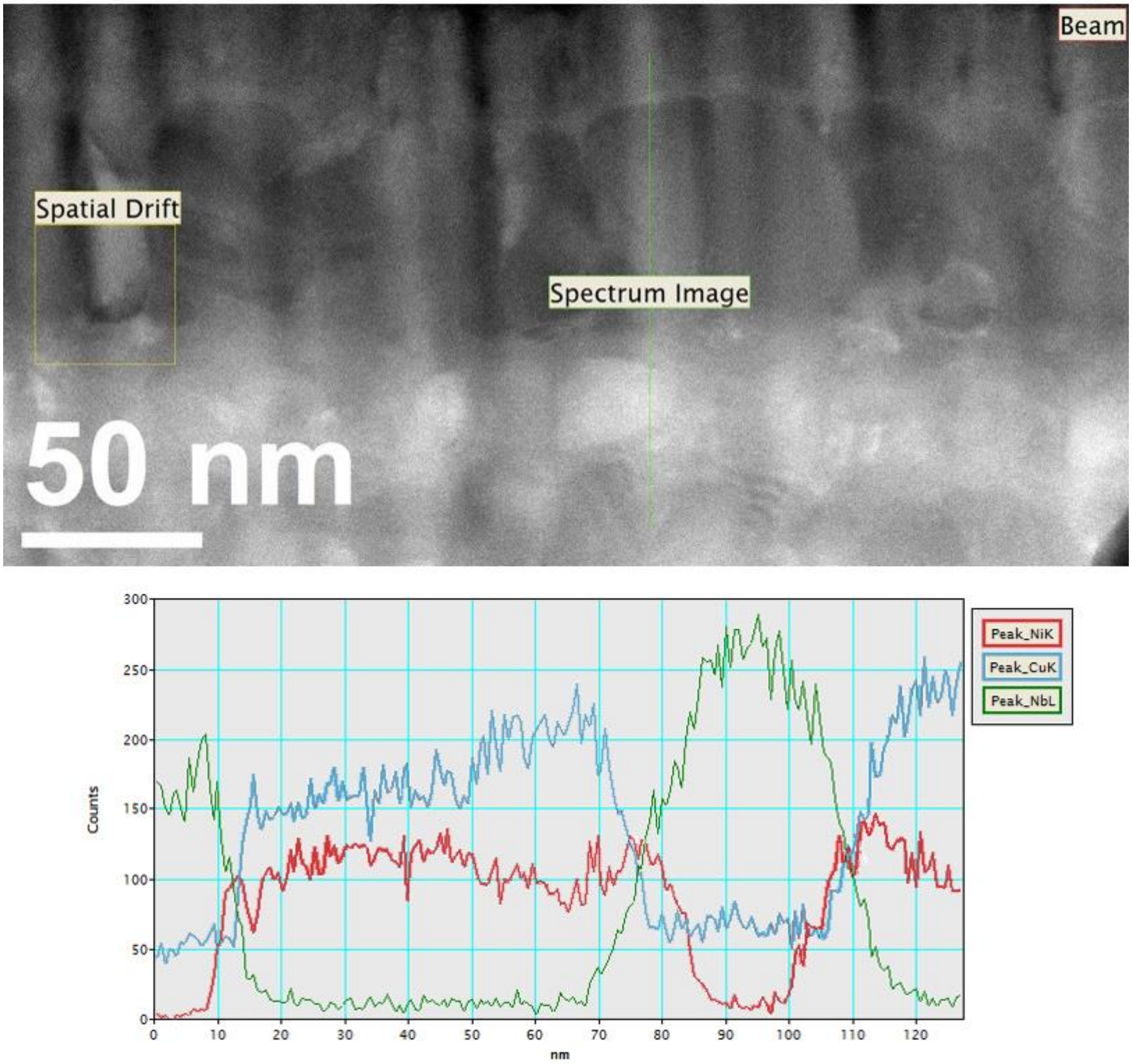

Figure 4-10. EDS scan of 30 nm alloy film annealed up to 500°C during the wafer curvature experiment. In this case, the Cu (blue) and Ni (red) are in solid solution and Nb (green) is its own distinct layer. Notice the enhanced Ni signal at the interface, despite the additional background Cu signal from the TEM grid.

The tri-layer sample shows a similar slope at the Ni interface, however only spans approximately 10 nm and only about 4 nm at the Cu-Nb interface which is due to the intermetallic formation or interface roughness as opposed to diffusion into the Cu layer. Therefore, a greater amount of Nb has diffused into the neighboring layers in the alloy film than in the tri-layer film, which is reflected in the nanoindentation data as will be discussed in the following chapter.

A higher magnification image of this film is shown in Figure 4-11, which focuses more closely on a single interface. As was seen in the previous figure, but is shown more obviously here, the Ni signal exceeds that of the Cu signal right at the interface, especially if the Cu grid background is subtracted from the Cu signal. Additionally, the 12 nm slope of the Nb signal is much more apparent at this scale than in the previous image while the Ni signal also has a slope spanning about 5 nm. The Cu signal also has a small slope spanning about 2-3 nm which could be strictly due to the roughness of the interface. In any case, the amount of diffusion of the Ni and Nb atoms exceeds that of the roughness of the interface reducing the layer thickness to less than the original as-deposited condition, which should lead to strengthening of the film. Furthermore, the addition of an intermetallic layer, which is stronger than the pure elements, will add to the strength of the overall composite beyond that of a reduction in layer thickness. All of which will be discussed in the next chapter.

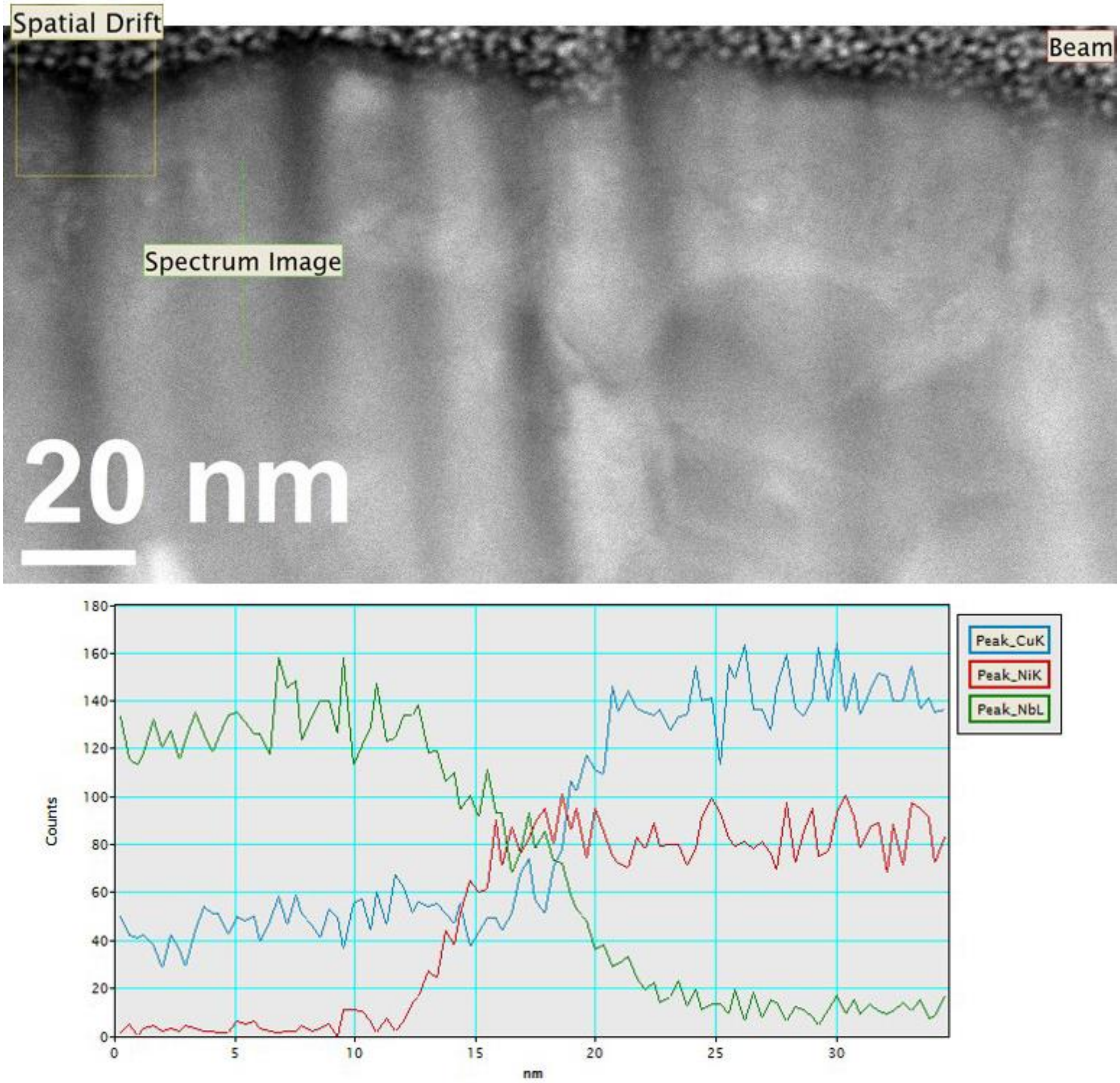

Figure 4-11. Higher resolution of EDS scan specifically across the Nb-Ni interface showing a distinct region of Nb_xNi_y alloy with varying concentration (between 12 and 22 nm along the scan line). The intensity of the Ni signal exceeds that of the Cu close to the interface, especially when the Cu signal from the TEM grid is taken out of consideration.

CHAPTER 5 : Nanoindentation for Determining the Effect of Different Annealing Conditions on Hardness

As has been mentioned previously, most multilayer films will decrease in strength due to a layer structure breakdown, either by diffusion and alloying, spherodization, or triple joint formation, depending on the chemistry of the different constituents. In contrast, previous investigations on the present system indicated there is a significant increase in strength after annealing [60]. In the Cu/Ni/Nb investigation it was hypothesized that the Ni-Nb interface could be creating intermetallic precipitates along the boundary due to subtle diffusion from annealing, though no direct evidence was provided until the present study. The intermetallics would then provide an additional strengthening in the form of precipitation strengthening, enhanced multilayer strengthening (CLS mechanism) from further reduction of the individual layer thickness, as well as purely from the addition of a strong intermetallic which was not present before annealing. Since a more extensive annealing investigation was conducted during this study, the effect of both different temperatures and different annealing times on the room temperature hardness of the multilayers could be determined.

5.1 As-Deposited Strength of NMM films

In order to determine the starting strength of these films, nanoindentation was conducted on the as-deposited films using a Hysitron Triboindenter at the Erich Schmit Institute in Leoben, Austria. All films were indented using a load controlled trapezoid load function with a loading/unloading rate of 300 μN/s and hold time of 10s. A 5s drift check at about 10% of the maximum load was also added to the unloading segment. The maximum load applied (4000 μN for 5 nm layers and 3000 µN for 30 nm layers) was changed to get approximate contact depths of 100 nm. Table 5-1 summarizes the as-deposited mechanical properties of each of the films including one standard deviation from the mean, indicating the relative spread in the values resulting from different local roughness in the film or subtle changes in drift rate.

Table 5-1. As-deposited modulus and hardness of the different films used in this investigation.

Sample	As-deposited E_r (GPa)	As-deposited H (GPa)
5 nm Alloy	160.40 ± 9.8	6.06 ± 0.48
5 nm Tri-layer	144.99 ± 8.1	5.41 ± 0.37
30 nm Alloy	169.29 ± 18.3	4.64 ± 0.30
30 nm Tri-layer	158.71 ± 14.8	4.56 ± 0.18

As can be seen from the table, all of the modulus values are approximately the same value, with the alloy films only being slightly more than the tri-layer films. A similar modulus is expected for these films since they all have the same volume fraction of constituents; therefore, the slight difference in the modulus could be a result of slight substrate effects which would be more visible in the thinner alloy films. The most noticeable difference is the higher strength of the alloy films when compared to the tri-layers. The additional solid solution strengthening which is occurring in the CuNi alloy layer is adding to the overall hardness of the film, with hardness values increasing by 7% for the 30 nm layer thickness and 17% for the 5 nm layer thickness. This suggests that solid solution strengthening of two constituents is more effective at increasing the strength of the film than the addition of a coherent interface. Finally, as is theoretically expected from the CLS deformation model, the hardness of the 5 nm multilayers is higher than the 30 nm layers in both material systems.

5.2 Annealing Effect on Strength

All annealing conditions were indented using the same loading conditions and indenter tip as the as-deposited samples. Changes in hardness due to different annealing times and temperatures were examined and are summarized in Figure 5-1 and 5-2, respectively. As was seen in previous investigations the hardness of all the films increases as the annealing conditions also increase. Specifically focusing on annealing time dependence (Figure 5-1), it is apparent that even at a moderate annealing temperature (T_h(Cu) = 0.28) causes an increase in the hardness values for each of the films. Interestingly, annealing these films for 1 hour actually resulted in a significant drop in strength which was not expected and does not hold with the general trend. However, since the modulus of all of the films also drops by approximately 20 GPa, it is likely that this apparent softening in all of the films is due to experimental error rather than an actual physical softening in the film. This annealing condition will be retested at a future date. Increasing the annealing time to 3 hours causes substantial hardening in all of the films (although the 30 nm alloy film was never annealed at this condition), indicating the mechanism behind increase in hardness is actually occuring. This strongly hints at a time dependent strengthening mechanism, likely due to diffusion of the different elements. The films were then held at 300°C for 12 hours in an attempt to reach a saturation point which would lead to a plateau in the hardness values of the films. The 5 nm tri-layer film delaminated after annealing for this long and thus could not be indented to determine if a hardness plateau had been reached. The remaining films however showed an interesting trend. Both the 30 nm tri-layer film and the 5 nm alloy film actually showed a decrease in hardness when compared to the previous annealing condition. While this is not completely unexpected from the 5 nm alloy film where layer degradation can easily occur (though unproven at this point), the hardness drop in the 30 nm tri-layer film was both unexpected and not obviously explainable by the XRD and TEM investigations reported previously. While there is still an overall strengthening in the film when compared to the as-deposited condition, the drop in strength when increasing the annealing time beyond 3 hrs is difficult to explain without accompanying TEM images of the 3 hr annealing condition. The XRD scans of the 30 nm tri-layer film annealed at 300°C for 12 hours showed very little change from the as-deposited condition, with peak ratios remaining remarkably consistent regardless of the annealing condition. Since very small particles or very thin layers generally are not capable of being resolved by the XRD method, the lack of a change does not necessarily mean that thin layers of Nb_xNi_y do not exist. Since the hardness of the films obviously increases with increasing annealing time, the hardening mechanism points to a method that cannot be detected using XRD. However, the TEM images for the 30 nm tri-layer film annealed at 300°C 12 hr annealing condition (See Section 4.2.1 and 4.4.1) suggest that there actually is a microstructural change from annealing, presenting itself as a very thin (2-3 nm) Nb_xNi_y layer at both the Nb-Ni and Cu-Nb interface. Presumably, this thin layer would also be present in the 3 hr annealed samples since the hardness increased for these conditions as well.

Since the 30 nm alloy film annealed under this same condition was not able to be imaged due to an unfortunate catastrophe, a comparison of the amount of Nb_xNi_y which develops during the same annealing condition cannot be assessed. However, since the 30 nm alloy film shows a significant hardness increase from the as deposited condition, it is highly likely that a considerable Nb_xNi_y layer is the root cause. Once again, the XRD scans to do not suggest a very thick layer has formed but as was pointed out in Section 3.2.4 a slight shoulder on the left side of the Nb peak does indicate there is a detectible change greater than what is seen in the tri-layer films. Since the Ni is readily available at the Nb interface in the alloy sample, the initial diffusion of Ni through Cu does not slow down the intermetallic formation. Therefore, for the same amount of time a thicker Nb_xNi_y layer can form at the interface, causing a greater amount of hardening than in the tri-layer sample. Accompanying TEM/EDS evidence of this is still required and is currently in progress.

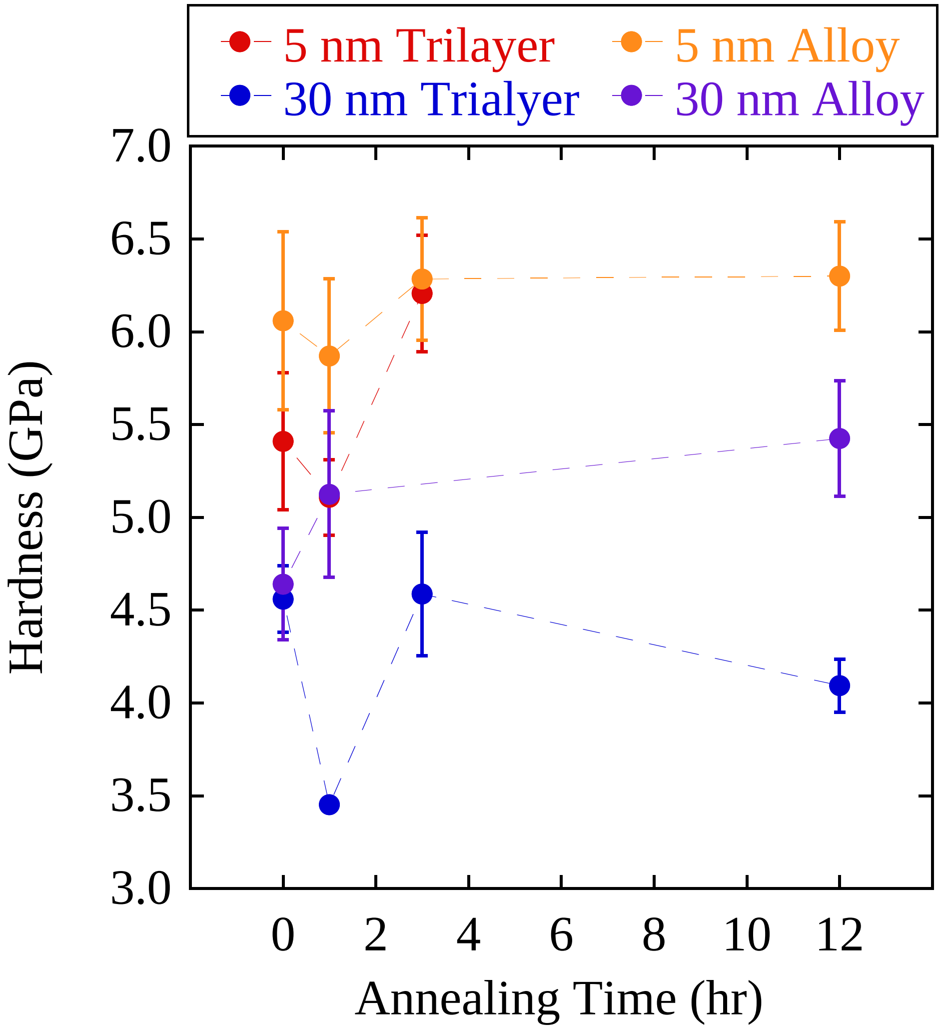

Figure 5-1. Nanoindentation hardness of both tri-layer and alloy films vacuum annealed at 300°C for 1, 3, and 12 hours and compared to as-deposited film condition. An increase in hardness is detected for all films, though the relative amounts are different depending on the type of film.

The films were also annealed to determine annealing temperature dependence on hardness at temperatures ranging from 200°C to 500°C (Figure 5-2). The film was annealed at 200°C for 1 hr while the 300°C 3 hr condition is reported since the 1 hr condition did not give reasonable data. The 500°C and 600°C conditions are from wafer curvature experiments which only had a few seconds at maximum temperature in an attempt to avoid delamination of the film. Since diffusion is more greatly affected by the annealing temperature, a general trend using these different annealing times is still acceptable. From the figure, it is apparent that annealing at 200°C for one hour does not affect the strength of the film, with the exception of the 30 nm tri-layer film which drops slightly. In general, as the annealing temperature increases, the hardness of the films also increase, with the peak occurring at 500°C followed by a substantial drop at 600°C (though still higher than the as-deposited condition). Comparing to the wafer curvature and XRD scans of these temperature conditions, it is apparent that a substantial change in the microstructure is occurring between 300°C and 550°C. The TEM scans of the 30 nm layer films both show a considerable layer forming at both Nb-X interfaces, consisting mostly of Nb and Ni (Nb_xNi_y intermetallic). The tri-layer film showed a diffusional gradient about 6 nm wide at this interface while the alloy film showed a thicker region measuring about 10 nm. Those results suggest that the tri-layer film is slightly more resistant to microstructural changes at similar annealing conditions because the Ni has to diffuse through the Cu layer to reach the Nb interface while the CuNi alloy already has enough Ni at both sides of the Nb to start intermetallic formation immediately. It is likely that at longer annealing times, the thickness of the Nb_xNi_y layer would be approximately the same thickness for the two different layers; however, that study has yet to be conducted. Interestingly, the hardness of all of the films drops at an annealing temperature of 600°C despite the obvious increase in intermetallics (either particle size or layer thickness) as was seen from the XRD measurements. This could be due to a complete breakdown of the multilayer structures (as is seen in other multilayer films), which would remove the strengthening benefit from this mechanism. However, further TEM investigations would be necessary to prove this hypothesis.

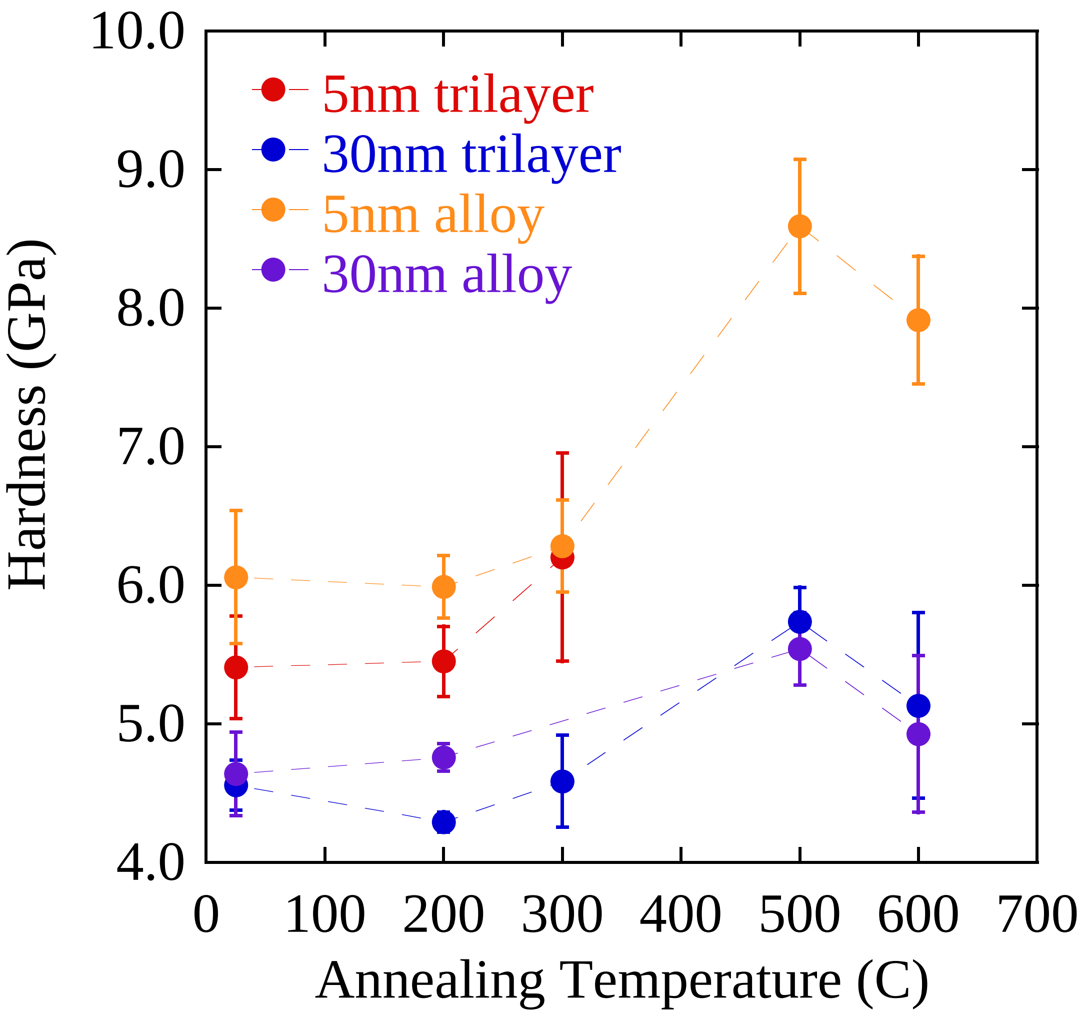

Figure 5-2. Nanoindentation hardness of tri-layer and alloy films annealed at different temperatures: as-deposited, 200°C 1hr, 300°C 3hr, 500°C wafer curvature and 600°C wafer curvature.

CHAPTER 6 : **Conclusions**

The multilayer systems investigated in the current study show a unique strengthening ability after annealing, which is uncommon for the majority of the multilayer systems currently being studied in literature. This ability stems from the fact that these multilayers have 3 components with the possibility of creating both solid solution CuNi as well as Ni_xNb_y intermetallics, which would inherently change the microstructure of the films by potentially removing the Cu/Ni interface through solid solution formation, or adding small intermetallic precipitates or an thin intermetallic layer which is not seen in as-deposited samples. Through XRD, and TEM characterization, the effect annealing at different temperatures and times has on a tri-layer Cu/Ni/Nb and alloy CuNi/Nb films was investigated.

Wafer curvature tests for the two different films were also conducted to determine the relative temperature at which a change in the microstructure is observed. Interestingly, for all of the films investigated, there are two different stress inflection/reduction points. The first occurs at around 150°C-200°C and correlates to the initial onset of plasticity and any number of stress drop processes: dislocation motion, grain boundary rotation, grain growth, or phase change. After this initial stress reduction the compressive stresses once again increase rapidly which indicates a strengthening mechanism is occurring as the temperature increases and is most likely due to the gradual Ni_xNb_y intermetallic formation. After 550°C, a second stress reduction is observed and is most likely the point at which significant changes in the microstructure is occurring, possibly due to layer degradation from spherodization or full alloying/intermetallic formation.

All annealing conditions were examined using x-ray diffraction to determine the relative change in elemental peak intensities and hopefully observe the formation of new peaks which would correspond to the specific alloy/intermetallic which is forming as a result of the different annealing conditions. After annealing at 300°C or higher both the tri-layer films and alloy films showed a change in the peak ratios (compared to the as-deposited condition). As either the annealing time or annealing temperature increased the relative strength of the Ni peak decreased indicating more Ni is being converted to Ni_xNb_y, or even CuNi alloy for the tri-layer samples. Since no obvious Ni_xNb_y peaks are observed even while the peak ratios change and the strength increases, it is most likely that the intermetallics which are formed are on the order of a few nanometers in length. Since traditional XRD technique is unable to resolve crystallites smaller than a few tens of nanometers, it is not surprising that no new peaks were observed.

Two different annealing conditions on two different samples were prepared for TEM characterization; however, only three samples could be characterized. Both 30 nm multilayer samples at 300°C 12 hr and 500°C wafer curvature annealing conditions were chosen for microstructural characterization since these two annealing conditions would be the most likely to show significant intermetallic formation. Through both STEM and EDS methods, a very thin layer of Ni_xNb_y was observed in all of the annealed samples on either side of the Nb layer. This layer was not observed in either of the as-deposited conditions, proving it is a direct result of annealing. Interestingly, even in the tri-layer sample, the Ni_xNb_y layer is observed on both sides of the Nb layer even at the Cu-Nb interface. This observation suggests Ni is diffusing through the Cu layer without first completely alloying the Cu and Ni layers. Since the 30 nm alloy annealed at 300°C for 12 hrs was not characterized, the comparative thickness of the Ni_xNb_y layer between the two different compositions at this annealing condition could not be determined. However, it is apparent in the 500°C annealing condition that the alloy film has a thicker Ni_xNb_y layer than the tri-layer film, indicating that the tri-layer film is more thermally stable than the alloy film, most likely because the Ni has to first diffuse through the Cu layer to interact with the Nb at the Cu-Nb interface.

Finally, nanoindentation experiments were conducted on all of the annealing conditions to determine if there is a peak strengthening point in either the annealing time or annealing temperature. For the 300°C annealing temperature, there seems to be a peak in the strengthening somewhere between 3 hr and 12 hrs. The decreased strength at 1 hr annealing time is unexpected and the reason behind the hardness drop is still unverified. Annealing the films at different temperatures showed an obvious peak in hardness at the 500°C annealing condition which corresponds well to the wafer curvature observations where the peak compressive stress was somewhere between 500°C and 600°C.

Overall, the annealing investigation of these tri-component multilayer systems showed an increase in strength as both annealing time and temperature increased, up to 500°C. This strengthening is due to Ni_xNb_y intermetallic formation at all incoherent interfaces: Cu-Nb, Ni-Nb, and CuNi-Nb. In general, it seems as though the tri-layer film microstructure is more stable than the alloy film with less intermetallic formation at a given temperature and therefore less relative strength increase as a result of annealing.

References

[1] Y. H. Chew, C. C. Wong, F. Wulff, F. C. Lim, and H. M. Goh, "Strain rate sensitivity and Hall–Petch behavior of ultrafine-grained gold wires," *Thin Solid Films*, vol. 516, no. 16, pp. 5376–5380, Jun. 2008.

[2] N. J. Petch, "Cleavage strength of Polycrystals," *J. Iron Steel Inst.*, pp. 25–28, 1953.

[3] C. C. Lo, "Hardening mechanisms of hard gold," *J. Appl. Phys.*, vol. 50, no. 11, p. 6887, Jul. 1979.

[4] E. O. Hall, "The Deformation and Ageing of Mild Steel: III Discussion of Results," *Proc. Phys. Soc. B*, vol. 747, 1951.

[5] A. F. Jankowski and H. S. T. Ahmed, "The nanoscratch hardness of a gold–nickel nanocrystalline nanolaminate at high strain rate," *Mater. Lett.*, vol. 77, pp. 103–106, Jun. 2012.

[6] M. Coll, C. A. Hacker, L. H. Miller, D. R. Hines, E. D. Williams, and C. A. Richter, "Ultrasmooth Gold as a Top Metal Electrode for Molecular Electronic Devices M.Coll," *ECS Trans.*, vol. 16, no. 25, pp. 139–146, 2009.

[7] S. K. Ghosh, P. K. Limaye, B. P. Swain, N. L. Soni, R. G. Agrawal, R. O. Dusane, and A. K. Grover, "Tribological behaviour and residual stress of electrodeposited Ni / Cu multilayer films on stainless steel substrate," *Surf. Coatings Technol.*, vol. 201, pp. 4609–4618, 2007.

[8] A. K. Ghosh and C. H. Hamilton, "Mechanical Behavior and Hardening Characteristics of a Superplastic Ti-6Al-4V Alloy," *Metall. Trans. A*, vol. 10, no. June, pp. 699–706, 1979.

[9] M. A. Muñoz-Morris, C. Garcia Oca, and D. G. Morris, "An analysis of strengthening mechanisms in a mechanically alloyed, oxide dispersion strengthened iron aluminide intermetallic," *Acta Mater.*, vol. 50, no. 11, pp. 2825–2836, Jun. 2002.

[10] P. C. Millett, R. P. Selvam, and A. Saxena, "Stabilizing nanocrystalline materials with dopants," *Acta Mater.*, vol. 55, no. 7, pp. 2329–2336, Apr. 2007.

[11] P. C. Millett, R. P. Selvam, and A. Saxena, "Molecular dynamics simulations of grain size stabilization in nanocrystalline materials by addition of dopants," *Acta Mater.*, vol. 54, no. 2, pp. 297–303, Jan. 2006.

[12] T. Bannuru, W. L. Brown, S. Narksitipan, and R. P. Vinci, "The electrical and mechanical properties of Au–V and Au–V2O5 thin films for wear-resistant RF MEMS switches," *J. Appl. Phys.*, vol. 103, no. 8, p. 083522, 2008.

[13] N. Fuschillo and M. L. Gimpl, "Electrical and Tensile Properties of Cu-ThO2, Au-ThO2, Pt-ThO2 and Au-Al2O3, Pt-Al2O3 Alloys," *J. Mater. Sci.*, vol. 5, pp. 1078–1086, 1970.

[14] L. A. Zepeda-Ruiz, G. H. Gilmer, B. Sadigh, A. Caro, T. Oppelstrup, and A. V. Hamza, "Atomistic simulations of grain boundary pinning in CuFe alloys," *Appl. Phys. Lett.*, vol. 87, no. 23, p. 231904, 2005.

[15] J. Weissmuller, W. Krauss, T. Haubold, R. Birringer, and H. Gleiter, “Atomic structure and thermal stability of nanostructured Y-Fe alloys,” *Nanostructured Mater.*, vol. 1, pp. 439–447, 1992.

[16] D. S. Gianola, B. G. Mendis, X. M. Cheng, and K. J. Hemker, “Grain-size stabilization by impurities and effect on stress-coupled grain growth in nanocrystalline Al thin films,” *Mater. Sci. Eng. A*, vol. 483–484, pp. 637–640, Jun. 2008.

[17] A. Misra, M. Verdier, Y. C. Lu, H. Kung, T. E. Mitchell, M. Nastasi, and J. D. Embury, “Structure and mehcanical properties of Cu-X (X ⸝ Nb , Cr , Ni) nanolayered composites,” *Scr. Mater.*, vol. 39, pp. 555–560, 1998.

[18] H. C. Barshilia and K. . Rajam, “Characterization of Cu/Ni multilayer coatings by nanoindentation and atomic force microscopy,” *Surf. Coatings Technol.*, vol. 155, no. 2–3, pp. 195–202, Jun. 2002.

[19] A. Misra, J. P. Hirth, and R. G. Hoagland, “Length-scale-dependent deformation mechanisms in incoherent metallic multilayered composites,” *Acta Mater.*, vol. 53, no. 18, pp. 4817–4824, Oct. 2005.

[20] J. Wang and A. Misra, “An overview of interface-dominated deformation mechanisms in metallic multilayers,” *Curr. Opin. Solid State Mater. Sci.*, vol. 15, no. 1, pp. 20–28, Feb. 2011.

[21] J. Y. Zhang, X. Zhang, G. Liu, G. J. Zhang, and J. Sun, “Scaling of the ductility with yield strength in nanostructured Cu/Cr multilayer films,” *Scr. Mater.*, vol. 63, no. 1, pp. 101–104, Jul. 2010.

[22] N. Abdolrahim, “Multiscale modeling and simulation of deformation and strength of nanoscale metallic multilayer systems,” 2012.

[23] H. M. Zbib, C. T. Overman, F. Akasheh, and D. Bahr, “Analysis of plastic deformation in nanoscale metallic multilayers with coherent and incoherent interfaces,” *Int. J. Plast.*, vol. 27, no. 10, pp. 1618–1639, Oct. 2011.

[24] A. Bellou, C. T. Overman, H. M. Zbib, D. F. Bahr, and A. Misra, “Strength and strain hardening behavior of Cu-based bilayers and trilayers,” *Scr. Mater.*, vol. 64, no. 7, pp. 641–644, Apr. 2011.

[25] I. N. Mastorakos, H. M. Zbib, and D. F. Bahr, “Deformation mechanisms and strength in nanoscale multilayer metallic composites with coherent and incoherent interfaces,” *Appl. Phys. Lett.*, vol. 94, no. 17, p. 173114, 2009.

[26] S. Shao, H. M. Zbib, I. N. Mastorakos, and D. F. Bahr, “Deformation mechanisms, size effects, and strain hardening in nanoscale metallic multilayers under nanoindentation,” *J. Appl. Phys.*, vol. 112, no. 4, p. 044307, Aug. 2012.

[27] J. L. Bucaille, S. Stauss, E. Felder, and J. Michler, “Determination of plastic properties of metals by instrumented indentation using different sharp indenters,” *Acta Mater.*, vol. 51, no. 6, pp. 1663–1678, Apr. 2003.

[28] I. N. Mastorakos, A. Bellou, D. F. Bahr, and H. M. Zbib, “Size-dependent strength in nanolaminate metallic systems,” *J. Mater. Res.*, vol. 26, no. 10, pp. 1179–1187, May 2011.

[29] P. Troche, J. Hoffmann, K. Heinemann, F. Hartung, G. Schmitz, H. C. Freyhardt, D. Rudolph, J. Thieme, and P. Guttmann, "Thermally driven shape instabilities of Nb/Cu multilayer structures: instability of Nb/Cu multilayers," *Thin Solid Films*, vol. 353, no. 1–2, pp. 33–39, Sep. 1999.

[30] N. Mara, A. Sergueeva, A. Misra, and A. K. Mukherjee, "Structure and high-temperature mechanical behavior relationship in nano-scaled multilayered materials," *Scr. Mater.*, vol. 50, no. 6, pp. 803–806, Mar. 2004.

[31] A. Misra, R. G. Hoagland, and H. Kung, "Thermal stability of self-supported nanolayered Cu/Nb films," *Philos. Mag.*, vol. 84, no. 10, pp. 1021–1028, Apr. 2004.

[32] S. A. Barnett, A. Madan, I. Kim, and K. Martin, "Stability of nanometer-thick layers in hard coatings," *MRS Bull.*, no. March, pp. 169–172, 2003.

[33] J. C. Malzahn Kampe, T. H. Courtney, and Y. Leng, "Shape instabilities of plate-like structures- I. Experimental observations in heavily cold worked in situ composites," *Acta Metall.*, vol. 37, no. 7, pp. 1735–1745, 1989.

[34] D. R. Economy, B. M. Schultz, and M. S. Kennedy, "Impacts of accelerated aging on the mechanical properties of Cu–Nb nanolaminates," *J. Mater. Sci.*, vol. 47, no. 19, pp. 6986–6991, Jul. 2012.

[35] D. Josell, T. P. Weihs, and H. Gao, "Diffusional creep : stresses and strain rates in thin films and multilayers," *MRS Bull.*, no. January, pp. 39–44, 2002.

[36] H. R. Gong and B. X. Liu, "Unusual alloying behavior at the equilibrium immiscible Cu–Nb interfaces," *J. Appl. Phys.*, vol. 96, no. 5, p. 3020, 2004.

[37] H.-J. Lee, K.-W. Kwon, C. Ryu, and R. Sinclair, "Thermal stability of a Cu/Ta multilayer: an intriguing interfacial reaction," *Acta Mater.*, vol. 47, no. 15–16, pp. 3965–3975, Nov. 1999.

[38] N. A. Mara, A. Misra, R. G. Hoagland, A. V. Sergueeva, T. Tamayo, P. Dickerson, and A. K. Mukherjee, "High-temperature mechanical behavior/microstructure correlation of Cu/Nb nanoscale multilayers," *Mater. Sci. Eng. A*, vol. 493, no. 1–2, pp. 274–282, Oct. 2008.

[39] N. A. Mara, T. Tamayo, A. V. Sergueeva, X. Zhang, A. Misra, and A. K. Mukherjee, "The effects of decreasing layer thickness on the high temperature mechanical behavior of Cu/Nb nanoscale multilayers," *Thin Solid Films*, vol. 515, no. 6, pp. 3241–3245, Feb. 2007.

[40] A. Misra and R. G. Hoagland, "Effects of Elevated Temperature Annealing on the Structure and Hardness of Copper/niobium Nanolayered Films," *J. Mater. Res.*, vol. 20, no. 08, pp. 2046–2054, Mar. 2005.

[41] A. A. Volinsky, N. R. Moody, and W. W. Gerberich, "Nanoindentation of Au and Pt/Cu thin films at elevated temperatures," *J. Mater. Res.*, vol. 19, no. 09, pp. 2650–2657, Mar. 2011.

[42] A. C. Lewis, D. Josell, and T. P. Weihs, "Stability in thin film multilayers and microlaminates: the role of free energy, structure, and orientation at interfaces and grain boundaries," *Scr. Mater.*, vol. 48, no. 8, pp. 1079–1085, Apr. 2003.

[43] J.-M. Roussel and P. Bellon, “Interface sharpening and broadening during annealing of Cu/Ni multilayers: A kinetic Monte Carlo study,” *Phys. Rev. B*, vol. 73, no. 8, p. 085403, Feb. 2006.

[44] H. J. Bunshah, R. F., Nimmagadda, R., Doerr, “Structure and property relationships in microlaminate Ni-Cu and Fe-Cu condensates,” *Thin Solid Films*, vol. 72, pp. 261–275, 1980.

[45] D. B. Butrymowicz, J. R. Manning, and M. E. Read, “Diffusion of Copper and Copper Alloys: Part IV. Diffusion in Systems Involving Elements of Group VIII,” *J. Phys. Chem. Ref.*, vol. 5, no. 1, pp. 103–200, 1976.

[46] NIST, “Cu-Ni Phase Diagram,” 2008. [Online]. Available: http://www.nims.go.jp/cmsc/pst/database/cu-elem/cuni/cuni.htm. [Accessed: 09-Mar-2015].

[47] J. S. Carpenter, S. J. Zheng, R. F. Zhang, S. C. Vogel, I. J. Beyerlein, and N. A. Mara, “Thermal stability of Cu–Nb nanolamellar composites fabricated via accumulative roll bonding,” *Philos. Mag.*, vol. 93, no. 7, pp. 718–735, Mar. 2013.

[48] Alphysica, “Cu-Nb, Cu/Cu-Nb and CuFe conductors,” 2015. [Online]. Available: http://www.alphysica.com/index.php/cu-nb.html. [Accessed: 09-Mar-2015].

[49] O. S. University, “No Title,” 2005. [Online]. Available: ME481/581: Final Exam F05 . [Accessed: 09-Mar-2015].

[50] P. A. Flinn, “Principles and applications of wafer curvature techniques for stress measurements in thin films,” *Mat Res Soc Symp Proc*, vol. 130, pp. 41–51, 1989.

[51] H. Ru, J. Li, and W. Wang, “3D Network SiC-Metals Composites for Heavy Duty Brake Applications,” 2010. [Online]. Available: http://www.intechopen.com/books/metal-ceramic-and-polymeric-composites-for-various-uses/3d-network-sic-metals-composites-for-heavy-duty-brake-applications#article-front. [Accessed: 01-Dec-2014].

[52] W. C. Oliver and G. M. Pharr, “An improved technique for determining hardness and elastic modulus using load and displacement sensing indentation experiments,” *J. Mater. Res.*, vol. 7, no. 6, pp. 1564–1583, 1992.

[53] D. F. Bahr and W. W. Gerberich, “Plastic Zone and Pileup around Large Indentations,” *Metall. Mater. Trans. A*, vol. 27A, no. December, pp. 3793–3800, 1996.

[54] D. Tabor, *The Hardness of Metals*. Oxford University Press, 1951.

[55] K. L. Johnson, “The correlation of indentation experiments,” *J. Mech. Phys. Solids*, vol. 18, no. 2, pp. 115–126, Apr. 1970.

[56] A. F. Bower, N. A. Fleck, A. Needleman, and N. Ogbonna, “Indentation of a power law creeping solid,” *Proc. R. Soc. Lond. A.*, vol. 441, no. 1911, pp. 97–124, 1993.

[57] J. C. Trenkle, C. E. Packard, and C. a Schuh, “Hot nanoindentation in inert environments.,” *Rev. Sci. Instrum.*, vol. 81, no. 7, p. 073901, Jul. 2010.

[58] B. D. Beake and J. F. Smith, “High-temperature nanoindentation testing of fused silica and other materials,” *Philos. Mag. A*, vol. 82, no. 10, pp. 2179–2186, Jul. 2002.

[59] C. A. Schuh, C. E. Packard, and A. C. Lund, “Nanoindentation and contact-mode imaging at high temperatures,” pp. 725–736, 2006.

[60] R. L. Schoeppner, N. Abdolrahim, I. Salehinia, H. M. Zbib, and D. F. Bahr, “Elevated temperature dependence of hardness in tri-metallic nano-scale metallic multilayer systems,” *Thin Solid Films*, pp. 31–36, May 2014.

[61] S. Enzo, G. Fagherazzi, A. Benedetti, and S. Polizzi, “A profile-fitting procedure for analysis of broadened X-ray diffraction peaks. I. Methodology,” *J. Appl. Crystallogr.*, vol. 21, no. 5, pp. 536–542, Oct. 1988.

[62] C. A. Volkert, C. F. Alofs, and J. R. Liefting, “Deformation mechanisms of Al films on oxidized Si wafers,” *J. Mater. Res.*, vol. 9, no. 5, pp. 1147–1155, 1994.

[63] T. P. L. Pedersen, J. Kalb, W. K. Njoroge, D. Wamwangi, M. Wuttig, and F. Spaepen, “Mechanical stresses upon crystallization in phase change materials,” *Appl. Phys. Lett.*, vol. 79, no. 22, pp. 198–201, 2001.

[64] I. R. Aseguinolaza, I. Orue, a. V. Svalov, K. Wilson, P. Müllner, J. M. Barandiarán, and V. a. Chernenko, “Martensitic transformation in Ni–Mn–Ga/Si(100) thin films,” *Thin Solid Films*, vol. 558, pp. 449–454, May 2014.

[65] M. F. Ashby, “A first report on deformation-mechanism maps,” *Acta Metall.*, vol. 20, pp. 887–897, 1972.

[66] T. G. Langdon and F. A. Mohamed, “A New Type of Deformation Mechanism Map for High-temperature Creep,” *Mater. Sci. Eng. A*, vol. 32, pp. 103–112, 1978.

[67] L. Heinz, R. A. White, and O. D. Sherby, “Grain Boundary Sliding and Deformation Mechanism Maps,” *Mater. Sci. Eng. A*, vol. 39, pp. 211–216, 1979.

[68] D. Weiss, H. Gao, and E. Arzt, “Constrained diffusional creep in uhv-produced copper thin films,” *Acta Mater.*, vol. 49, pp. 2395–2403, 2001.

[69] R. P. Vinci, E. M. Zielinski, and J. C. Bravman, “Thermal strain and stress in copper thin films,” *thin s*, vol. 262, pp. 142–153, 1995.

[70] C. V Thompson, “Grain Growth in Thin Films,” *Annu. Rev. Mater. Sci.*, vol. 20, no. 1, pp. 245–268, Aug. 1990.

[71] N. Abdolrahim, H. M. Zbib, and D. F. Bahr, “Multiscale modeling and simulation of deformation in nanoscale metallic multilayer systems,” *Int. J. Plast.*, vol. 52, pp. 33–50, Jan. 2014.